Experimental study and computational simulation of fibre suspension flows - Application to headboxes

Leandro Sebastian Salgueiro Hartard

INSTITUT POLYTECHNIQUE DE GRENOBLE

N° attribué par la bibliothèque

|_|_|_|_|_|_|_|_|_|_|

THÈSE

pour obtenir le grade de **DOCTEUR DE Grenoble INP**

Spécialité : « Génie des procédés »

préparée au laboratoire LGP2 dans le cadre de **l'École Doctorale « Matériaux et Génie des Procédés »**

présentée et soutenue publiquement par

Leandro Sebastian SALGUEIRO HARTARD

le 20 juin 2008

Etude expérimentale et simulation d'écoulements de suspensions fibreuses Application à une caisse de tête

---

Directeur de thèse : M. Jean-Claude ROUX
Co-directrice : Mme Martine RUEFF

JURY

Mme Evelyne MAURET	Présidente
Mme Maria-Angels PELACH SERRA	Rapporteure
M. Samuel SCHABEL	Rapporteur
M. Simon CENA	Examinateur
M. Jean-Claude ROUX	Directeur de thèse
Mme Martine RUEFF	Co-encadrante

Contents

Remerciements

Je tiens à remercier en tout premier lieu Martine Rueff qui a co-encadré cette thèse dans la continuité de mon stage de DEA. Tout au long de ces quatre années, elle a su orienter mes recherches aux bons moments en me donnant de courage quand les solutions n'étaient pas évidentes, elle a toujours été disponible pour d'intenses et rationnelles discussions. Pour tout cela, sa confiance et son soutien en fin de thèse, je la remercie vivement. Je tiens à remercier aussi mon directeur de thèse, le Professeur Jean-Claude ROUX, pour tout son soutien pendant mon séjour à l'EFPG, sa bienveillance et ses conseils.

Je remercie les rapporteurs de cette thèse, madame Maria-Angels PELACH SERRA, professeure à l'université de Girona, et monsieur Samuel SCHABEL, professeur à l'université technologique de Darmstadt, pour la rapidité avec laquelle ils ont lu mon manuscrit et l'intérêt qu'ils ont porté à mon travail. Merci également à la présidente du jury, madame Evelyne MAURET, professeure à Grenoble-INP, qui a accepté de juger ce travail, : les discussions partagées avec elle m'ont permis de avoir confiance dans le futur et m'ont permis d'évoluer professionnellement.

Je voudrais vivement remercier l'EFPG qui m'a ouvert ses portes depuis le premier jour avec une amitié inconditionnelle que m'a fait me sentir comme chez moi. Au risque de manquer quelqu'un, je voudrais ne pas citer de noms. Tous ont participé à mon succès et ils savent qu'ils resteront dans mon cœur. Cependant il y a des gens que je voudrais quand même citer, en premier lieu merci Mohamed Aichi pour tout ton aide et ton amitié, Chu, Charlotte, Nathalie, Denis, Philippe, Jean-Marc, bref tout le service technique auxquels je dois tant. Bien sur, je ne voudrais pas oublier Olivier, Guy, Gilles, Denis, Stéphane, avec eux je pu m'amuser autant à la machine à papier. Mes collègues de bureau et mes amis, Marie, Chiquito (Pierre) et Mohamed Krouit, Erginos, Babacar, Rémi, Davide qui m'ont supporté dans mes moments de stress et de désespoir.

Je tiens à remercier aussi Mathieu qui m'a traité toujours comme un frère.

Je devrais prendre l'annuaire de l'EFPG et le coller ici car ils sont tous devenues pas seulement les collègues et professeurs, mais aussi mes amis.

Je voudrais remercier spécialement mes parents (sans eux rien ne serait possible) et mon amie Amandine qui, pendant ces trois dernières années de folie, m'a supporté sans me jeter dehors ..., et aussi Ruben, mon frère gémeau, (comme il dit !).

Finalement, je tiens à remercier ma " famille " en France, Analin, Marco, Jane, Marc. Je ne vous oublierai jamais ...

Dedicated :
to my parents...
to Marc and Jane...
hope you were here...

Introduction

The evolution of paper machines to get better paper grades at faster production rates imposed paper mills to operate more complex systems and requested higher precision. Headboxes are the part of the paper mill that delivers diluted fibrous suspensions onto the forming wire. These headboxes as a central and fundamental part of the paper mill have not escaped from this continuous evolution. On the contrary, fundamental research was made, over the last fifty years, to try to understand fibrous suspension rheology and to give a scientific answer for a better stock distribution. However, even though some major advances were made in this subject some "dark areas" are still left in the design of modern headboxes:

- Some of these areas are due to a complete lack of understanding of the fibrous suspensions due to their complexity and the absence of measuring tools.
- Some of them come from a misbelief of old papermakers that kept some traditions in machine design.
- Some of them come from confidential clauses that kept the state-of-the art of headboxes evolution submerged in an ocean of secrets and lack of applicable data.

Even though a detailed description of fibrous suspension behaviour is searched nowadays, the major rheological parameters are still unknown. Paper forming should be as homogeneous as possible to ensure a good quality paper. However, owing to the nature and shape of fibres, flocculation is almost impossible to avoid. In this work, which was conducted thanks to the financial support of the French ministry of Education and Research and of the University, we will try to answer three major questions to try to keep re-flocculation level as low as possible:

1. Is it necessary to get a full rheological model of pulp suspensions for designing modern headboxes or are basic models sufficiently precise to describe the flow?

2. Are all the major parts of a headbox necessary? If yes, are they optimised?

3. Is it possible to predict the geometry of the free jet delivered by the headbox nozzle with simple tools?

The first chapter of this work introduces the historical background of the paper machine evolution, especially the headbox, and the complexity of fibrous suspension rheology. It is not the author's intention to fully describe these subjects but to give an idea of the complexity of papermaking and the reason why, until now, there is a lack of knowledge in these areas.

The second chapter is focused on the internal elements of a headbox. Its objective was to analyse the internal flows and determine whether dimensioning rules can be proposed or not. Therefore, an experimental study of fibrous suspension flows was carried out and numerical simulations, with water only, were performed thanks to CFD. For the experimental study, classical headloss measurements were made and more sophisticated methods, i.e. high speed imagery and non-invasive velocimetry thanks to a pulsed ultrasonic Doppler velocimeter, were used. Pulp behaviour was also compared to that of water. Indeed, no rheological model is available to describe the behaviour of pulp suspensions in the range of interest, which may be a problem for CFD. However, for most of the industrial conditions analysed, dimensioning with water is more restrictive than using a fibrous suspension. This is why the numerical simulations were run with water only in order to analyse turbulence intensity and length in the system.

The control of the jet is an important parameter in papermaking. Indeed, a good knowledge of the jet angle as well as its velocity is searched to have a total control of fibre orientation. Therefore, the third chapter of this dissertation is devoted to the prediction of the jet geometry. Several mathematical models, already published in the literature and applicable to ideal flows, were analysed. Not only were the jet angle and contraction ratio searched but also the location of the vena contracta. Experimental work was performed in order to check the applicability of these models. After observing that there was no significant difference in the jet shape between a fibrous suspension and water, CFD was applied with a two-phase model to predict the jet shape. This chapter ends with a comparison of all these methods and their limitations.

Finally, a general conclusion is made and some future perspectives are proposed.

Chapter 1

General concepts and evolution

This first chapter is mainly devoted to a review of the state-of-the art in hydrodynamics and rheology of fibrous suspensions. Indeed, understanding the behaviour of fibrous suspensions is a fundamental key for the development and optimisation of new equipments. However, it should be noticed that the development of new equipments was not only based on a scientific approach. It often depended on a heritage of older conceptions. Some old believes from papermakers interfered on the application of new technologies. This is why a historical background of paper manufacturing was made as an introduction, since it is important to understand the evolution of papermaking to get a global view of the optimisation possibilities of some machines. Finally, as this work was focused on the application to headboxes, a precise description of this apparatus closes this chapter.

1.1 Paper manufacturing historical background

For the common of people, a paper sheet is a trivial product with no technology inside. Modern papermaking is, nevertheless, a quite complicate procedure involving several high technology controls and machinery. Generally speaking, paper is made by drainage of a weak suspension of cellulose fibres. The wet web is formed and then pressed and dried to get a coherent structure, called "paper". This procedure was originally invented in China in the year 105 AD, by Cai Lun at the Han's dynasty using hemp fibres, fishing net residuals and bamboo fibres. Although paper was used originally as a protecting material (wrapping), it is commonly thought that it was widely used for writing purposes around the 3rd century. The first printed book found is the "Chinese Diamond Sutra" (see figure 1.1). It was found in 1907 by the archaeologist Sir Marc Aurel Stein in Mogao Caves in Dunhuang, and is now in the British Museum. This book is the proof of the common use of paper in Chinese society.

After further commercial trading and the defeat of the Chinese in the Battle of Talas in 751, the invention spread to the Middle East. Production was started in Baghdad,

Figure 1.1: Earliest known printed book, AD 868 (The British library www.bl.uk)

where the Arabs invented a method to make a thicker sheet of paper. The manufacture had spread to Damascus by the time of the First Crusade in the 11th century, but the wars interrupted production, and it split into two centres. Cairo continued with the thicker paper. Iran became the centre of the thinner papers. It was also adopted in India. The first paper mill in Europe was in Spain, at Xátiva (modern Valencia) in 1120. More mills appeared in Fabriano Italy in about the 13th century, as an import from Islamic Spain. They used hemp and linen rags as a source of fibre [1].

The development of new printing techniques made paper demand continuously increasing, which could not be followed by hand-made papermaking. This problem gave, in 1798, an idea to a young French engineer, Louis-Nicolas Robert who invented the first continuous paper machine as it is shown in figure 1.2.

Nevertheless, as it is known, the first prototype frequently does not work properly. This prototype was then optimised by M. Leger Didot and Mr. Bryan Donkin (see figure 1.3), and later on by Mr. John Gamble. In 1804, Messrs. Henry and Sealy Fourdrinier purchased the patent and acquired the first working continuous paper machine. Since then, the papermaking industry keeps on growing. Here, we must point out that today every flat forming unit continues to be known or called as "Foudrinier". The papermaking process is the same as in early years but, in order to respond to higher quality demand and higher production volumes, paper mills were changed, gaining in complexity and accuracy. An example of a 1920^{th} Foudrinier machine producing a 2 metre wide paper sheet at a rate of 400 metres per minute can be found in figure 1.4. Today, a modern paper machine can produce a ten metre wide paper sheet at a rate of 2000 metres per minute with similar operating units.

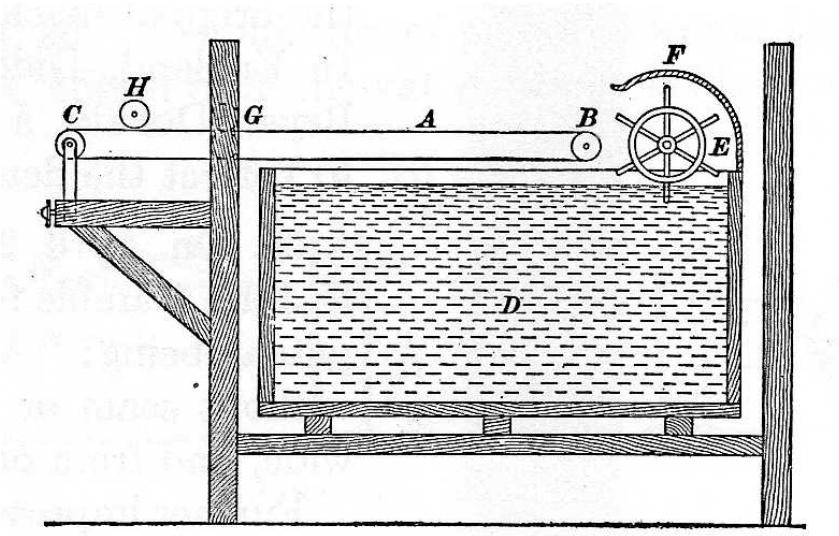

Figure 1.2: Louis-Nicolas Robert's paper machine

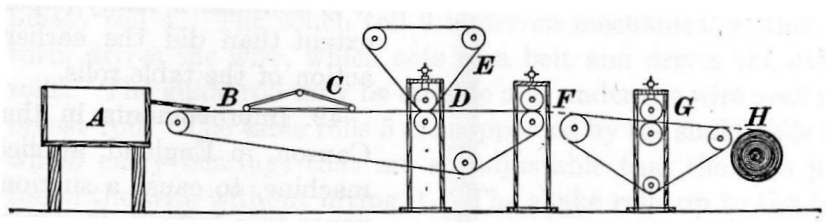

Figure 1.3: Donkin's paper machine

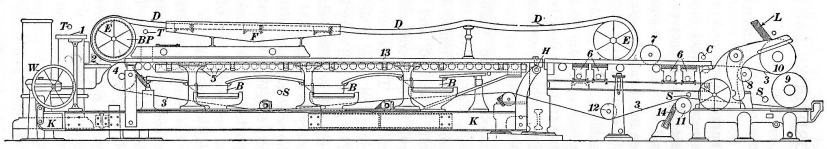

Figure 1.4: 1920^{th} Foudrinier paper machine

For a better comprehension of the complexity of papermaking, an explanation of cellulosic fibre morphology and a short review of fibre suspension rheology should be made.

1.2 Fibre description

The complexity of papermaking flows is closely linked to the cellulose fibre morphology and the procedure used for its extraction from wood. Fibres can be considered as flexible hollow tubes with tapered ends [2]. The main components of a fibre wall vary according to the tree species but in general these walls are composed by cellulose, hemicellulose and lignin. This last component acts as a matrix of a composite material bonding fibres together. The fibre dimensions vary with the growth rate of trees. This growth is not constant over a year. The fibres formed during the beginning of a growing season (earlywood) are thin-walled and their hollow centre is wide. On the other hand, fibres at the end of growing season (latewood) are thinner in diameter and longer than the previous ones but their walls are thicker. There is also a big variation of fibre morphology among tree species. Generally speaking the cellulose fibres can be divided into two big categories, the so-called "long" fibres which come essentially from softwood trees and the so-called "short" fibres which come from hardwood trees. The main difference between these two categories is the fibre length and wall thickness, and therefore fibre stiffness. In table 1.1 we can find the mean minimum and maximum morphology values of hardwood and softwood fibres.

Type	Length (mm)		Width(μm)		Wall thickness (μm)	
Hardwood	Min	Max	Min	Max	Min	Max
	0.8	1.6	16	38	2	3.75
Softwood	2.4	4.0	32	48	1.6	4.0

Table 1.1: Hardwood and Softwood mean morphological values (from [3, 4])

The extracting procedure used to get the cellulose fibres can also affect their physical characteristics. Generally speaking, the extracting procedures of fibres can be divided in four main families, the chemical treatments, the mechanical treatments, a mix between them, i.e. chemi-mechanical treatments, and recycled materials.

- The Kraft process is the best known and the main chemical process used nowadays. This process is suitable when strong, long flexible fibres are needed. The main purpose of the Kraft process is to render lignin soluble so it can be washed out from cellulose and hemicellulose cells. However, difficult bleaching and low yields are some limitations of this process.

- The mechanical procedure does not remove lignin, therefore yields are very high. It produces rigid, brittle fibres. However, the mechanical energy demand is very high, which limits this process application. The mechanical pulps can be divided into mechanical pulp and thermo-mechanical pulp (TMP). Their main difference is the use of steam-heated refiners to reduce the mechanical energy consumption by softening the wood components.

- Recycled materials are in general considered as a fourth type of raw material because of their heterogeneity. These are very complex materials mainly because of the presence of a certain amount of non-fibre elements mixed to fibres (i.e. sand, stickies, metals, organics, etc.). Even though high cleaning operations are used, there is still a high concentration of undesirable particles in the pulp.

All these processes will give the fibres some mechanical and electrochemical properties that will affect the pulp flow and therefore the paper quality. Flocculation, for instance, is a function of the pulp consistency, the aspect ratio of the fibres, i.e. the length to diameter ratio, and their stiffness. This phenomenon, among others, will be thoroughly discussed at the next section.

The main aim of this section is to draft a brief panorama of the complexity and the wide fan of variables present in a modern paper making mill. For further details of the different fibre extraction methods the reader should refer for instance to [2].

1.3 Review of fibre suspension behaviour

1.3.1 Flocculation of fibres

The most remarkable property of fibre suspensions is the formation of local mass aggregates called "flocs". This flocculation process was studied over the years in order to give a more homogeneous distribution of fibres and therefore a better quality paper. Flocculation depends on various factors such as: fibre concentration, fibre aspect ratio and flexibility. Concentration varies in a quite large range inside a mill. Typical values are:

- Pulp storing at 5-15% (50-150 g/L)
- Refining at 3% (30 g/L)
- Forming of paper at 0.5-1% (5-10 g/L)
- And laboratory handsheet forming at about 0.02% (0.20 g/L)

In fibrous suspensions, the mean value of the aspect ratio of fibres has a strong influence and flocculation occurs even at very low concentration ranges. The behaviour of an isotropic particle suspension, as the one studied by Einstein [5] [6], that changes for a particle concentration of 2% or higher, while a fibrous suspension changes for a much diluted particle concentration (i.e. approx. 0.1%). This difference of behaviour comes principally from the propensity of fibres to flocculate. Flocculation occurs as a resultant of forces applied to fibres and the space where these fibres evolutes.

Early works made by Mason [7] developed the idea that, in simple shear flow, there is a critical concentration where fibres can not keep moving freely without colliding to each others. Mason [7] developed a probabilistic distribution of the possible movement and orientation made by rigid elliptic particles. He simplified the model saying that the rotational movement of each particle develops a spherical volume with a diameter equal to the length of each particle. Then, he applied to these spherical volumes the Einstein's equation for obtaining the number of collisions between particles and to evaluate the critical concentration giving a flocculated pulp. According to Einstein, the duration of the rotation cycle of spheres in a shear flow is:

$$T = \frac{4\pi}{\left(\frac{dU}{dy}\right)} \tag{1.1}$$

where dU/dy is the shear rate. The number of collisions between the particles per time unit is:

$$n_{ct} = \frac{4}{3} a^3 n \frac{dU}{dy} \tag{1.2}$$

where n is the number of spheres per volume unit and a is the sphere diameter. The number of spheres per volume unit depends on the sphere diameter and their volumetric consistency C_{S0} as follows:

$$n = \frac{6C_{S0}}{\pi a^3} \tag{1.3}$$

The lifetime of a doublet, which is the time of contact of two spheres, may be expressed as a function of the shear rate:

$$t_v = \frac{\pi}{dU/dy} \tag{1.4}$$

In steady conditions the number of doublets per volume unit, n', is then:

$$n' = n_{ct} \frac{n}{2} t_v = 8C_{s0}^2 \frac{3}{\pi a^3} \tag{1.5}$$

Thus, the number of doublets per volume unit can be expressed as:

$$C_{doublets} = 8C_{s0}^2 \tag{1.6}$$

This equation works only for small spherical particles. Long flexible particles change the kinetic conditions because the lifetime of a doublet can last for an infinite period of time in a simple shear flow owing to the entanglement of the particles. The critical concentration, as developed by Mason [7], is achieved when the number of doublets per unit volume equals unity, i.e. when the volumetric concentration of spheres generated by fibres (length l and diameter d) is equal to $1/\sqrt{8}$. The concentration of fibres is then:

$$C = n\frac{4}{3}\pi\left(\frac{l}{d}\right)^3 = \frac{2}{3}C_0\left(\frac{l}{d}\right)^2 \tag{1.7}$$

So when C equals $1/\sqrt{8}$, C_0 is equal to the critical concentration:

$$C_{0critic} = \frac{3}{4\sqrt{2}}\left(\frac{d}{l}\right)^2 \tag{1.8}$$

Mason [7] defined a dilute regime which corresponds to concentrations of fibres inferior to this critical concentration, which means that the concentration of doublets is inferior to unity.

Wahren and Meyer [8], using statistical analysis, were the first authors to establish a relationship between the concentration and the number of contacts between fibres as a parameter to study flocculation:

$$C_0 = \frac{16\pi}{\left[\frac{2}{n_c}\frac{l}{d} + \frac{n_c}{n_c - 1}\right]^3 (n_c - 1)} \cdot \frac{l}{d} \tag{1.9}$$

where n_c is the number of contacts. Wahren and Meyer [8] fixed to three the number of contacts needed to get a fibrous suspension fully constrained in rotation and translation.

Other numerical predictions of the number of contacts per fibre were made by Dodson [9] who used statistical geometry, assumed that fibres are randomly arranged in space and developed the next equation:

$$n_c = 2C_v\frac{l}{d} \tag{1.10}$$

Pan [10] derived the following equation, also using a statistical geometry analysis:

$$n_c = 4\frac{l}{d}\frac{C_v}{(2+\pi C_v)} \tag{1.11}$$

It should be noticed that this equation gives similar results to those predicted by the previous one at high volumetric consistencies.

The number of contacts were measured by Soszynsky [11] on networks of nylon fibres suspended in sucrose solutions. However the number of contacts measured is less than the predicted one, sometimes almost by half. This could be related to the flexibility of nylon fibres.

Kerekes [12] has generalised Mason's idea to describe the fibrous suspension behaviour. He defined a "Crowding Number" which is a dimensionless number that describes the number of fibres in a volume swept out by the length of a fibre. This crowding number can be calculated by:

$$N = \frac{2}{3}C_v\left(\frac{l}{d}\right)^2 \tag{1.12}$$

or more conveniently for papermakers, it can be approximated using the mass consistency C in percentage, the fibre length l expressed in metres and the fibre coarseness ω expressed in kilograms per metre:

$$N \cong \frac{5Cl^2}{\omega} \tag{1.13}$$

It can be seen in equation 1.12 that for N equal to unity, we have the special case of Mason's critical concentration. Kerekes and Schell [13] simplified equation 1.9 to get the crowding number as a function of the number of contacts per fibre n_c:

$$N = \frac{4\pi n_c^3}{3\,(n_c - 1)} \tag{1.14}$$

The authors also assigned some empirical values of N to determine the typical regimes of fibrous suspensions, which are summarised in table 1.2

Regime	Type of fibre contact	Value of N
Dilute	Chance of collision	N<1
Semi-concentrate	Forced collision	1<N<60
Concentrated	Continuous contact	N>60

Table 1.2: Fibrous suspensions regimes by Kerekes and Schell [13]

Martinez *et al.* [14] found a special sub-regime of fibrous suspensions at N equal to 16 where fibres interact but not completely locked. From their observations, the authors

defined a new model, called "Gel Crowding Number", which takes into account into account this phenomenon.

Fibre length and consistency are the most influential variables affecting formation in a paper mill. Increasing either of these parameters worsens formation. These parameters are related to the uniformity and mobility of fibres inside a paper pulp. Uniformity refers to the evenness of the mass distribution in the suspension. It can be divided into two parameters: intensity and scale. Intensity refers to the local mass variation in grammage while scale refers to the size of the zones having elevated grammage. Scale is governed by the size of the discrete elements on the system i.e. fibre length, while intensity is governed by the propensity of fibres to flocculate. This propensity is characterised by means of the Crowding number defined hereabove. It is commonly accepted that the paper uniformity is linked to the uniformity of the pulp suspension. One way to guarantee this uniformity is to use a very diluted fibrous suspension at the headbox, so as to reduce the crowding number. Another way to improve uniformity is to reduce fibre length or modify the fibre coarseness as it can be seen in equation 1.13. However, in order to guarantee a high quality commercial grade of paper, the fibre length and coarseness can not be completely modified.

Mobility refers to the ease with which these fibres can be rearranged as a result of hydrodynamic forces. It determines the extent to which the suspension uniformity can be altered during drainage on the paper machine. Mobility is clearly governed by the number of contacts and the force per contact. It is also related to the fibre coarseness when transient flocs turn into coherent flocs, i.e. coarser fibres produce coherent flocs at lower suspension concentrations than finer fibres [15].

1.3.2 Internal forces inside a floc

The number of contacts can be easily calculated using equation 1.14. But, the force per contact and the reaction to hydrodynamical forces is more complicated. Wahren [16] showed that fibres are deformed by forces generated within the shear flow. These deformed fibres tend to recover their original state once the shear stress ceases, but collisions to other fibres block this process and generate a fibrous web with internal stresses. In order to measure this, Thalén and Wahren [17] developed a new testing instrument called "elasto-viscometer". The sample is placed between two concentric cylinders. The outer cylinder is driven and the shear stress on the surface of the inner cylinder can be measured. They found that the network becomes fully constrained at an experimental onset called "sedimentation concentration" defined as the concentration of the sediment formed by gravity settling of fibres from a dilute suspension. They also showed that the shear

modulus can be expressed as a function of the fibrous suspension concentration and the sedimentation concentration, as expressed in the following equation:

$$G = G' \left(\frac{c - c_s}{0.1} \right)^{k_G} \tag{1.15}$$

where c_s is the sedimentation concentration, c is the fibrous suspension concentration. G is the shear modulus and G' can be interpreted the value of the shear modulus at consistency c_s+0.1. k_G is a coefficient depending on the pulp. In another work and using the same method, Thalén and Wahren [18] established equation 1.16 which shows that the ultimate shear stress, τ_u, can be also expressed as a function of the concentration:

$$\tau_u = \tau' \left(\frac{c - c_s}{0.1} \right)^{k_\tau} \tag{1.16}$$

In this equation, k_τ is a coefficient depending on the pulp and, similar to the previous equation, τ' can be interpreted the value of the shear modulus at consistency c_s+0.1. Combining equations 1.15 and 1.16, the shear stress can be expressed as a function of the complex shear modulus only, which gives us a more generic equation as shown in equation 1.17

$$\tau_u = \tau' \left(\frac{G}{G'} \right)^{\frac{k_\tau}{k_G}} \tag{1.17}$$

Wahren and Meyer [8] worked at larger consistencies and defined a regime of three or more contacts per fibre. In this regime, fibres are fully constrained in rotation and translation. They also noted bending forces as a source of cohesion in fibre networks.

1.3.3 Reaction of fibrous suspensions to hydrodynamical forces

The presence of fibres modifies the entire behaviour of the flow. This phenomenon was studied by several authors, [19, 20, 21, 22] among others. Fibre suspensions have a unique flow behaviour not encountered in other solid seeded suspensions. In early works, Robertson and Mason [23] identified three flow regimes of fibre suspensions in straight horizontal pipe flows: Plug, Transition and Turbulent Flow. According to Paul and Duffy [24] each regime can be subdivided into several very well identified sub-regimes as shown in table 1.3. Even though a fully turbulent flow regime is reached, it does not imply that a fully deflocculated pulp is obtained. Indeed, several authors [25, 26, 27] observed the relative motion of flocs at high flow rates in the turbulent regime.

As fibre suspensions are inhomogeneous two-phase systems, one could say that they are "fluidised" when they behave as a fluid. Care must be taken, as pointed out by

Duffy [28], because we can not use the expression "fluidisation" in fluids having parts that are not in motion (plug formation).

Regime	Friction loss behaviour	Particle/flow behaviour
Plug	Friction loss independent of velocity	Solid-solid friction dominates
	Friction loss decreases (negative slope)	Shear rate strong enough to "smooth" surface of plug. Water annular layer in laminar shear developed.
	Crossing of pulp friction loss curve with the water one	Beginning of turbulence in the thin peripheral layer. Free of fibres until the shear stress is strong enough to remove fibres from plug
Transition	Pulp friction loss curve reduced further below water	Plug diminished in size. Turbulent fibre/water annulus. Central plug acts as a solid linkage to transfer and enhance momentum.
	Maximum plug reduction (minimum of friction loss curve)	Fibre plug approximately of 20% of pipe diameter. Competing mechanism of turbulence damping by fibres and central plug momentum enhancing mechanisms are at equilibrium.
	Pulp friction loss curve moves closer to water one	Fibre turbulence damping dominates over the rest of central plug.
Turbulent	Friction loss curve remains under water curve but parallel.	No central plug left. Fully developed turbulence reached.

Table 1.3: Fibre suspension flow regimes according to Duffy [21, 24]

As it was explained by Mason [29], a dynamic equilibrium exists where transient flocs form and disperse continuously. The size of transients flocs decrease with increasing levels of shear. This mechanism was observed by Salgueiro [30] and Dietemann [31] using high-speed video analysis. This dynamic equilibrium disappears in some particular conditions, for instance in the free-jet exiting the headbox where the shear stress due to walls disappears. This situation is of capital importance for knowing the size of flocs arriving onto the forming wire. It was studied for instance by Skali-Lami [32]. In this work, Skali-Lami considered flocs as a linear viscous-elastic solid like a Kelvin-Voigt one. He got to the conclusion that a time of 20 ms of free-jet fly is needed to get flocs to grow up. According to this work, this characteristic time is independent of flow rate and depends only on the type of fibres used. Moreover, Salgueiro *et al.* [27] have seen much bigger flocs than those

described by Skali-Lami using high-speed video analysis, even though the strain rates used were much higher than the one used by Skali-Lami.

Other authors [33, 34, 35] studied another way of floc dispersion with the use of extensional flows in contracting channels. It was shown that extensional flow disrupts flocs much faster than simple shear flow, but not completely (floc fragments from the main floc remain intact). Simple shear flow acts more slowly but more efficiently than extensional flow. This floc dispersion was observed in many different ways like NMR imaging [36], X-Ray computed tomography [37], positron emission tomography [14] and wavelets transformation in digital images to get information on inner structure [38]

1.3.4 The need of a viscosity model

Another way to predict the pulp reaction to hydrodynamical forces is by the use of numerical models i.e. computational fluid dynamics. To this effect, a detailed rheological model of the pulp is needed, especially one that includes the shear viscosity of pulp and the flocculation phenomena. During the last 50 years, many authors tried to assess (or measure) the stock shear viscosity. However, this is not an easy task to do. Flocs are big enough so that the fibrous suspension cannot always be considered as a continuum. The turbulent water-annulus phenomena creates a second problem because fibres migrate from the wall region into the centre of the flow causing that almost no fibres are left in the near wall region where shear stress is maximum. Several attempts to measure the stock viscosity were made using direct and indirect techniques in order to overcome this continuum problem [39, 40, 41, 42, 43, 44]. However, owing to the complexity of the task, no meaningful values were found. More precisely, accurate values were found but for a special particular condition (type of pulp, shear strain, curl value of fibres, viscosity of liquid medium, consistency, etc.) so that no comparison can be made with other studies.

1.4 Review of hydrodynamic theory

1.4.1 Fluid flow governing equations

Every basic governing equation in fluid flow comes from conservation equations made using the Leibnitz's theorem expressed as follows:

$$\frac{d}{dt}\int\limits_{\Omega} f d\Omega = \int\limits_{\Omega} \frac{\partial f}{\partial t} d\Omega + \int\limits_{\Sigma} f\left(V_i n\right) d\Sigma \tag{1.18}$$

where Σ is the exterior surface of a control volume Ω, n is a normal vector to this surface and f is any typical physical function. In this equation, V denotes the velocity, ρ the

density of the fluid and t the time. If we take the mass of a control volume as this function, transforming then the second member of the Leibnitz's equation in a volume integration by means of the Stokes integration formulae and trending this control volume to zero, then equation 1.18, expressed in vectorial notation, becomes:

$$\frac{\partial \rho}{\partial t} + div\left(\rho V\right) = 0 \tag{1.19}$$

If density is constant then the last equation can be reduced to:

$$div\left(V\right) = 0 \tag{1.20}$$

which is the equation used to describe non-compressible fluid flows. Proceeding similarly but using the linear momentum expression as the function f in equation 1.18 we have:

$$\int\limits_{\Omega} \frac{\partial\left(\rho V\right)}{\partial t} d\Omega + \int\limits_{\Sigma} \rho V\left(Vn\right) d\Sigma = F \tag{1.21}$$

where F represents the total external forces applied to the control volume. These external forces can be divided into the weight of fluid particles plus the resultant of the external actions in contact with the surface Σ. Expressed as volume integrals, the equation becomes:

$$\int\limits_{\Omega} \frac{\partial\left(\rho V\right)}{\partial t} d\Omega + \int\limits_{\Omega} div\, V\left(\rho V\right) d\Omega = \int\limits_{\Omega} \rho g d\Omega + \int\limits_{\Omega} -grad\ \left(p\right) d\Omega + \int\limits_{\Omega} div\ \left(\tau\right) d\Omega \tag{1.22}$$

where τ is the stress tensor and g the gravitational constant. If we trend the volume control to zero once again, we get:

$$\frac{\partial V}{\partial t} + V \cdot grad\left(V\right) = -\frac{1}{\rho} grad\left(p\right) + g + \frac{1}{\rho} div\left(\tau\right) \tag{1.23}$$

which is called the Navier-Stokes equation. This equation gives the dynamics of fluid flows. If density is constant, then we get the Navier-Stokes equation in an explicit form for non-compressible fluids.

$$\frac{\partial V}{\partial t} + V \cdot grad\left(V\right) = -\frac{1}{\rho} grad\left(p\right) + g + \upsilon \Delta V \tag{1.24}$$

where υ denotes the kinematic viscosity of the fluid.

Despite of its non-linearity which disables us to attain a direct calculation of the flow for every possible case, this equation is the most important equation used in fluid mechanics and is the base of every other model used nowadays.

1.4.2 Turbulence description

The complete description of turbulence remains one of the unsolved problems in physics. As Horace Lamb has one said *"I am an old man now, and when I die and go to heaven there are two matters on which I hope for enlightenment. One is quantum electrodynamics, and the other is the turbulent motion of fluids. And about the former I am rather optimistic."*. This shows us the little knowledge we have of the real state-of-art of turbulence. Nowadays, some mathematical developments like fractals, Chaos theory and wavelets analysis can give us a little insight of a direct solution of Navier-Stokes equation in turbulent condition for very simple cases.

For other cases, some compromise must be achieved and the use of models is imposed. The first person to get a quantitative value for the description of turbulence was Osborne Reynolds in 1886 who derived the dimensionless number known a Reynolds number. It is the ratio of inertial forces to viscous forces and, consequently, it quantifies the relative importance of these two types of forces for given flow conditions:

$$\mathrm{Re} = \frac{VL}{\upsilon} \tag{1.25}$$

In this expression, V is the bulk velocity of the flow and L the characteristic length.

The transition between laminar and turbulent flow is often indicated by a critical Reynolds number Re_c, which depends on the exact flow configuration and must be determined experimentally. Within a certain range around this point there is a region of gradual transition where the flow is neither fully laminar nor fully turbulent, and predictions of fluid behaviour can be difficult. For example, within circular pipes the critical Reynolds number is generally accepted to be 2300, where the Reynolds number is based on the pipe diameter and the mean velocity within the pipe. Burger in 1939 could give a theoretical background and an explanation of this critical value. He noted that once the critical Reynolds value is attained, the instabilities inside the fluid amplified themselves by a certain wavelength. Burger has also shown that the origin of these instabilities is related to the non-linear term of the Navier-Stokes equation. A clever way to simplify the description of turbulence is by introducing a statistical concept to decompose the velocity variable into its mean value, $\overline{u}$, plus its fluctuation, u', as described as follows:

$$u_i = \overline{u_i} + u_i' \tag{1.26}$$

If we introduce this last equation into the Navier-Stokes equation and then apply the mean operator to every term we get a set of equation:

$$\begin{cases} \dfrac{\partial \overline{u_i}}{\partial t} + \overline{u_j}\dfrac{\partial \overline{u_i}}{\partial x_j} = -\dfrac{1}{\rho}\dfrac{\partial \overline{P}}{\partial x_i} + \dfrac{\partial}{\partial x_j}\left(\upsilon \dfrac{\partial \overline{u_i}}{\partial x_j} - \overline{u_i' u_j'}\right) + g_i \\ \dfrac{\partial \overline{u_i}}{\partial x_i} = 0 \end{cases} \tag{1.27}$$

which is generally called the "Reynolds equations". In vectorial notation we get:

$$\begin{cases} \dfrac{\partial \overline{\mathbf{V}}}{\partial t} + \left(\overline{\mathbf{V}} \cdot \mathbf{grad}\right)\overline{\mathbf{V}} = \dfrac{1}{\rho} div\left(\overline{\sigma} - \rho \mathbf{R}\right) + g \\ div\left(\overline{\mathbf{V}}\right) = 0 \end{cases} \tag{1.28}$$

where $\mathbf{R}$ is the vector product of the velocity fluctuation vectors $\mathbf{R} = \overline{\mathbf{V}' \otimes \mathbf{V}'}$ and is called Reynolds tensor. This tensor becomes an infinite series of equations. So, a closing hypothesis must be taken to be able to solve equation 1.28.

We solve this tensor by an external model and then we introduce this result into equation 1.28 so to get the mean value of the flow fluctuation generated by turbulence.

1.4.3 Relation between turbulence and flocculation

Dispersion of fibre flocs by turbulent forces is an important part of papermaking process and is crucial for sheet formation. Anderson [45] developed a model in which the probability of the rupture of fibre flocs was equal to the product of the probability that a certain fluid stress would occur and the probability that the strength of the floc was lower than this stress. Wagle *et al.* [46] stated that the floc breakup process in a steady shear field started as a global deformation and fragmentation at large scale depending mostly on the shear rate. It was followed by a local small-scale erosion process, for which the floc size reduction was modelled as an exponential rate process in which the rate constant was a function of the shear stress. Hourani [47, 48] assumed that a "dynamic equilibrium" exists between fibres and flocs and that the mean floc scale was equal to the mean turbulent eddy size. Later on, Steen [49] presented a concept to explain fibre flocculation in turbulent flows. He showed that large eddies will contain local fibre networks (flocs) while the smallest vortices will contain only single fibres or no fibres at all. This can be explained from the turbulent energy transfer from larger to smaller scales by vortex stretching (Kolmogoroff's turbulent energy cascade). During this energy transfer, flocs are deformed. Floc breakup is probable if the deformation forces are larger than the flocs internal network strength. The length scale of the straining vortices will be of the same order as the floc scale. Eddies of a smaller scale will agitate the outer part of the floc, making the floc weaker and making rupture more likely. Flocs of one length scale can be transported by turbulent eddies of larger scale, and floc collisions will occur. These

collisions cause build-up when the contact time is long enough for the newly formed local floc to settle.

In this concept, the rupture of flocs is linked to the turbulent energy cascade, whereby eddies interact with other eddies of adjacent length scale. However, the floc aggregation process is composed of a small-scale activation and a large-scale collision and network settling. Steen developed a useful parameter called the flocculation intensity defined as:

$$I_f = \frac{\sqrt{\overline{c'^2}}}{\overline{c}} \tag{1.29}$$

where $\overline{c}$ is the average fibre consistency and $\overline{c'^2}$ the mean-square of the consistency fluctuations. This parameter is equivalent to the coefficient of variation of the consistency and is closely related to another dimensionless number called turbulent intensity (I_t) defined as:

$$I_t = \frac{\sqrt{\overline{u'^2}}}{\overline{u}} \tag{1.30}$$

I_t represents the relationship between the root-mean-square of the turbulent velocity fluctuations and the Reynolds averaged mean velocity. The similarity between both equations explains most of the flocculation theory developed by Steen. One of the major conclusions made by Steen is that the break-up of flocs takes place when the frequency of the turbulent eddies is resonant with some eigen frequency of the flocs. However, one of the weak points of his work is that he assumed that the turbulent structure is unchanged in the presence of fibres.

1.5 Papermaking process description

Generally speaking, a typical paper machine is divided in two sections, the wet section and the dry section. Screening, refining, chemical mixing and forming are, among others, some of the most important unit operations of the wet section. The main objective of this section is to prepare the cellulose fibres for a certain grade of paper. The understanding of hydrodynamics of the paper pulp in this section is essential for manufacturing a good paper quality. Sheet forming is the heart and the most delicate operation inside a paper machine. A good paper sheet formation depends on several variables: freeness, consistency, fibre orientation, intensity of flocculation, temperature, level of vacuum applied, pH, amount of fibre fines and mineral fillers are, among others, the most important ones. In terms of hydrodynamics, formation depends on the creation of a perfect plane jet, free of disturbances, that will land at a certain angle and speed onto a permeable and mov-

able weave called "fabric". Formation becomes then, a compromise between the proper functioning of the hydrodynamical injector (called "headbox") that creates the plane free jet and the drainage level and speed of the fabrics.

1.6 Headbox description and working principle

The main functions of a headbox can be listed as follows:

1. Evenly distribution of the stock especially in the cross-direction.
2. Small scale, high energy turbulence generation for a better deflocculation
3. Flow acceleration to a nearby speed of fabrics
4. Fibre orientation
5. Transformation of the geometry of the flow
6. Machine direction pressure pulses attenuation
7. Grammage control either by local dilution or by micro adjustments of slice lip.
8. Stock jet orientation and control (angle and contraction coefficient)
9. Multi-layer capability

Considering all these constraints, the design of a perfect headbox is a hard thing to do. Historically, headboxes kept several errors from one design to another. These errors were originated by the misunderstanding of the fibrous suspension rheology or by some papermakers wrong believes of those years. The first kind of headboxes used in modern papermaking was the one called "Open headbox" as shown in figure 1.5. This was the first logical solution for an evenly distribution of stock onto the former. Then, during the fifties, air-cushioned headboxes were developed to avoid pressure variations generated at the fan-pump as shown in figure 1.6(a) and in figure 1.6(b). Finally, hydraulic headboxes appeared in the mid sixties to give a solution for the high-speed production paper machines. Since then, several optimisations were made but no major changes were proposed. A typical headbox is classically composed by different sections:

1. Flow spreader
2. Stabilisation chamber
3. Turbulence generator
4. Nozzle
5. Slice (or upper lip)
6. Lower and upper lip control (if exists)

A better description of all this parts is made hereinafter for a complete understanding of the headbox functioning.

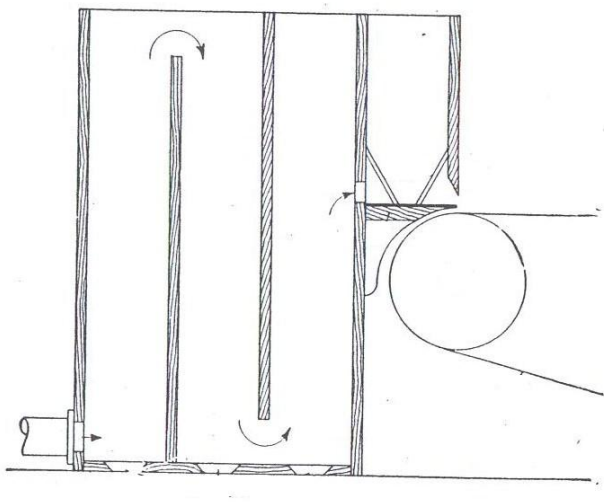

Figure 1.5: Open headbox

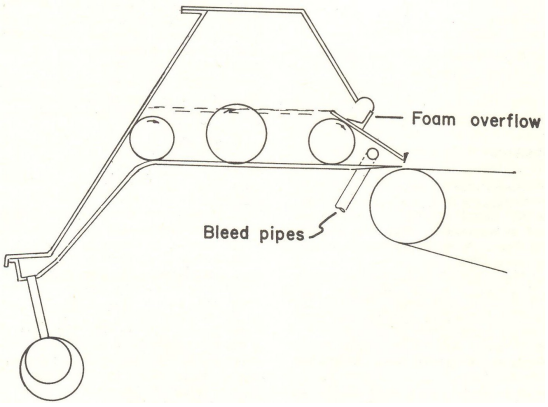

(a) Air padded headbox

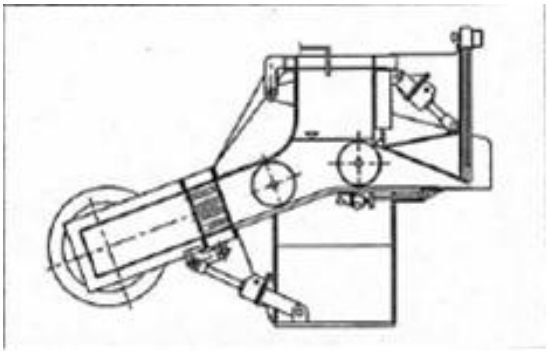

(b) Pressure headbox

Figure 1.6: Different headbox technologies

1.6.1 Flow spreader

The flow spreading was neglected for a long period of time: it was considered as a simple pulp arrival into the headbox. The funny thing is that, if a perfect flow spreader were made, this would make the headbox almost superfluous. The main function of the headbox was then to eliminate or correct the effects of poor flow spreading.

Several kinds of flow spreaders were developed. Chronologically, they can be ordered as follows:

1. Expanding channel, diverging in the plane of the sheet and converging in the thickness, in the machine direction (see figure 1.7(a))
2. Division of flow in multiple branch flows (see figure 1.7(b))
3. Cross-flow distribution (see figure 1.7(c) and figure 1.7(d))
4. Tapered flow distribution (see figure 1.7(e))
5. Radial iso-pressure distribution (see figure 1.8)

Every new design was conceived to eliminate previous problems and to try to inject the stock into the headbox at a uniform velocity, with no cross machine component and with a turbulence scale low enough to avoid flocculation, recirculation flows and settling.

The radial distribution, which enables a pressure control thanks to an air-cushioned tank and an even distribution inside the headbox via several rubber hoses, is one of the best solutions known up to now because of the wide range of possible flow rates and not found in others technologies. This spreader allows a better grammage control by local dilution. It also allows reducing the size of headboxes which is an important concern in modern paper machine design.

1.6.2 Stabilisation chamber

The first concepts for this stabilisation chamber was to give a high turbulent impulsion to the flow and then decelerate the flow to create an even plug flow that will be deposited on the fabrics. It was believed that the fibrous web was formed inside the stabilisation chamber and then, if no turbulence (or instability) were present at the rest of the headbox, the fibre distribution would be almost perfect. Some examples of this kind of chambers are shown in figures 1.9(a) and 1.9(b). Nowadays, another kind of chamber is used but for a different reason. A minimum length is required for evening the velocity profile after a bent or an irregularity inside the pipes. This hydrodynamical evenness is searched with modern stabilisation chambers. It is also known that flocculation is a very fast process

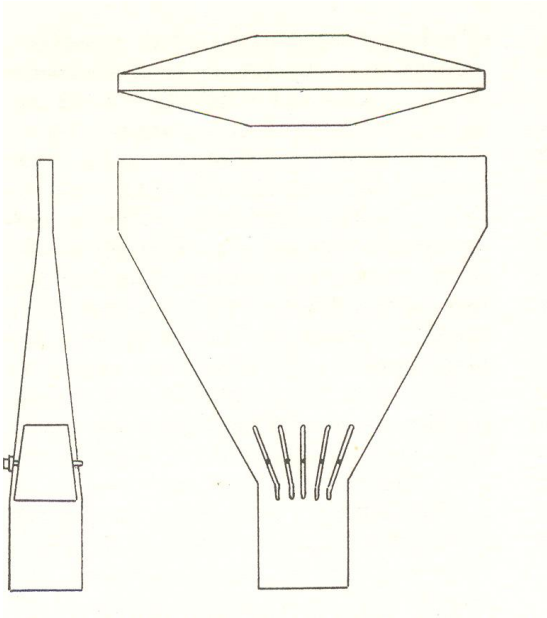

(a) Expanding channel flow spreader

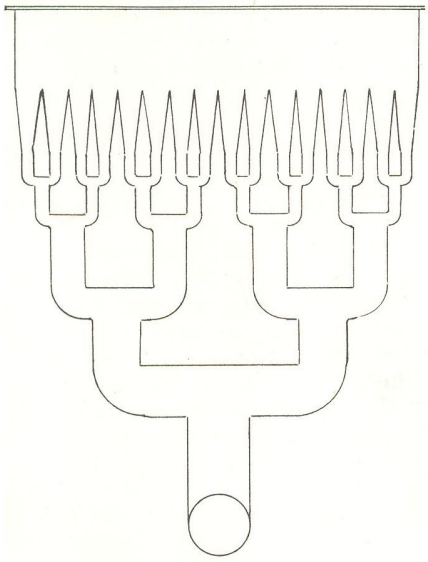

(b) Multiple branch flow spreader

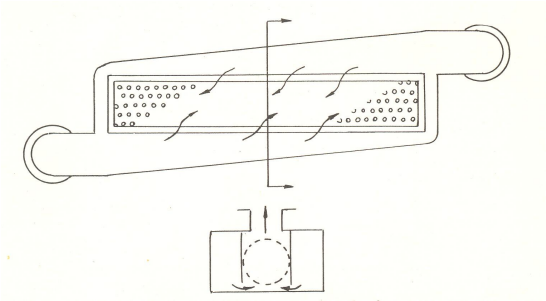

(c) Cross flow spreader

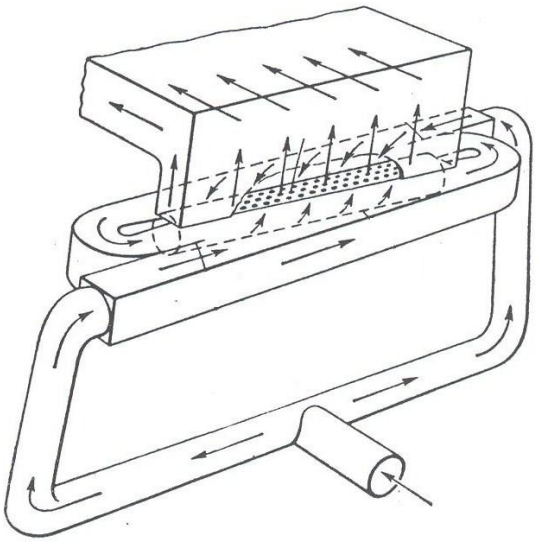

(d) Cross flow spreader 3D view

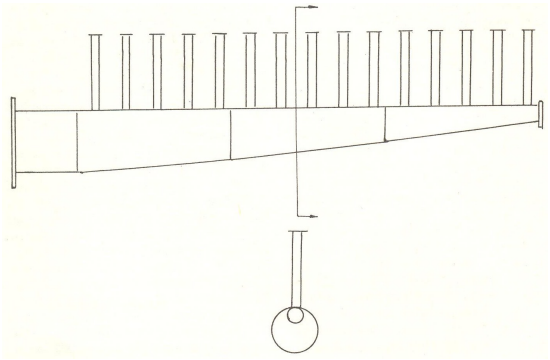

(e) Tapered flow spreader

Figure 1.7: Different spreader technologies

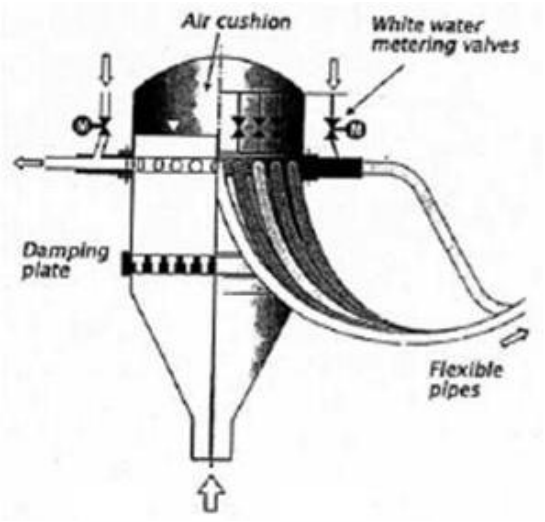

Figure 1.8: Radial iso-pressure flow spreader

that will appear whenever the pulp is decelerated. In modern equipment, stabilisation chambers are of a similar cross section as the arrival tubes to maintain the speed rates.

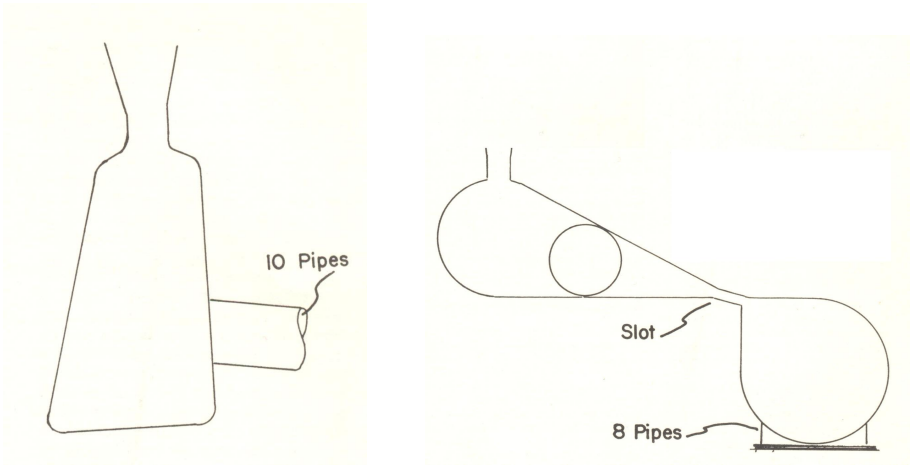

(a) Stabilisation chamber (commonly called explosion chamber)

(b) Stabilisation or explosion chamber

Figure 1.9: Several stabilisation chamber technologies

1.6.3 Perforated rolls and turbulence generators

In hydrodynamics applications, a way to obtain small scale turbulence and evenness of the velocity profile is to introduce perforated plates (turbulence generators) in the path of the flow. This practice was thought to be the solution for the requirements in papermaking. Nevertheless, the fear to clog up the whole installation motivated the development of a self cleaning system called perforated rolls, frequently used inside a headbox. The idea is very simple: A perforated roll turns at low speed, so if a plug is formed when it turns all over, it will be cleaned. This solution worked but the generated instabilities and the apparition of hydraulic headboxes for high-speed machines forced the development of the step turbulence generator shown in figure 1.10. The idea is to produce high turbulence intensity and then a regular diverging channel (or a collection of steps) re-arranges the flow into the nozzle. The drag generated by eddies inside the turbulence generator is supposed to break up the flocs and to keep a certain amount of small scale until the flow reaches the nozzle. The main problem of this solution is that there is no way to control the amount of energy introduced inside the system and, even more, we do not know how this energy is dissipated in the liquid medium or on the fibres.

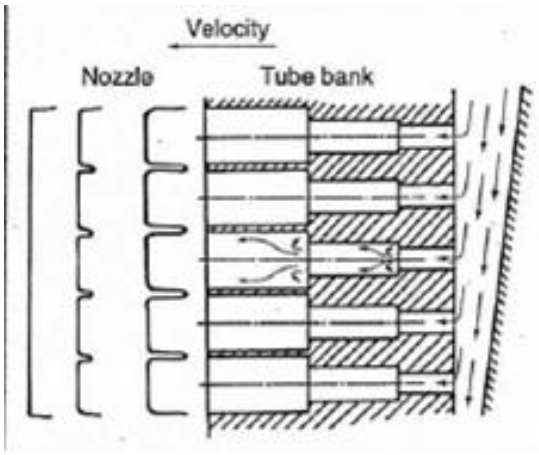

Figure 1.10: Escher Wyss Step turbulence generator

1.6.4 Nozzle, slice and lips control

The main function of the nozzle is to get a smooth gradual acceleration of the flow with a low level of turbulence, until the fabrics speed (or a close speed) is attained. The second function is to reduce the depth of the jet that will land on the fabrics so to have the proper grammage for a given wire speed and concentration. Older designs used to have a vertical "knife" assembly (see figure 1.12(a) and figure 1.12(b)). The increase in machine speed standardised the use of converging nozzles (see figure 1.11). Depending of the attack angle (the converging angle) of this nozzle, a certain amount of turbulence can

be obtained in the jet. If this turbulence is too high, this can cause the jet to disintegrate on hitting the fabrics, or even worse before reaching it.

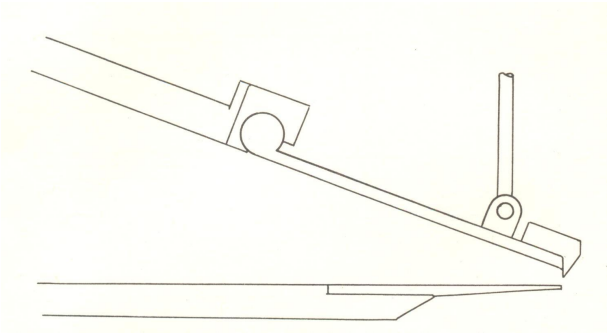

Figure 1.11: Converging nozzle configuration

The angle at which the jet hits the fabrics and the place of the impingement are of paramount importance to sheet formation. These values depend on the lips control. The jet shape depends on three geometrical parameters described in figure 1.12(c), where b is the slice opening of the headbox, B is the acceleration rate of this nozzle and L is the position of the lower lip with respect to the slice opening.

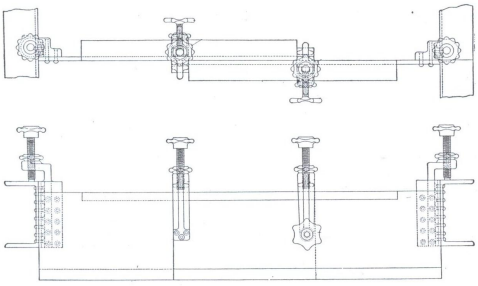

(a) Knife type slice

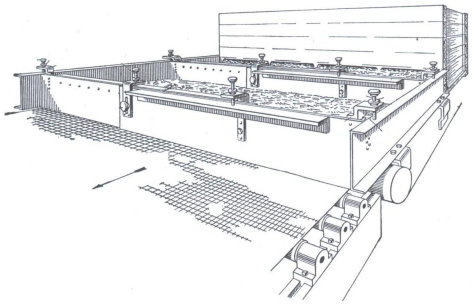

(b) Knife slice after open headbox

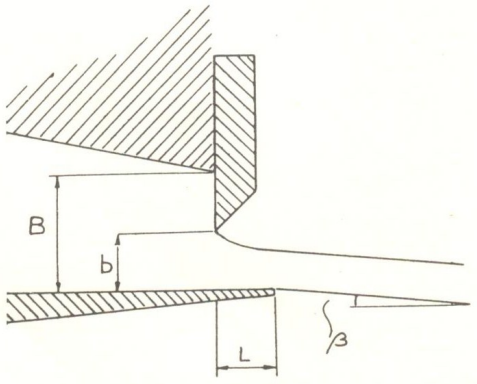

(c) Geometrical parameters of the slice

Figure 1.12: Different nozzle technologies for jet control

The jet angle depends on the ratio L/b and the ratio b/B. Some technical solutions were developed to get a proper control of these ratios thanks to movable or deformable devices as shown in figures 1.13(a), 1.13(b) and 1.13(c).

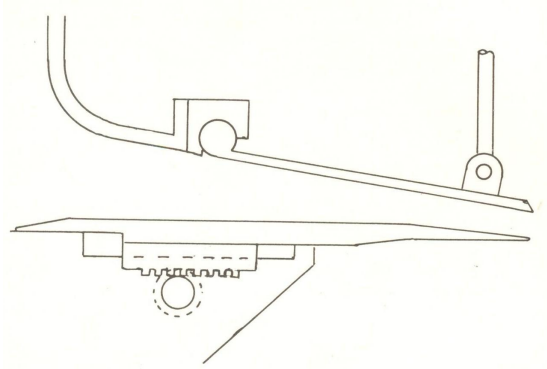

(a) One option for jet control

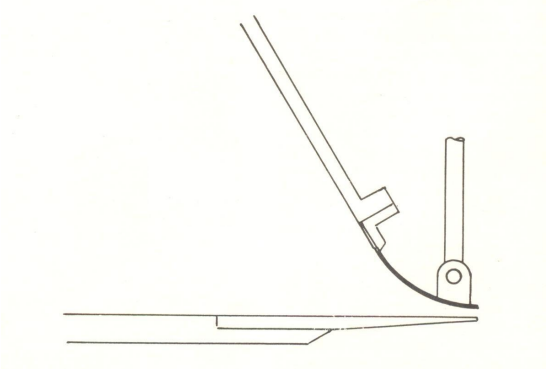

(b) A second option for jet control

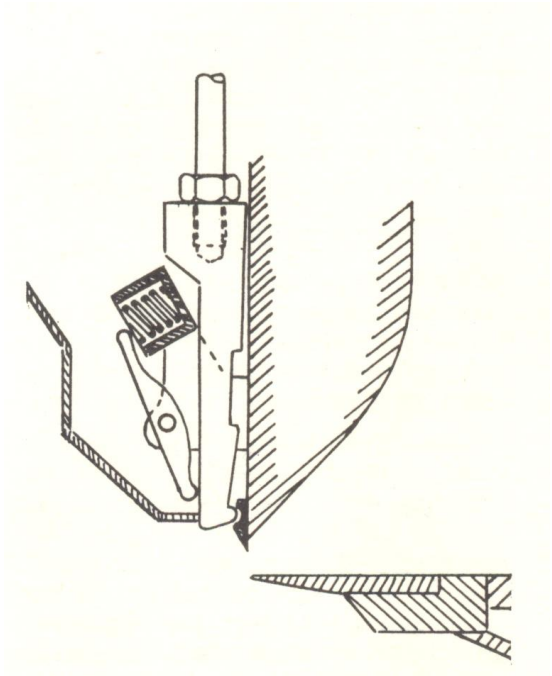

(c) A third option for jet control

Figure 1.13: Different nozzle technologies for jet control

1.7 Conclusions of this chapter

In this chapter, a comprehensive review of the literature about the behaviour of fibrous suspensions was made. It could be seen the complexity and the little understanding of some of these processes. A brief description of some of the elements composing a headbox

was also made. It is important to understand that most of the improvements made at this forming unit aimed at obtaining a more uniform suspension. This uniformity is closely related to the gain in quality of the paper and a better control of this quality. However, it was pointed out that not only uniformity, but also fibre mobility, are the key parameters for ensuring a good formation. Even though a flocculated suspension is observed, if fibre mobility is good, a good formation could be achieved. This mobility is related to hydrodynamical forces (especially turbulent ones), fibre characteristics and the force of contacts between fibres. In the next chapter a detailed analysis of hydrodynamic forces (turbulent intensity fields) of each part of the headbox will made. Indeed, it is important to know how much energy is used for obtaining a uniform pulp and how it is applied.

Chapter 2

Study of the efficiency of a headbox and its dimensioning

Fibre delivery onto the wire is achieved by a system (headbox) which contains several elements. The action of each of these elements to the fibrous suspension is essential to obtain a satisfactory quality grade of paper. The main objective of this chapter is to analyse the energy efficiency of each device inside a headbox. The motivation of this work comes from a visual observation of a working headbox where it was noticed that the flocculation state of a fibrous suspension did not very significantly change from one element to another. This would mean that the energy used inside a headbox for deflocculation was not properly used. We have decided, then, to make an individual study of the most important elements involved, in order to get a clearer picture of their individual influence upon the fibrous suspensions. Then, in a second time, the inter-influence of these elements inside a headbox was studied in order to make a global conclusion from an energetical point of view and propose some optimisation designs.

2.1 Headbox setup and testing conditions

Measurements were made at a pilot hydraulic headbox with approx. 50 cm cross section width, a lip opening varying from 8 to 30 mm. This headbox is attached to a closed circuit of a 12 cubic metre tank connected to a fan pump as shown in figure 2.1. The flow rate arriving to the headbox is controlled by a by-pass connection and a valve giving a working flow range from 0 to 400 m^3/h. There is an iso-pressure distributor which delivers the flow to the headbox thanks to 50 mm in diameter flexible pipes. The headbox side walls are made of Plexiglas to allow visual observation. The tube bank used was a two step diffuser, with a 17 mm in-diameter inlet and a squared column ordered outlet.

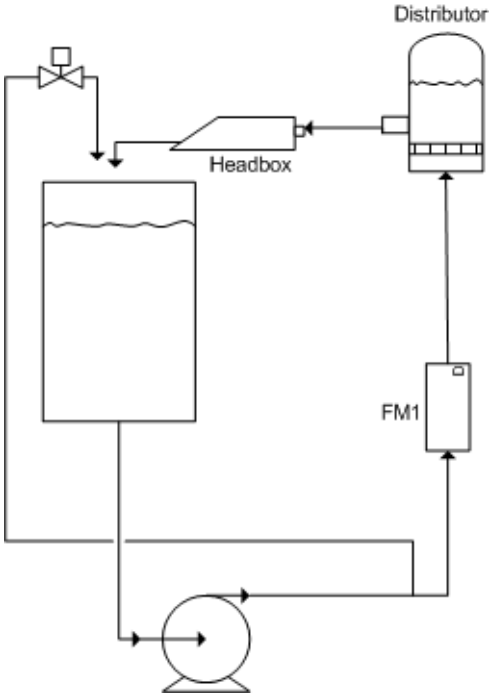

Figure 2.1: Headbox setup

Six pressure sensors were placed all along the headbox in order to measure the pressure loss at different points, especially at the tube bank and at the nozzle, as it is shown in figure 2.2. Three others sensors were placed at the bottom lip of the headbox, to study the position of the vena contracta.

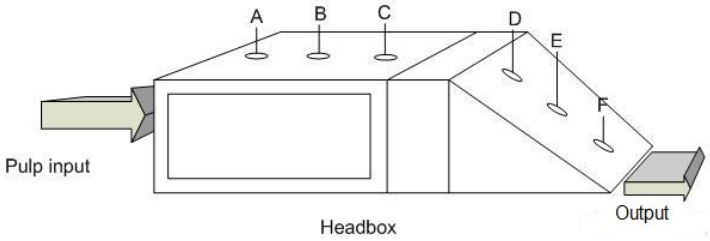

Figure 2.2: Headbox pressure sensors detail

Real industrial flowing conditions were tried to be kept all along our experimental protocol, even if this means adding other difficulties to our analysis i.e. opacity of pulps due to concentration.

Three different types of pulps were chosen for this study, one hardwood (acacia), one softwood (maritime pine) and one mixed pulp (60% hardwood and 40% softwood). The physical properties of these pulps and testing conditions are summarised in table 2.1.

Type of pulp	Mean fibre length, mm	Coarseness, mg/m	°SR	Concentration, g/L Crowding factor @ 5 /L	°C
Hardwood	0.67	0.0406	60	5, 10, 15, 20 275	20
Softwood	2.53	0.14	30	5, 10, 15, 20 1145	23
Mixed pulp	1.32	0.10	43	5, 10, 15 330	22

Table 2.1: Physical properties of fibre suspensions and operating conditions

Obviously, considering the crowding factor, there must be continuous contacts between fibres in these concentrated suspensions which must be flocculated. As it was seen in the previous chapter, forming is closely related to the hydrodynamical forces acting inside a headbox. To better understand these forces we decided to study each element that composes a headbox separately. According to the importance of their action on the paper quality and considering that they are present in every commercial headbox, three main elements were kept in this study:

- The stabilisation chamber.
- The turbulence generator (or tube bank).
- And the nozzle section.

2.2 Study of the stabilisation chamber

The stabilisation chamber of old paper mills played (or it was believed to play) a major role in forming. It was believed that forming was made at the stabilisation chamber and then this web was distributed onto the fabrics for a water extraction. Nowadays, a hydrodynamical reason is given to keep this chamber. Therefore, we studied the behaviour of pulp in different hydrodynamic test benches and then made an application to a stabilisation chamber.

2.2.1 Study of pulp behaviour in a straight pipe

It is well known that after a hydrodynamical disturbance, i.e. the passage through a bend or a pump, a fluid flow needs a certain amount of distance to recover a stable velocity profile. This distance was measured several times with a homogeneous fluid like water, but can we consider that the same amount of distance is needed with a fibrous suspension?

In order to be able to answer to this last question we have to understand first a general fibrous suspension flow. To this effect, we used a fluid mechanics test bench designed

to study the pulp flow at industrial conditions. The first circuit of this test bench (see figure 2.3) is a closed loop circuit connected to an agitated two cubic metre tank. The agitator acting inside this tank is powered by a motor controlled by a speed regulator; it was especially designed to ensure a homogeneous fibrous suspension. The pulp is then pumped into an eight metre long return pipe, 80 mm in-diameter. Most of this circuit is made in Plexiglas so as to study the flocculation state of the pulp at different flow rates at every point of the circuit. The pump in this circuit is also controlled by a speed regulator in order to have a precise control of the flow rate between 0 and 180 m^3/h. The mean flow rate was measured by a ferromagnetic flow meter and a mass flow meter. The choice of this double measuring system is to get a more precise measurement of the flow rate. The linear pressure drop was measured at the last four metres of the circuit, in order to be sure that the flow is completely developed and the velocity profiles are not disturbed by the presence of other devices (bend, valve, etc.). The linear pressure drop was measured by a 50 mbar differential pressure sensor. The distance between the pressure taps was chosen according to the measuring range of this sensor.

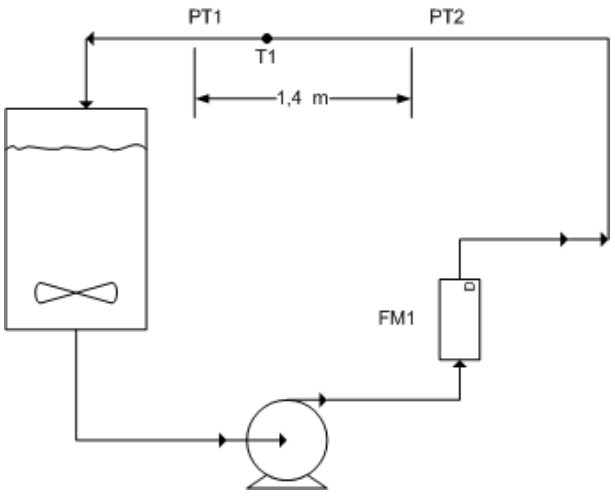

Figure 2.3: Hydrodynamic test bench

The flow regimes of each pulp were determined for every consistency. For this we have plotted a Cartesian representation of the bulk flow velocity as a function of the friction loss, as we can see in the following figures 2.4(a), 2.5(a) and 2.6(a). It is advised in Tappi Information Sheets 0410-14 [50] to represent these graphs in a double-log diagram. This was made for figures 2.4(b), 2.5(b) and 2.6(b). This representation should make the determination of the changes in the flow regime easier because it enhances the plot scale in low velocity ranges i.e. between 0.1 and 1 m/s, while the Cartesian representation gives us a more detailed description of the flow regimes at high velocity ranges.

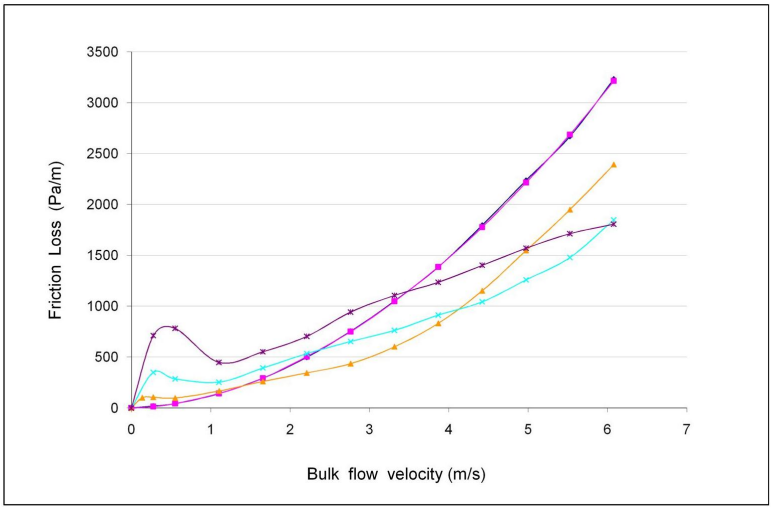

(a) Cartesian representation

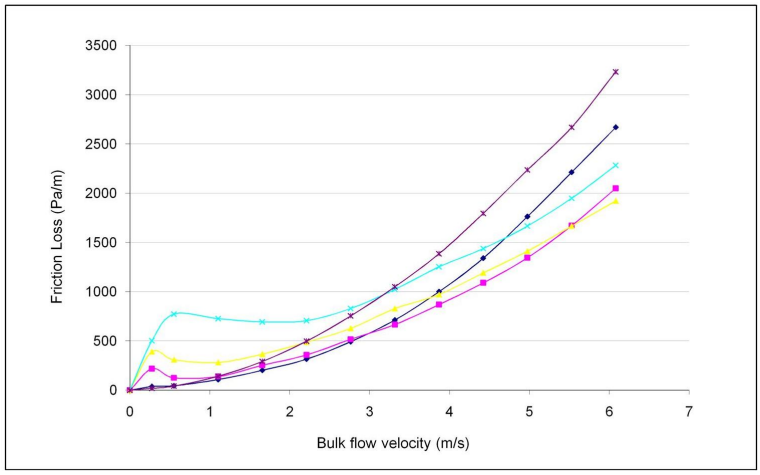

(b) Double log representation

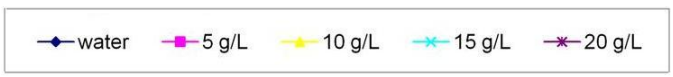

(c) Legends

Figure 2.4: Friction Loss in a straight pipe for hardwood pulp

In figure 2.4(a) we can see that for a hardwood pulp the plug regime begins from zero and extends to 0.5 m/s and then the intermediate regime varies according to the consistency. It goes from about 0.5 m/s up to 1.3 m/s and then we can consider the flow in a turbulent regime. If we examine the figure 2.4(b) we can see that the 5 g/L pressure loss curve is almost the same as the water pressure loss curve. For all the other curves we can see that they cut the water line at different positions (velocities). This intersection is the onset of the drag reduction, where friction loss with pulp is lower than with water.

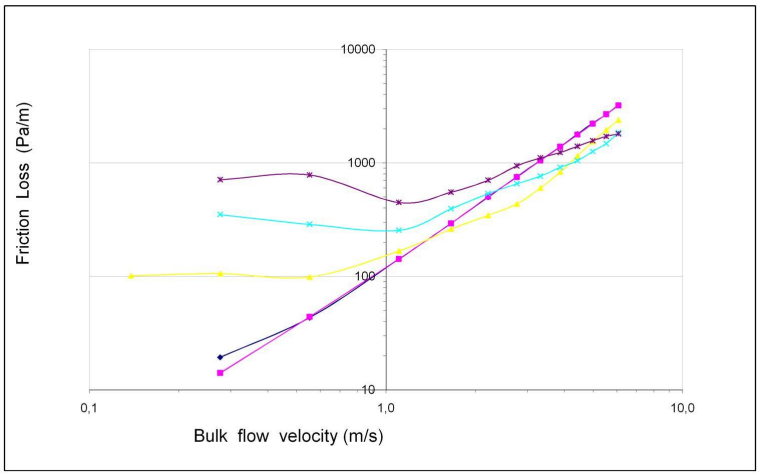

(a) Cartesian representation

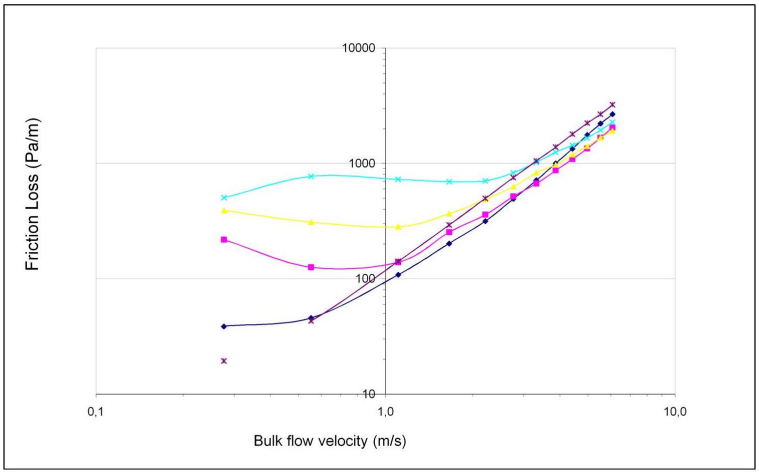

(b) Double log representation

(c) Legends

Figure 2.5: Friction Loss in a straight pipe for softwood pulp

In figure 2.5(a) we can see that for softwood pulp there are some variations depending on the consistency of the pulp: the plug regime begins from zero and extends to about 0.6 m/s (at low consistencies we can say that it is lower, about 0.3 m/s), then the intermediate regime varies from 0.3 m/s up to 0.5 m/s for the lower consistency and from 0.6 m/s up to almost 2 m/s for the higher consistency, then the turbulent regime begins. In figure 2.5(b) we can see that the regimes are quite easy to distinguish and there is no curve that coincides with the water reference. As usual, the drag reduction point varies very much depending on the pulp consistency. There is a fair agreement between the values obtained in the present study and the formula proposed in the Tappi TIS 014 for chemical pulps which gives the value of the velocity at drag point as a function of the consistency, i.e. $V_{dr} = 1.22 \cdot C_m^{1.4}$.

In figure 2.6(a) we can see that the plug regime goes up to 0.3 m/s, then the intermediate regime varies with the consistency. It goes from 0.3 m/s up to 0.5 m/s for the 5 g/L pulp and from 0.3 m/s to about 1 m/s for the higher consistencies. In figure 2.6(b) we can see that, as in the previous cases, there is a quite big deviation from the water pressure loss curve.

One interesting conclusion is obtained from a simple observation of the previous graphs. The fact that the headloss is smaller for any pulp at high industrial flow rates, i.e. for flow velocities greater than 3 m/s, means that the apparent viscosity of the pulp is smaller than pure water. This is a very important conclusion because it would mean that designing a circuit with pure water will give us a security coefficient to allow the passage of any pulp through the installation. However, care must be taken if the flow speed is slower than 2 m/s because the headloss, as it was seen, could be almost doubled for the pulp compared to water.

For all the previous cases, the water reference is a measured value. We noticed that there is a little deviation between this reference and a theoretical water reference. The difference between a measured value and a theoretical one is so little i.e. less than 10 Pa/m (0.1 mbar/m), as shown in Figure 2.7, that we can neglect it. This is thanks to the accuracy of the pressure sensor used and the possibility of zero shift. Moreover, the biggest difference appears for non-industrial flow rates which are not taken into account in this work. The experimental curve could therefore be kept as a reasonable reference.

Visual observations

Now that the flow regimes are established for these pulps, we need to get acquainted with the flocculation state at different flow rates. For this a tracing liquid was chosen for a visual determination of the mixing scale at different points of this circuit. The tracer chosen was a fixed volume of a concentrated solution of $KMnO_4$. This tracer is quite

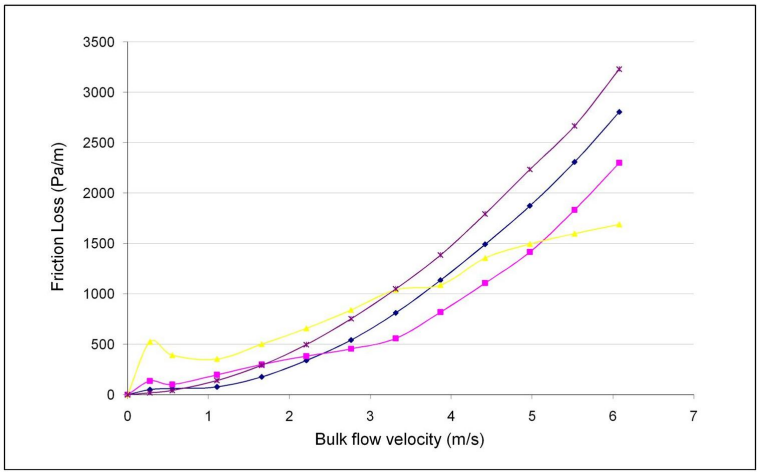

(a) Cartesian representation

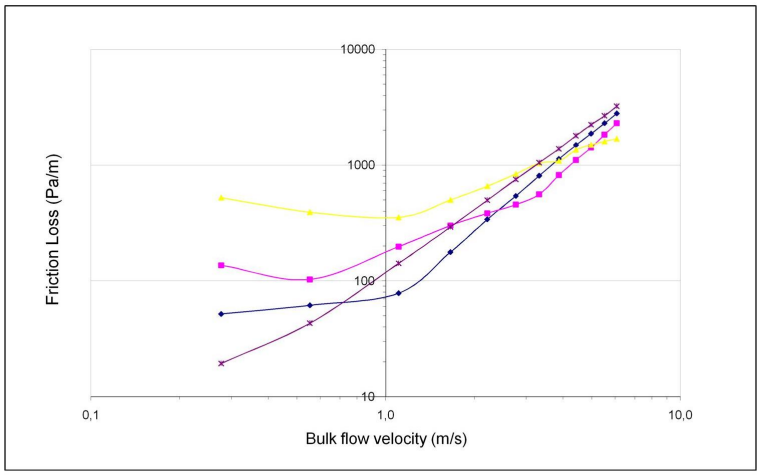

(b) Double log representation

(c) Legends

Figure 2.6: Friction Loss in a straight pipe for mixed softwood and hardwood pulp

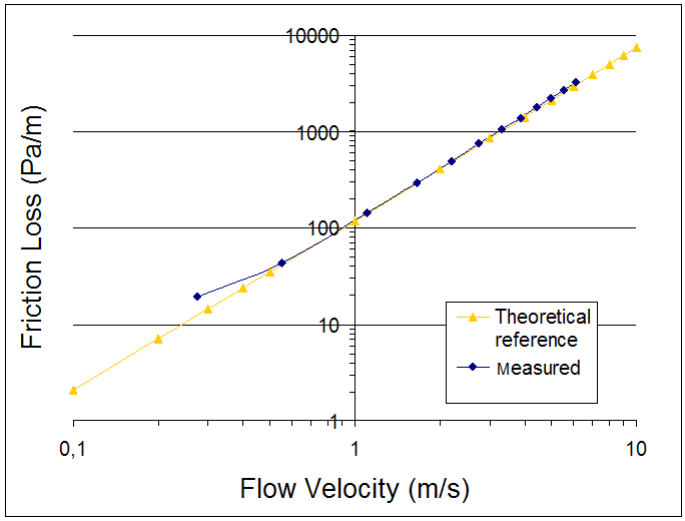

Figure 2.7: Friction Loss difference in a straight pipe - comparison between theoretical and experimental values for water

useful because of its strong colour at the injection point and its ability to "disappear" by oxidation later on. Considering the small volume injected during the experiment, no noticeable modification of pulp properties was detected. This tracing liquid was injected by a micro-volumetric pump. A Sony© digital-Camcorder was used at 25 frames per second to capture the evolution of this tracer in the liquid. As it was expected, at very high flow rate (or flow speed over 5 m/s) the mixing in mass is total for every fibrous suspension. In other words the turbulent scale at the near wall region is strong enough to produce a homogeneous distribution of the tracer and no tracer can be observed afterwards. At a medium flow rate (or a flow speed near 2.5 m/s) the tracer is not evenly distributed in the bulk. There are still some pink zones at the bottom half of the pipe (where the tracer injection was made) for most of the pulps. However a difference between a diluted hardwood pulp and a strong consistency softwood pulps was noticed. Indeed, in the first case no tracer was visible whereas no mixing takes place in the second one. Finally, at very small flow rates (flow speed under 1 m/s) the tracer remains in the near wall region: there is absolutely no mixing in the mass for every pulp (except for some diluted hardwood pulps). This observation confirms the plug theory explained before in chapter 1.3.

Images were taken at different points of the circuit using a MotionScope© 8000s High speed camera from Redlake. This camera has a charge-coupled device (CCD) allowing an 8000 images per second capture. However, the resolution obtained at this very high speed is only 60 pixels by 68 pixels. The maximum resolution got with this camera is 480 pixels by 420 pixels at 250 frames per second. These resolutions are not enough to get a detailed image of the deflocculation process. Anyway what wanted to verify in this work

is the dynamic equilibrium between deflocculation and regeneration of flocs for different flow rates, and in this case the resolution is sufficient. This camera was used then for a detailed observation at certain critical points of the circuit. The results are quite encouraging and verify our findings and measurements. At every flow rate, even at the highest ones, flocs were found at the near wall region. This region is where the highest shear rate is, so we can conclude that biggest structures were also present in the axial region of the pipe. There was only a reduction in size for the flocs found at the highest flow rate. This is important to know, because it means that the shear rate can not break all the flocs inside the flow and furthermore it means that as soon as the flow speed is diminished, flocs are reformed and grow in size.

Non-invasive velocity measurement

To verify the existence of a plug, a non-invasive velocity testing method was used. We determined velocity profiles of the solid particles thanks to Pulsed Ultrasonic Doppler velocimetry. Ultrasonic Doppler velocimetry was originally used in the medical fields but, nowadays, this technique is used in other areas, especially in fluid dynamics. It started to be used in pulp and paper research centres at the beginning of this century. PUDV principle can be summarised as follows [51]: it detects and processes many ultrasonic echoes issued from pulses reflected by micro particles contained in a flowing liquid. When we hear the words Ultrasonic Doppler Velocimetry, we think directly that the velocity is measured by finding the Doppler frequency in the received signal as a Laser Doppler velocimeter does. In fact, in Pulsed Ultrasonic Doppler Velocimetry, this is never the case. The velocities are derived from shifts in positions between pulses and the Doppler effect plays a minor role. In PUDV, instead of emitting continuous ultrasonic waves, an emitter sends a short ultrasonic burst periodically and a receiver continuously collect echoes issued from targets that may be present in the path of the ultrasonic beam. By sampling the incoming echoes at the same time relative to the emission of the bursts, the shift of positions of scatters are measured, as shown in Figure 2.8. If we consider only one particle present along the ultrasonic beam, as illustrated in Figure 2.9, the depth P of this particle can be computed from the knowledge of the time delay T_d between an emitted burst and the echo issue from the particle as follows:

$$P = \frac{c \cdot T_d}{2} \tag{2.1}$$

where c is the speed of the ultrasonic wave in the liquid. If the particle is moving at an angle in relation to the axis of the ultrasonic beam, its velocity can be determined by computing the variation of its depth between two emissions separated in time by T_{prf}:

$$P_2 - P_1 = v \cdot T_{prf} \cdot \cos\theta = \frac{c}{2} \cdot (T_2 - T_1) \tag{2.2}$$

The time difference $(T_2 - T_1)$ is always very short, most of the time less than a microsecond. Therefore, it is advantageous to replace this time measurement by a measurement of the phase shift of the received echo.

$$\delta = 2 \cdot \pi \cdot f_e \cdot (T_2 - T_1) \tag{2.3}$$

where fe is the emitting frequency. With this information the velocity of the target is expressed by:

$$v = \frac{c \cdot \delta}{2 \cdot f_e \cdot \cos\theta \cdot T_{prf}} = \frac{c \cdot f_d}{2 \cdot f_e \cdot \cos\theta} \tag{2.4}$$

This last equation gives the same result as the Doppler equation but one should be always aware that the phenomena involved are not the same.

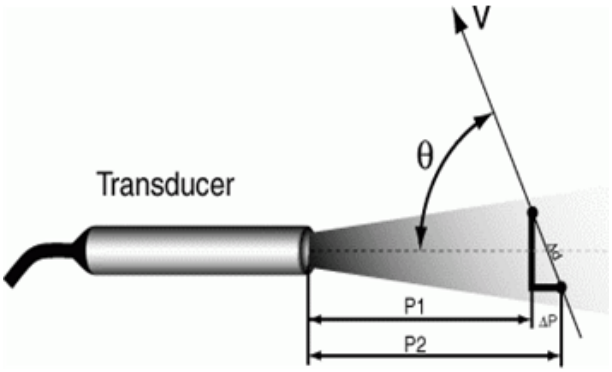

Figure 2.8: Working principle of PUDV

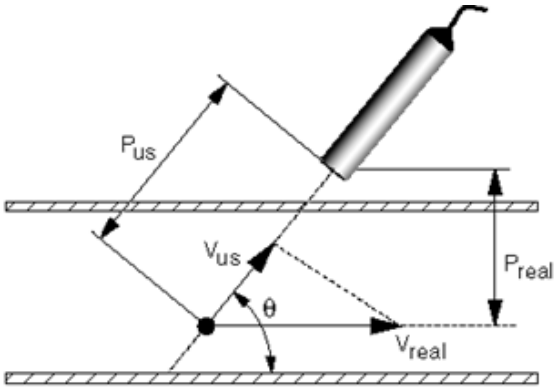

Figure 2.9: Detail of PUDV working principle

In order to minimise the aliasing phenomena the time difference between two emissions was carefully chosen. Similarly, the impedance of the pipe wall material, where the measurements were made, was chosen to recover the maximum amount of the emitting

energy. It should be noticed that all the velocity values given by the Pulsed Ultrasonic Doppler Velocimeter were verified, by calculating the flow rate thanks to a numerical integration of the velocity profiles, see Equation 1. The calculated flow rate was then compared to the measured one.

$$Q = 2 \cdot \pi \cdot \int_0^R r \cdot u\,(r) \cdot dr = 2 \cdot \pi \cdot \sum \frac{(r_i \cdot u_i + r_{i+1} \cdot u_{i+1})}{2} \cdot (r_{i+1} - r_i) \tag{2.5}$$

Figure 2.10 shows that there is a good agreement between the calculated flow rate and the measured flow rate. Less than 5% variation was found between these values. The variations may come from the accuracy of both systems, especially at high flow rates. We know that the PUDV is very sensitive to the incident angle and this can generate a systematic error of about 2 or 3%. We also know that the flow meter has a similar accuracy. Therefore the observed differences are acceptable and we can consider the PUDV to be a reliable tool.

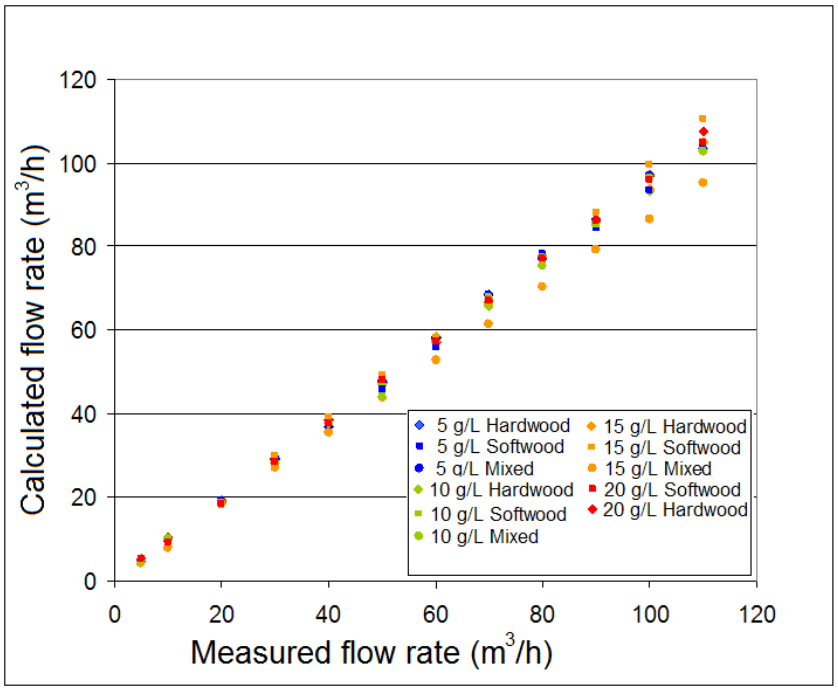

Figure 2.10: Comparison between the measured and calculated flow rate

For every tested pulp, the velocity profiles were determined at each flow rate. In figure 2.11 we show the velocity profiles at different consistencies for the Hardwood pulp. In the graphs, the "y" axis represents the distance (expressed in millimetres) to the wall of the pipe. In order to guarantee the quality of our measurements, all the velocity measurements were done until we reached the centreline of the pipe, which is at 40 mm distance from the wall. Similar to the previous section, we show the velocity profiles for the softwood pulp in figure 2.12 and those concerning the mixed pulp in figure 2.13.

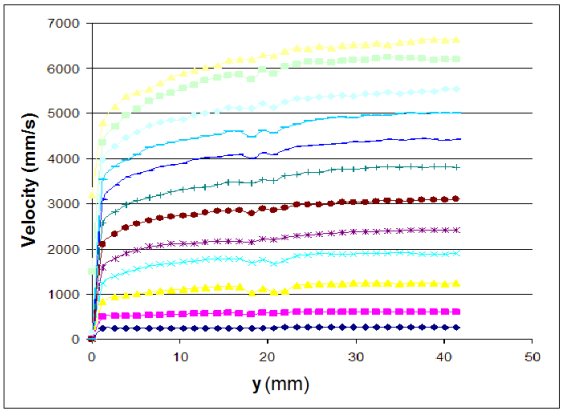

(a) 5 g/L

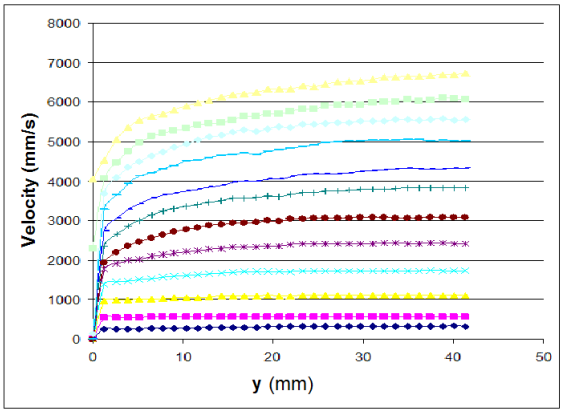

(b) 10 g/L

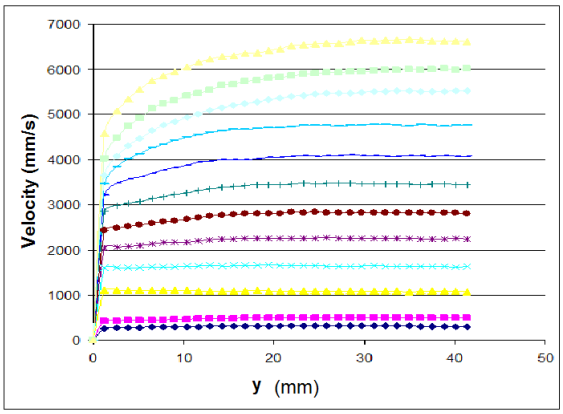

(c) 15 g/L

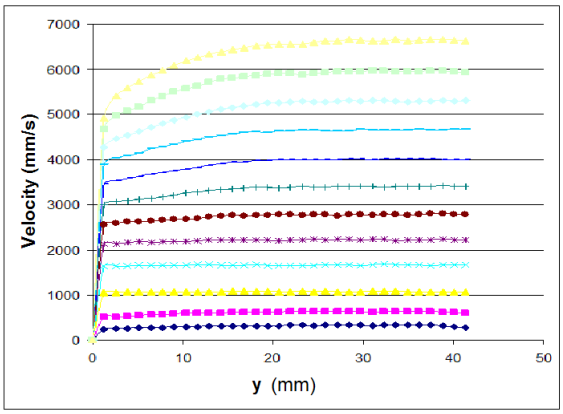

(d) 20 g/L

Figure 2.11: Hardwood pulp velocity profile in an 80 mm in-diameter pipe

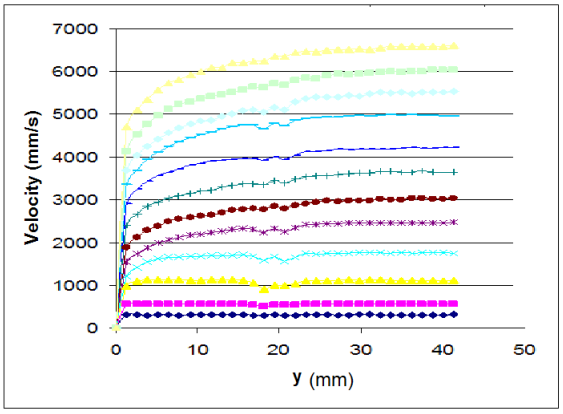

(a) 5 g/L

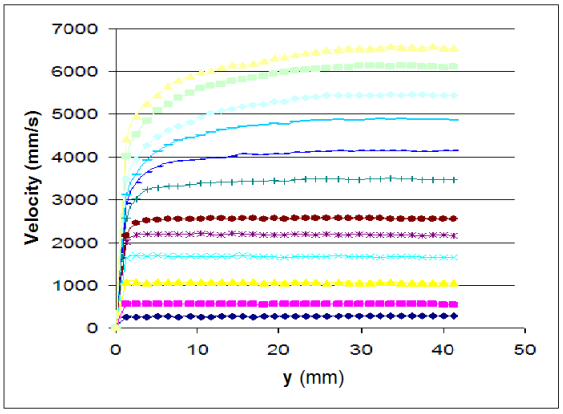

(b) 10 g/L

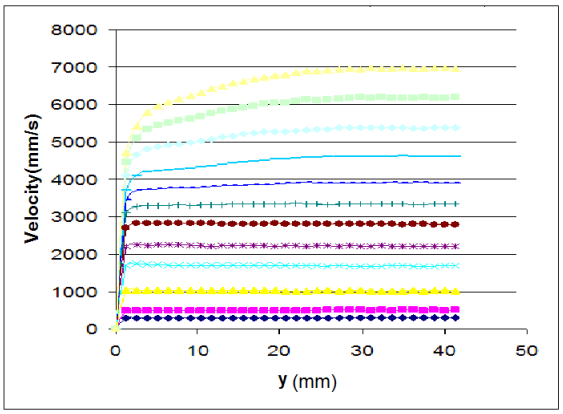

(c) 15 g/L

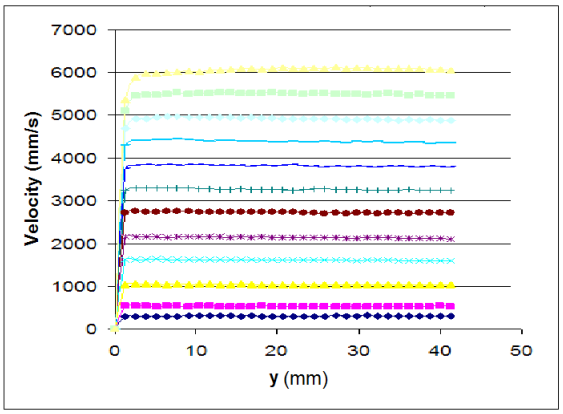

(d) 20 g/L

Figure 2.12: Softwood pulp velocity profile in an 80 mm in-diameter pipe

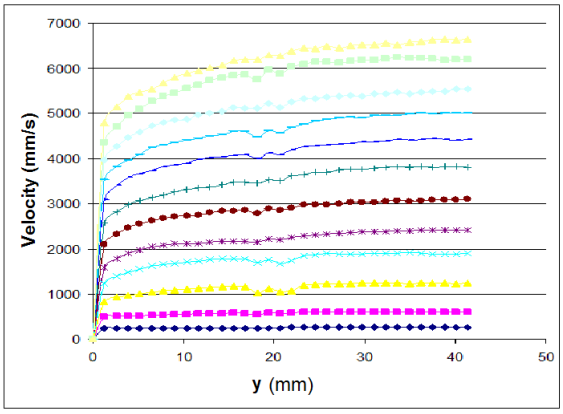

(a) 5 g/L

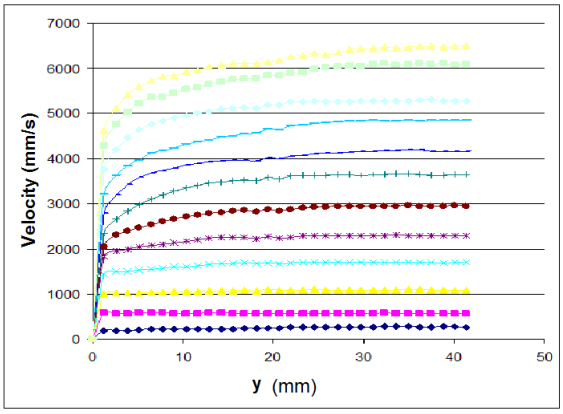

(b) 10 g/L

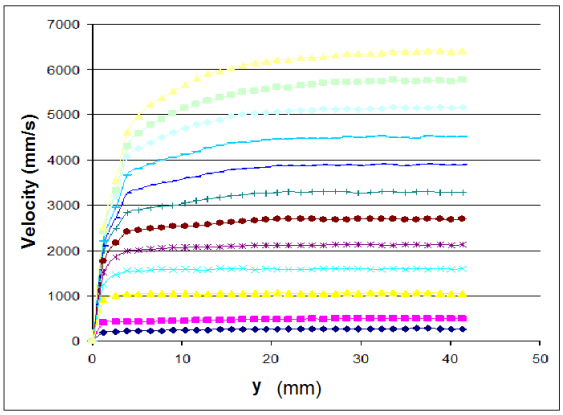

(c) 15 g/L

Figure 2.13: Mixed pulp (softwood and hardwood) velocity profile in an 80 mm in-diameter pipe

As expected, the velocity profiles vary gradually from a plug into a turbulent like profile. These profiles depend on the pulp consistency. We can also see that, even if we have some turbulence near the wall, it is possible to have a plug formation at the centre of the flow. Hence, the plug-annulus theory is verified. We also found that for the 5 g/L pulp we always have a distortion at exactly 20 mm from the wall. This distortion comes from a reception of parasite echoes. We can also compare these results to the first estimation of the flow regimes done with the head loss analysis. It was found that a total turbulent regime comes at much higher flow speeds i.e. flow speed superior to 4 m/s depending on the fibre concentration. So considering the nature of the pulp only, a high shear stress should be continuously applied to guarantee a very mobile pulp that will give us a good formation. These high shear rates could be reached by flow speed or by turbulence. It should also be noticed that total in-line mixing would be very difficult to reach in lower flowing conditions at industrial fibre concentrations.

2.2.2 Study of pulp behaviour in a sudden expansion

To measure the distance needed by a fibrous suspension to recover a stable velocity profile we used the pulsed ultrasonic Doppler velocimeter in a sudden expansion configuration from a 17 mm in-diameter Plexiglas pipe to a 42 mm in-diameter pipe. To this effect, we used another circuit attached to the first one described previously (red circuit in figure 2.14).

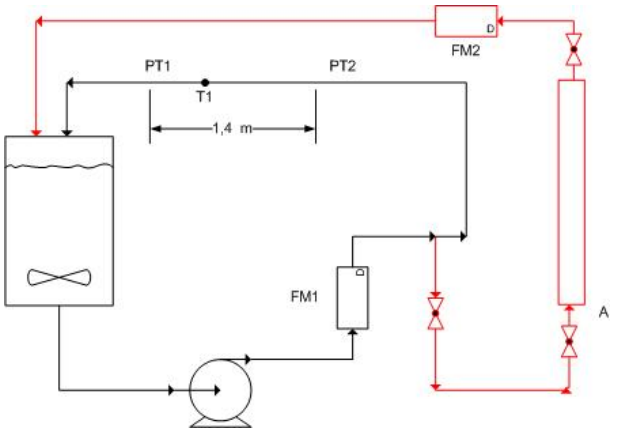

Figure 2.14: The second circuit of the hydrodynamic test bench

The protocol chosen was to place the PUDV sensor in different locations from the point zero corresponding to the sudden expansion step until a stable velocity profile was attained and measure this distance for every pulp at different flow rates. This protocol is depicted in figure 2.15.

We considered that a stable velocity profile was attained when, at three consecutive locations, the variation between the velocity profiles was less than 5%.

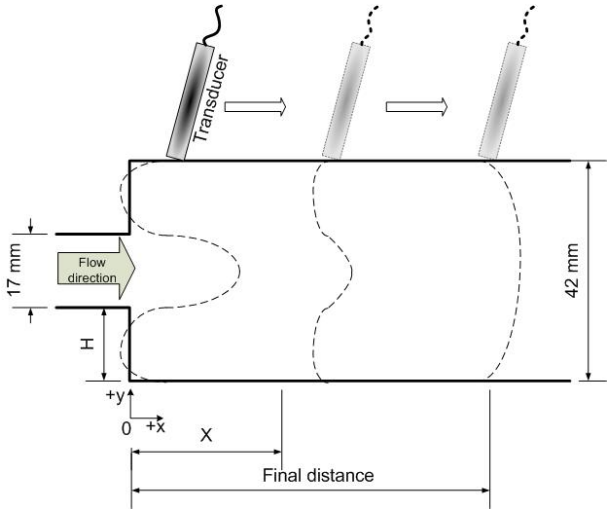

Figure 2.15: Protocol for recirculation length determination

Typical results are displayed in figure 2.16 and figure 2.17, respectively for the softwood and the hardwood pulps. For the softwood pulp, it was found that consistency plays a minor role on the recirculation length at small flow rates (flow speed inferior to 0.6 m/s) whereas a strong sensitivity to fibre concentration was observed for the hardwood pulp in the same conditions. This could be explained by the high mobility of fibres in hardwood pulps while softwood fibres trend to bloc themselves.

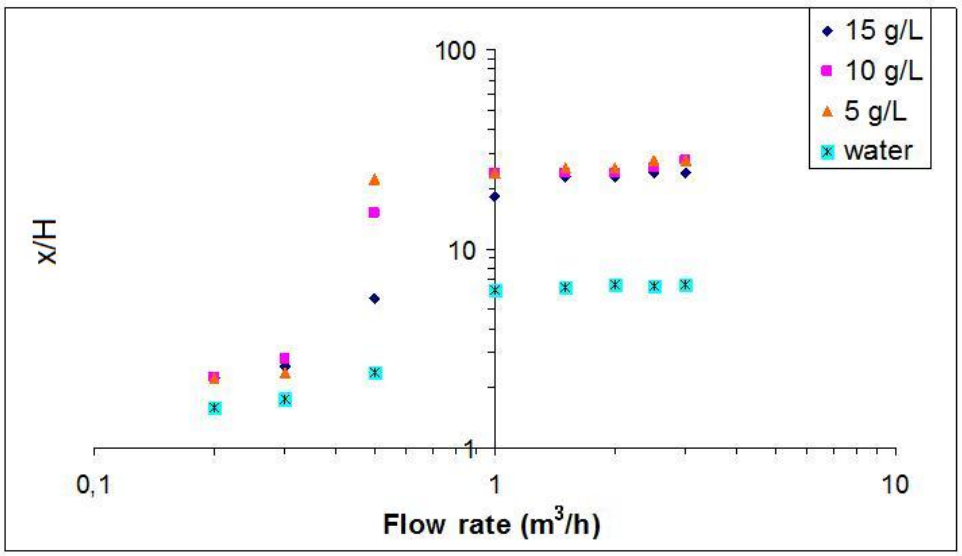

Figure 2.16: Recirculation length in a sudden expansion for the softwood pulp at three different consistencies and for water

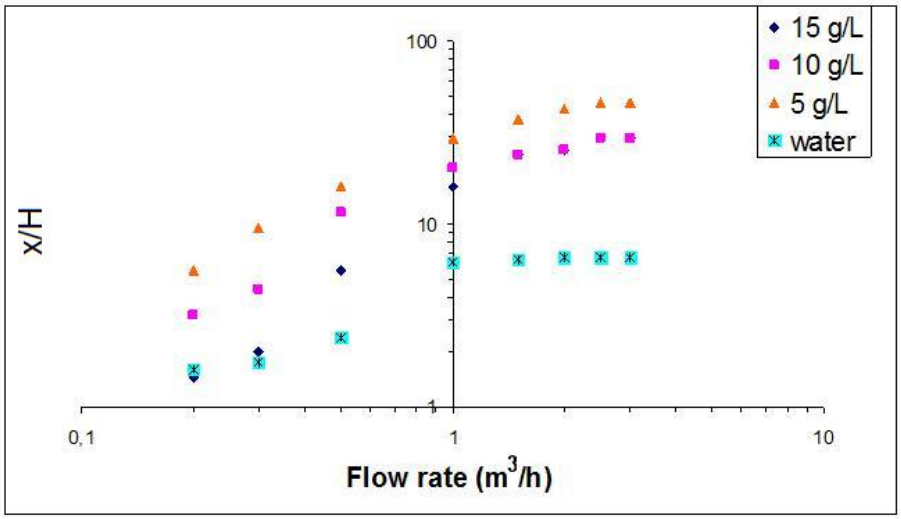

Figure 2.17: Recirculation length in a sudden expansion for the hardwood pulp at three different consistencies and for water

Thus, the value of the recirculation length may depend on the concentration for a given flow rate. At higher flow rates (flow speed superior to 1 m/s), the concentration plays a minor role and a stabilisation of the recirculation length is obtained. As observed in these results the recirculation length is around the double of the recirculation length obtained with pure water. This is explained by the presence of fibres that restrains the turbulent energy cascade. So a longer distance is needed to recover an equilibrium level.

2.2.3 Application to a stabilisation chamber

Generally the distribution of the pulp into this chamber is made through flexible pipes with a diameter inferior to the size of the chamber. From a practical point of view this is quite logical, but this configuration generates big vortices that will disturb the flow. The design of the stabilisation chamber should avoid transverse effects. The length of the stabilisation chamber should be long enough to guarantee the recover of a stable velocity profile. The flow speed inside this chamber should be strong enough to ensure good fibre mobility and good mixing if a local dilution system is used. To study all these parameters a computational fluid dynamics simulation was made of the functioning of a standard stabilisation chamber.

Transversal effects

The internal architecture of the stabilisation chamber is an important issue. The local dilution control made at the flow spreader is not efficient if the flow can be mixed in a cross direction inside this chamber. We have previously shown that complete mixing is quite

difficult in some conditions. However if there is a differential pressure between the inlet pipes, then cross-direction flows are created, generating an oscillating mixing phenomena that makes almost impossible to get an accurate fibre mass distribution control. There are two solutions to this problem. The first one is to put some grids with different hole sizes in order to generate a local blending of the inlet flows. This will attenuate the differential pressures. However this solution does not prevent from a total control of cross-direction mixing. The other solution is adding a division wall between two incoming pipes. These division walls are not as long as the chamber itself: a small mixing chamber is left just before the entrance of the turbulent generator to dampen pressure variations but keep the cross-directional mixing as small as possible.

Computational fluid dynamics simulations

Considering the low consistency used in a normal headbox and the flow rate passing through, it can be said that a plain water flow is similar enough to the fibrous suspension for studying some specific phenomena. Moreover, the use of water is the most penalizing case because of higher viscosity compared to pulps at normal flow velocities. It is possible then to make a computational fluid dynamics simulation of this chamber. A standard $k-\epsilon$ turbulent model was used to simulate a 3D stabilisation chamber. A standard stabilisation chamber with internal divisions was chosen for this part of this work. One of the divisions, in this case the division closer to the external wall, was made a little bigger in order to analyse the influence of the symmetry of the positioning of the internal walls.

The first thing we can see in the CFD results is that the velocity contours are almost stabilised before getting to the tube tank (see figure 2.18(b)). We can also see that there is no symmetry of the flow, which confirms that dead zones are created at this inlet. The pressure contours are quite logical and corresponds exactly to what we expected and measured in the headbox pilot (see figure 2.18(a)). However, we expected to have equal size dead zones in a vertical plane but instead we can see that there is an unstable process that continuously changes the eddies in every direction. This phenomenon could be related to the Coanda effect which is the tendency of a stream of fluid to stay attached to a surface rather than follow a straight line in its original direction.

In order to verify this, a streamline analysis was made and the results shown in figure 2.19. It can be seen that the size and shape of the big eddies depend not only on the inlet flow speed but also on the size of the chamber itself. This is why in figure 2.19(a), which is related to the modified compartment described before, there are bigger eddies than in the others compartments as shown in figure 2.19(b). We could see that these eddies depend on time and evolve continuously in different directions. Nevertheless, this

streamline analysis should be taken with caution, because as it was shown previously the recirculation length for pulps certainly differs with that for water. However we can think that the global behaviour would be the same.

If we consider the pressure contours (figure2.20(a)) we can notice that there is nearly no headloss in this section of the headbox which is what we expected.

It is also interesting to analyse turbulence. As it was pointed out previously a certain turbulence intensity and length scale is needed to break up flocs. Remember that turbulence intensity is defined as the relationship between the root-mean-square of the turbulent velocity fluctuations (eddies) and the Reynolds averaged mean velocity of the flow, while the turbulent length scale is a physical quantity describing the size of the large energy containing eddies in a turbulent flow.

In figure 2.21(a) it can be seen that the highest turbulent intensity can be found at the inlet of the stabilisation chamber, which is quite logical considering the mean flow speed at this location and the big eddies structures formed there. On the other hand the turbulence length contours (figure 2.21(b)) show a very interesting result. For a pure fluid as water the turbulent length passes from 2 cm at the inlet to almost 7 cm at the core of the compartment. This would support our idea that big flocs structures should be found at this location. It would be very interesting to do the same study using another fluid similar to a fibrous suspension, i.e. a non-homogeneous fluid, but this is out of the scope of this project. However, remembering the length needed for recovering a stable velocity profile, showing us that the fibrous suspension keeps some of the energy applied in turbulence inside its bulk structure. We can hypothesize that for a fluid like a fibrous suspension bigger turbulence length will be found at this place. Then, bigger flocs structures should be found at the core of a stabilisation chamber.

We also made an analysis of a horizontal plane cutting several compartments. As it was shown before, there is a dimensioning problem at the near wall compartment and therefore there is a reduction of speed in the near wall region and a bigger vortex is formed at the inlet. This is why we find at this region a high turbulent intensity (see figure 2.22(a)) that could be avoided by correcting this compartment dimensions. For the same reason, there is a bigger turbulent length at the first compartment (see figure 2.22(b)).

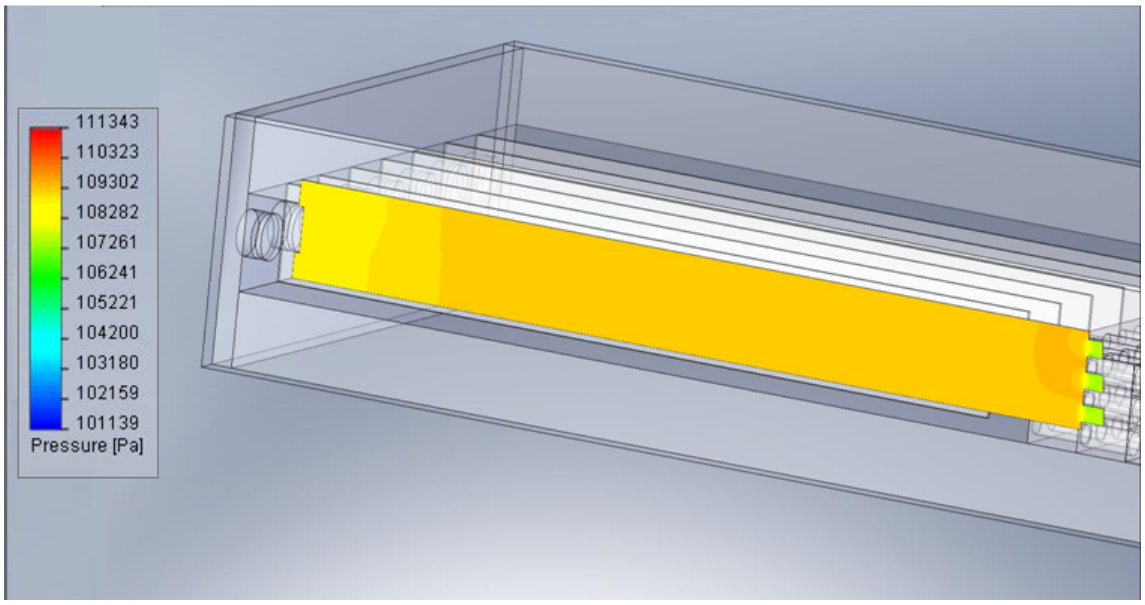

(a) Pressure contours

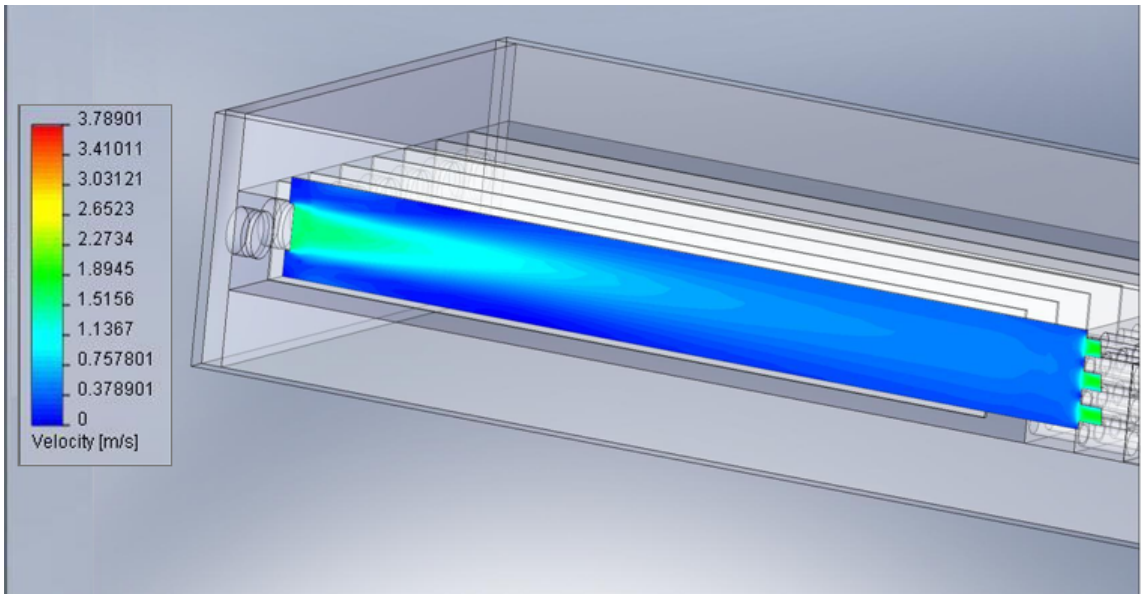

(b) Velocity contours

Figure 2.18: Pressure and velocity contours for a compartment of the stabilisation chamber

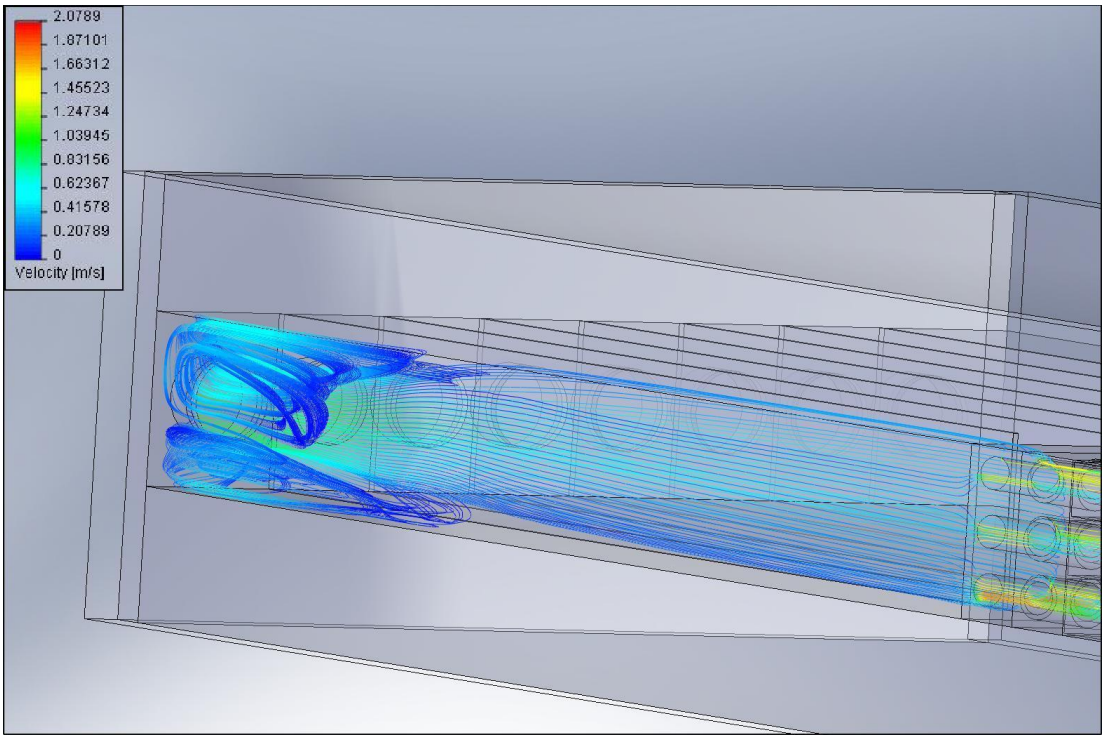

(a) External wall compartment

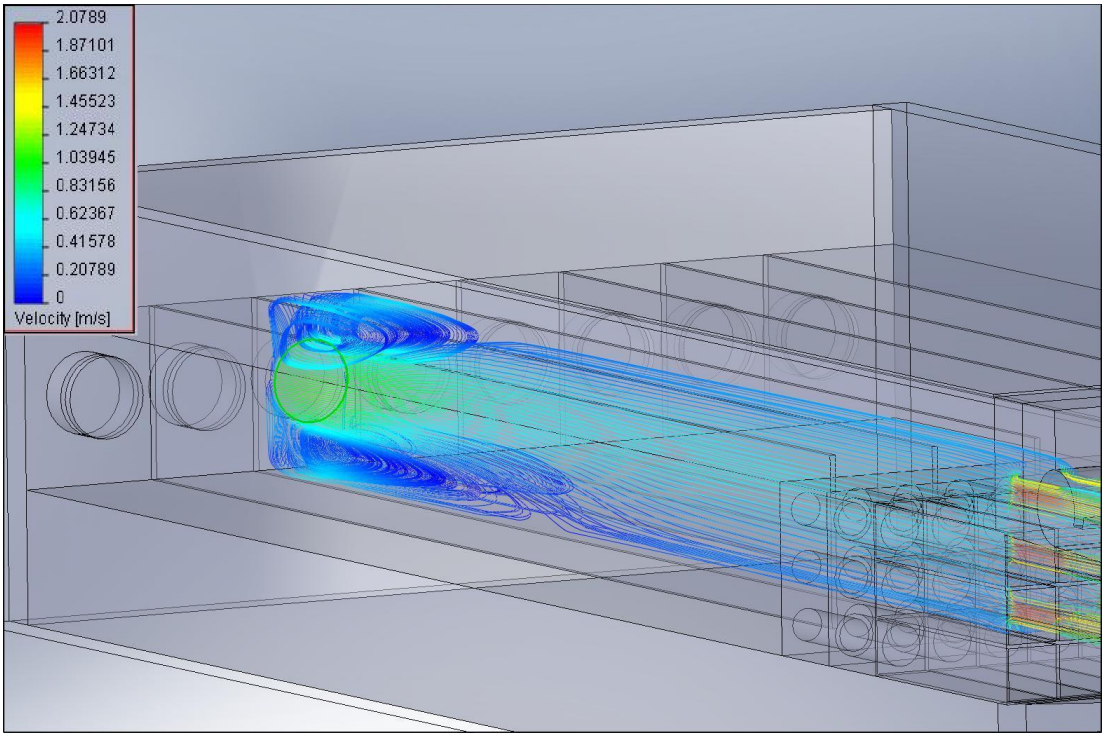

(b) Centre compartment

Figure 2.19: Streamline analysis of the stabilisation chamber inlet

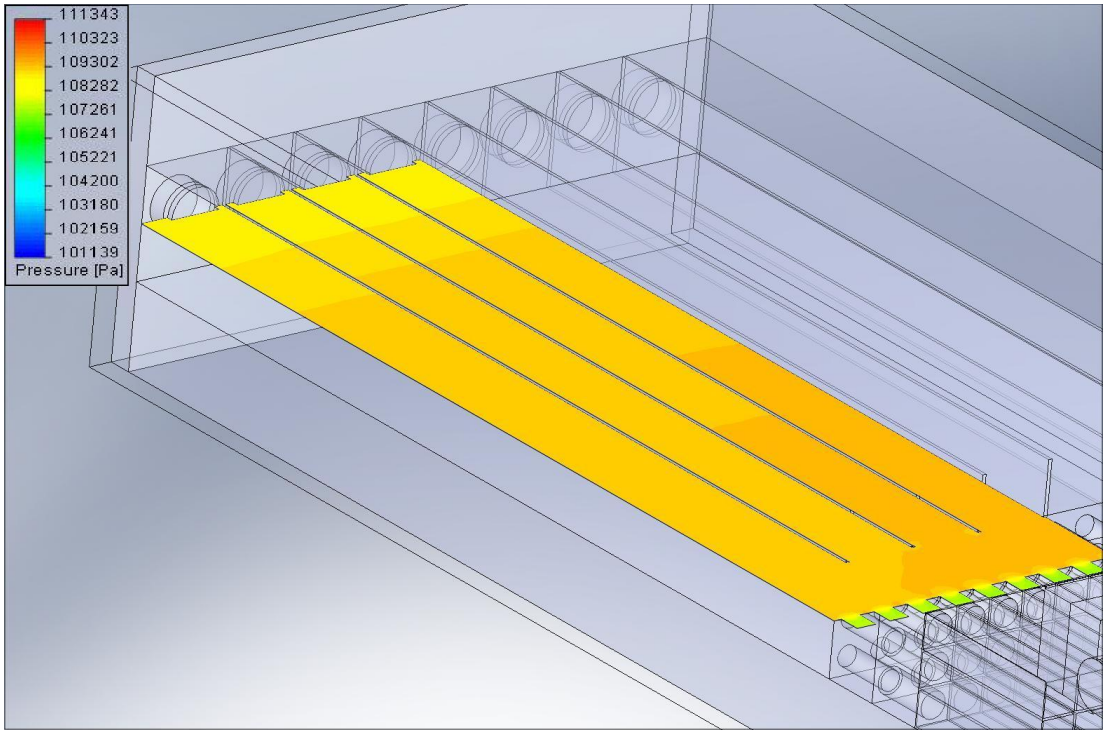

(a) Pressure contours

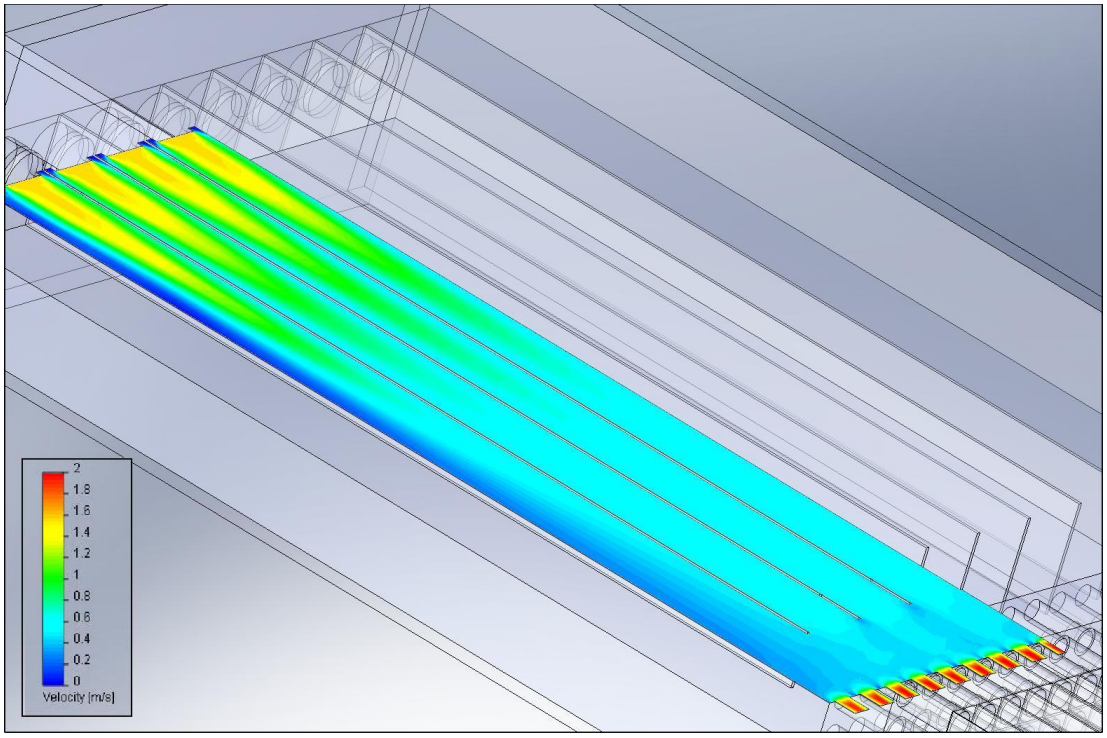

(b) Velocity contours

Figure 2.20: Pressure and velocity contours in a horizontal plane of the stabilisation chamber

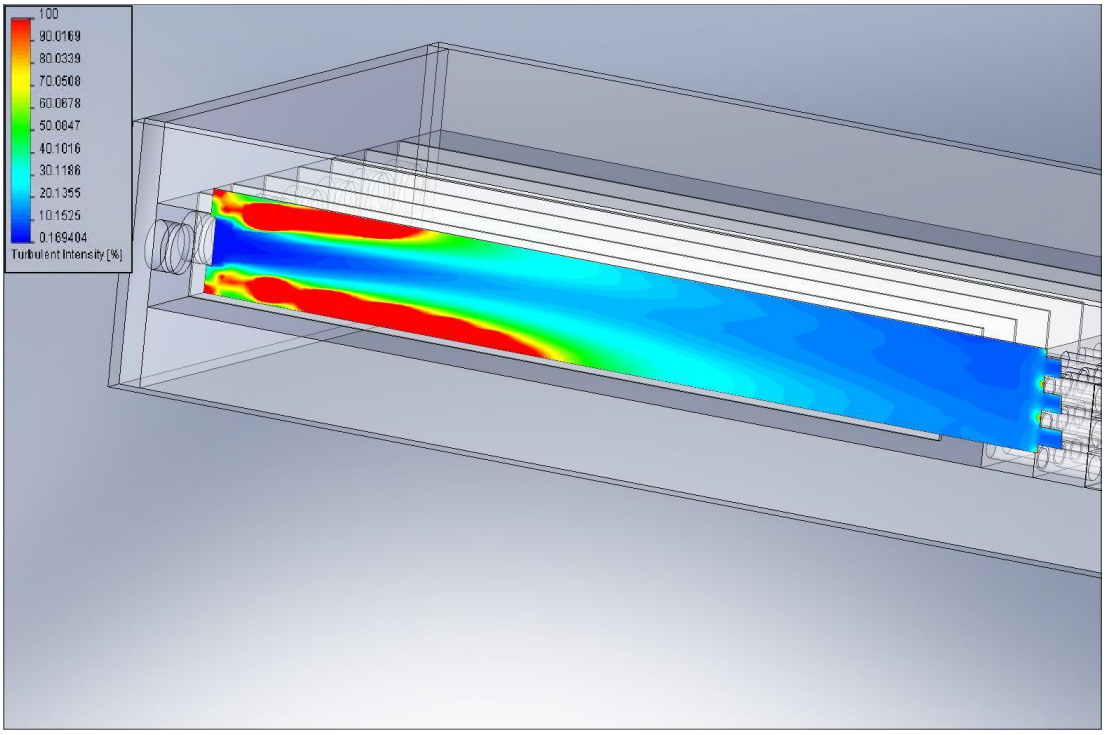

(a) Turbulent intensity contours

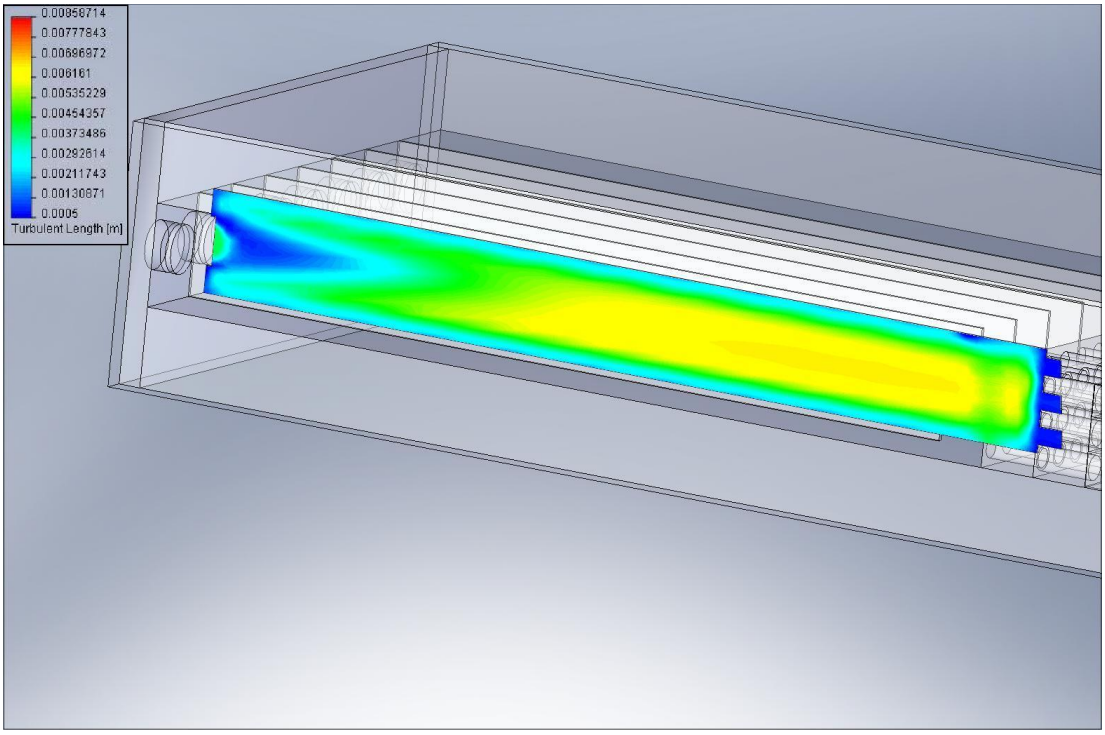

(b) Turbulent length contours

Figure 2.21: Turbulence analysis of the stabilisation chamber

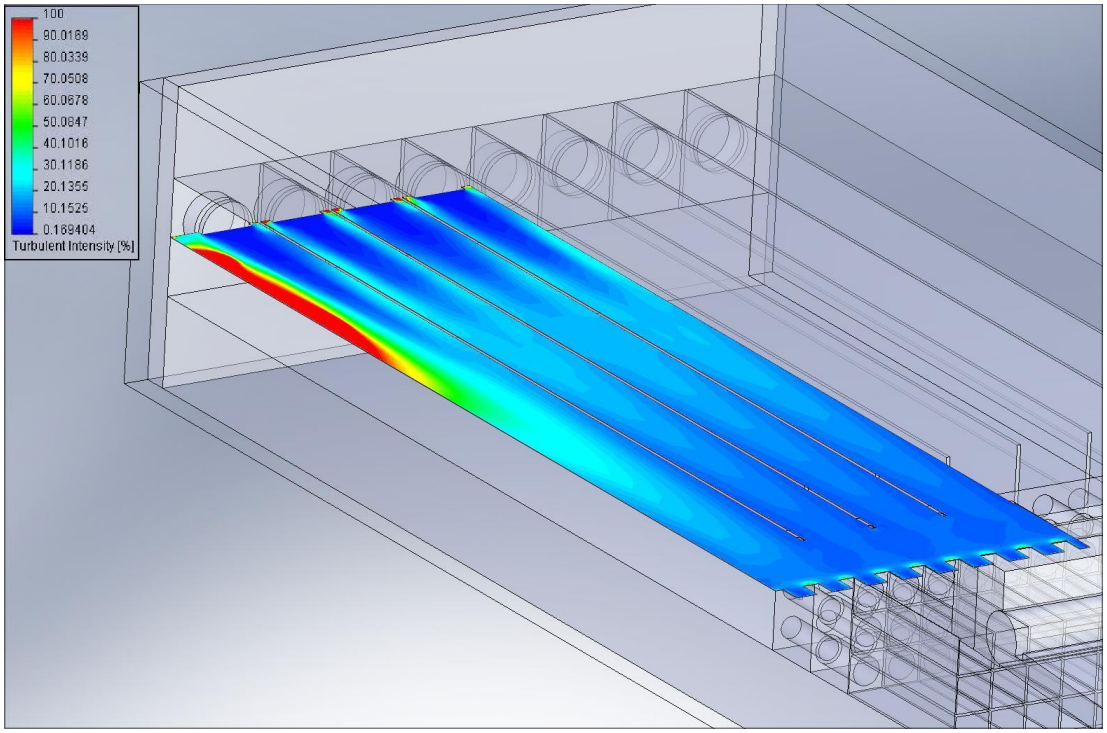

(a) Turbulent intensity contours

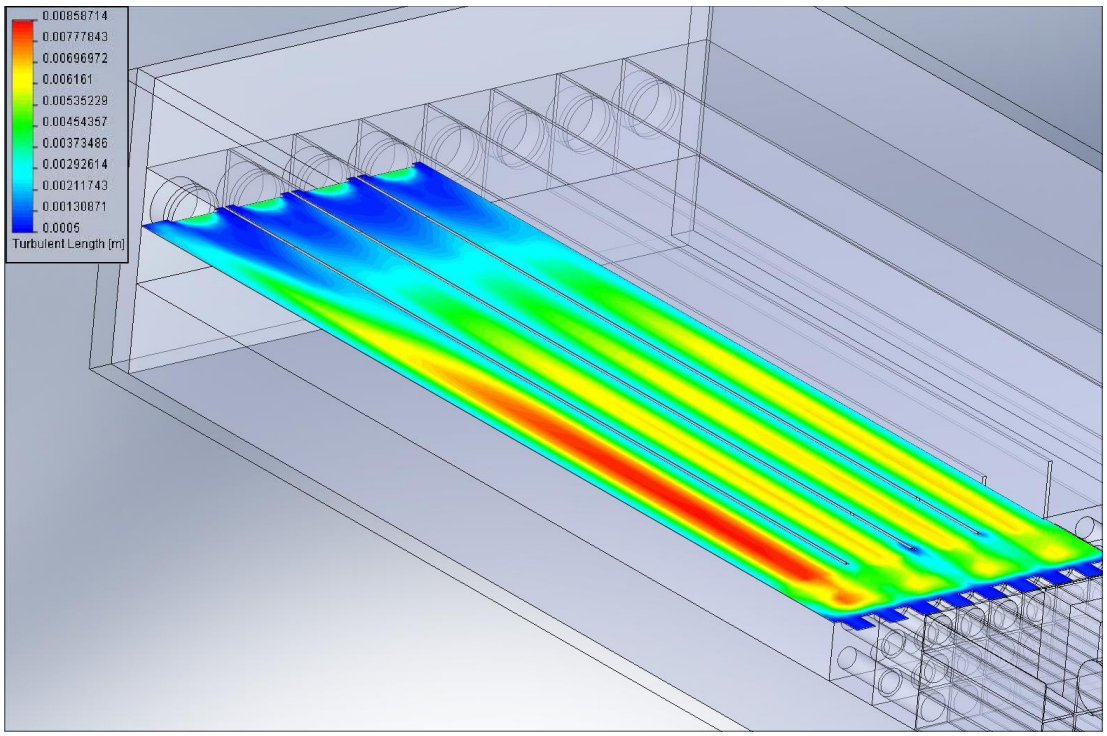

(b) Turbulent length contours

Figure 2.22: Turbulence analysis contours in a horizontal plane of the stabilisation chamber

Conclusion of the stabilisation chamber study

From a hydrodynamics point of view, a developed flow is obtained at the end of this stabilisation chamber. Other geometrical cases will be analysed further on in this work. If this chamber is used as a mixing chamber i.e. when a local dilution system is used, then its utility is justified. However, if there is no mixing, then we could think that a shorter stabilisation chamber could be used. The behaviour of the pulp in this kind of geometry could be globally predicted from the studies made previously. Considering the weak concentration in fibres inside a headbox, the pulp behaviour will be somewhat very similar to the results obtained with the computational fluid dynamics simulation. A fibrous suspension model would be of great utility for a CFD simulation of a headbox, however nowadays there is no model available and to develop this model is extremely complicate and out of the scope of this present work.

2.3 Study of the turbulence generator

As explained previously, the turbulent generator in modern headboxes is most of the times composed by a tube bank. High intensity turbulence is generated and then the flow is equally distributed into the nozzle. The main objective of this device is to apply a certain amount of turbulent energy at a certain turbulent scale to the fibrous suspension to break most of the flocs and to get the most homogeneous pulp possible. From our visual observations, the pulp flocculation level before and after the tube bank is not significantly different. So, a paramount question has to been answered: is the energy disposed in this device properly used? To study this, two different approaches were taken into account. The first one was to characterise in terms of pressure drop and turbulence intensity the amount of energy applied in this setup and to determine if there is any difference (hydraulically and energetically speaking) between water and a fibrous suspension for this characterisation. Then, the second approach consisted in making a qualitative study of the flocculation level of the pulps and trying to determine a possible efficiency of the energy applied into this setup. Two different theoretical deflocculation processes were described and studied, and a critical analysis of the available measuring methods for determine the size of a floc was also made.

2.3.1 Study of pulp behaviour in a thick hydraulic orifice plate

In order to better understand each parameter inside a tube bank, a laboratory scale setup, consisting in an exchangeable thick hydraulic orifice plate was made. Several geometrical parameters were tested.

Setup description

The laboratory scale setup consisted in a rectangular Plexiglas box that holds a perforated plate (see figure 2.23). This perforated plate, which plays the role of a thick hydraulic orifice plate, can be changed and different geometrical values (length and constriction diameter) were imposed to all the pulps flows. The aim of this setup is to simulate the passage of the pulp inside of a single step tube bank and to study the evolution of flocculated fibrous suspensions passing through a sudden constriction channel. The length of the inlet section is long enough to ensure a perfect velocity profile development. Two pressure taps were included in the rectangular section at the inlet and at the outlet of the orifice plate to measure the head loss caused by this orifice plate. This setup was connected to the hydrodynamic test bench as shown in figure 2.24. The pulps used in this section are described in table 2.2. We have decided to use a mixed pulp because it is commonly used in industrial conditions. Two different concentrations were tested, a diluted one (5 g/L) and a concentrated one (10 g/L). The choice of these concentrations is related to the usual consistencies in a headbox. The flow speed range varies from 0 to 0.13 m/s in the rectangular section and 0 to 5 m/s inside the orifice itself. The different orifice plates studied are described in table 2.3.

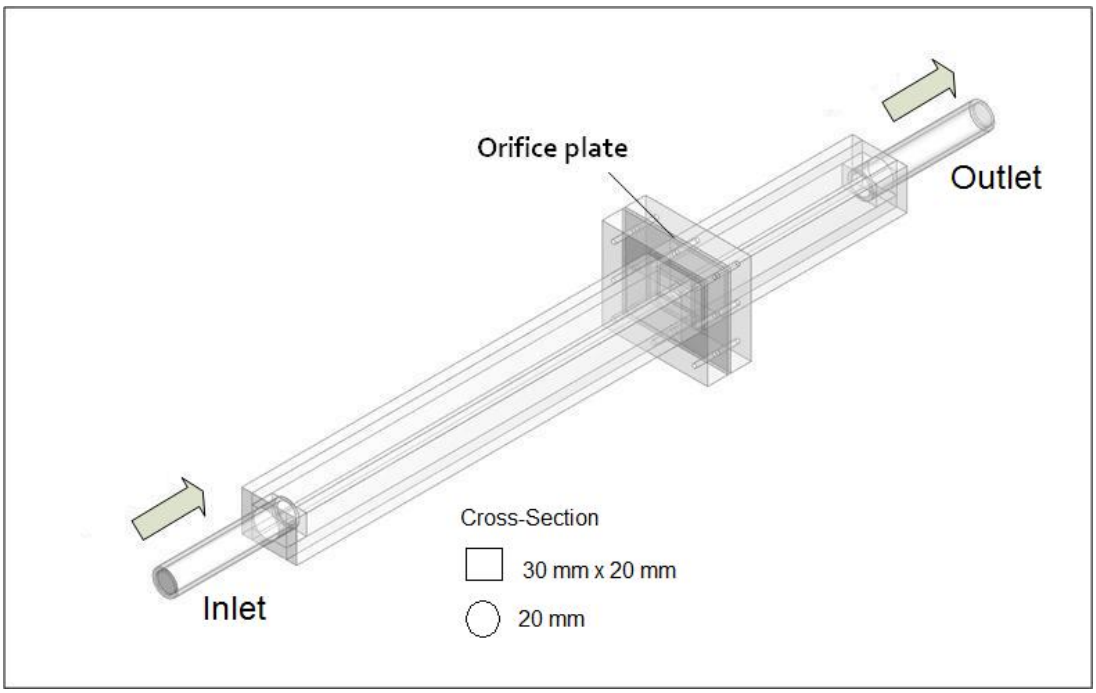

Figure 2.23: Orifice plate setup

Type of pulp	Mean fibre length, mm	Coarseness, mg/m	Conc., g/L	°C	°SR
Mixed pulp (60%HW/40%SW)	1.32	0.10	5, 10	25	45

Table 2.2: Properties of the fibre suspensions used in the orifice plate study and some operating conditions

Orifice diameter, mm	Length, mm
5, 10, 15	3, 9.5, 25, 50, 99

Table 2.3: Geometrical characteristics of studied orifice plates

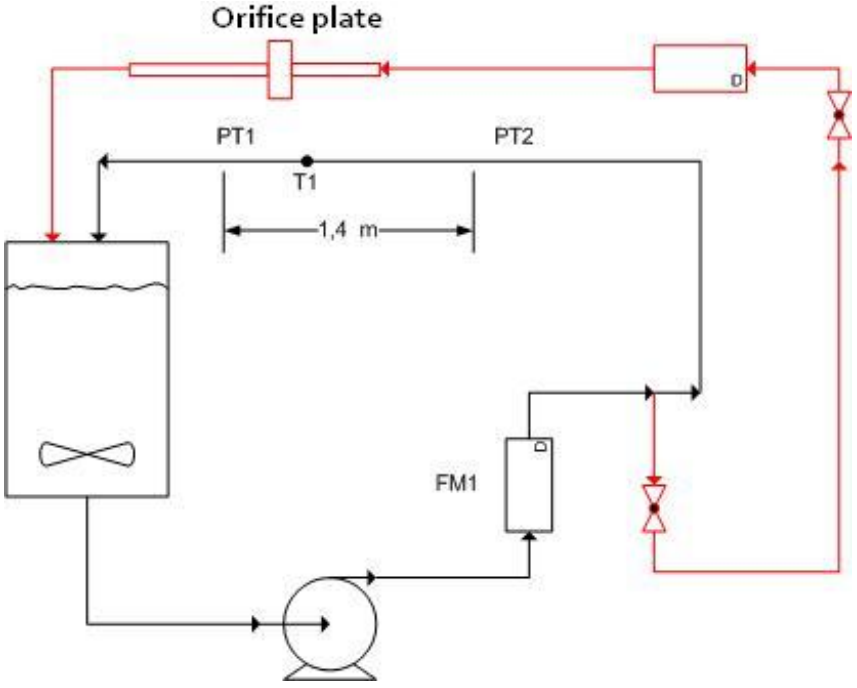

Figure 2.24: Setup connection to hydrodynamic test bench

Theoretical characterisation of a thick orifice plate

A good characterisation of this orifice plate is essential for the study wanted. A theoretical approach is suitable in this case. For this, we computed the theoretical head loss by means of an empirical formula (equations 2.6 and 2.7) proposed by Idel'cik [52] and then compared these results to the measurements made using water. Because of the complexity of the last equations, we have decided to keep the nomenclature proposed by Idel'cik.

For $Re > 10^5$:

$$\begin{aligned} \zeta &= \frac{\Delta H}{\gamma U_1^2/2g} \\ &\cong \left[\left(0,5+\tau\sqrt{1-\frac{F_0}{F_1}}\right)\left(1-\frac{F_0}{F_1}\right)+\left(1-\frac{F_0}{F_1}\right)^2+\lambda\frac{1}{D_H}\right]\left(\frac{F_1}{F_0}\right)^2 \\ &= \left(\zeta_0+\lambda\frac{1}{D_H}\right)\left(\frac{F_1}{F_0}\right)^2 \end{aligned} \tag{2.6}$$

For $Re < 10^5$

$$\zeta = \frac{\Delta H}{\gamma U_1^2/2g} \cong \left(\zeta_\varphi + \varepsilon_0^{-\mathrm{Re}}\zeta_0 + \lambda\frac{1}{D_H}\right)\left(\frac{F_1}{F_0}\right)^2 \tag{2.7}$$

where:

- ζ is the hydraulic headloss coefficient.
- γ is the specific gravity of the fluid flowing inside.
- F is the section of passage
- D_H is the hydraulic diameter of the orifice plate
- ζ_0 is the headloss coefficient as a function of the Reynolds number and the ratio of passage sections
- τ, ζ_φ and ϵ_0^{-Re} are determined from tables and charts.
- λ is the head loss coefficient for the liquid flowing in the orifice plate

The results are shown in figure 2.25. It can be seen that the formula proposed fits very well with the experimental measurements and the water curves can be used as the reference curve to compare the results obtained with the different pulps.

Study of the behaviour with pulps

The results obtained with pulp are shown in figure 2.26. The consistency of the pulp has no influence on the head loss. This is a very interesting result because it could be said that from an energetical point of view, any turbulence generator could be designed

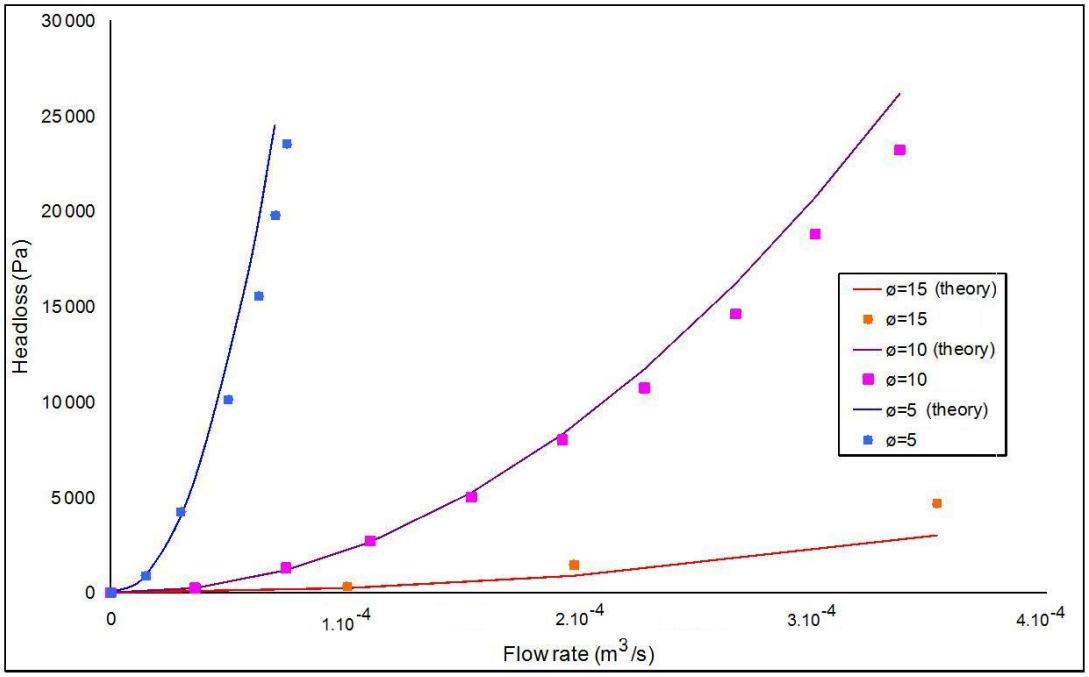

Figure 2.25: Headloss in orifice plates - Water curves compared to theoretical values

using a simple water analogy. Tmeggshe influence of the geometry of the orifice plate was also studied. The pressure drop is related to the diameter reduction of the constriction channel, but is the relationship between the constriction length and the pressure drop is less clear. These two last parameters were changed as described in table 2.3.

We studied constriction length varying from 3 mm to 99 mm and diameters varying from 5 to 15 mm. The results of the length variation are shown in figure 2.27. We can see that the highest pressure drops are for the 3 mm length orifice plate. For the other lengths, the same order magnitude is obtained whatever the length. However, using the empirical formulae derived by Idelc'ick, it can be demonstrated that there is a minimum for the pressure drop, which is obtained for 25 mm length with 10 or 15 mm in-diameter orifice plates. This can be explained by the fact that after a certain length, the velocity profile inside the constriction is reformed so the head loss can be calculated as a collection of head losses for a sudden constriction, a straight pipe and a sudden expansion device. This decomposition in three smaller parts is essential for understanding that, whatever the length used, the pressure found for these setups are nearly the same (considering the straight pipe pressure drop small enough to be neglected).

If we study now the orifice plate diameter variation, it can be predicted at least for water that the smaller the diameter the higher the pressure drop. This is exactly what we found out (see figure 2.28). It should be pointed out, once again, that the pulp results fit exactly to the water curves.

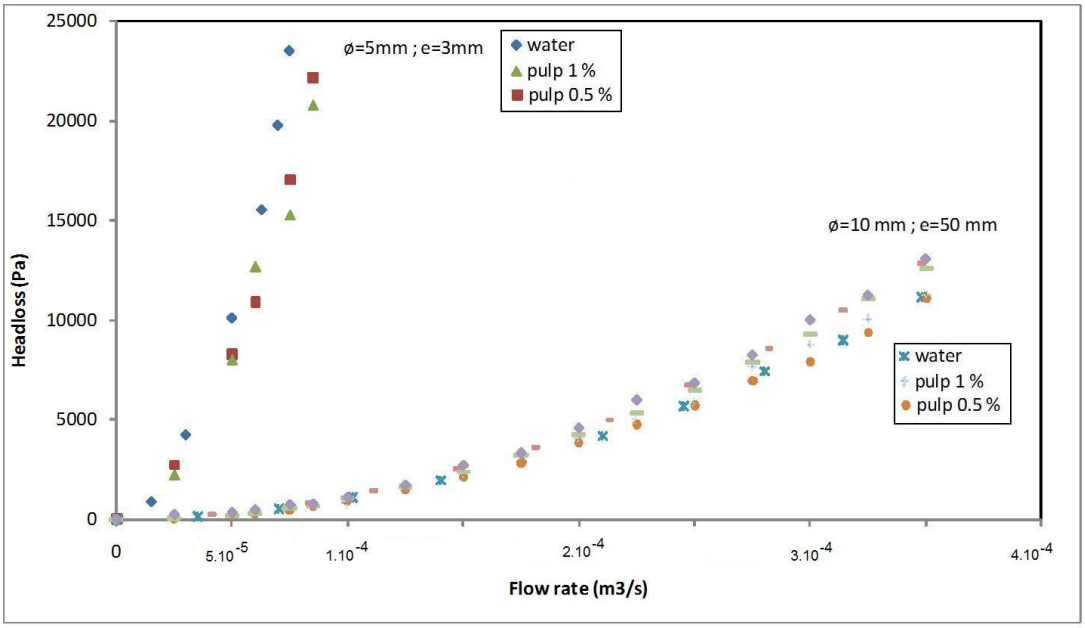

Figure 2.26: Study of the influence of pulp consistency on the headloss in the orifice plates

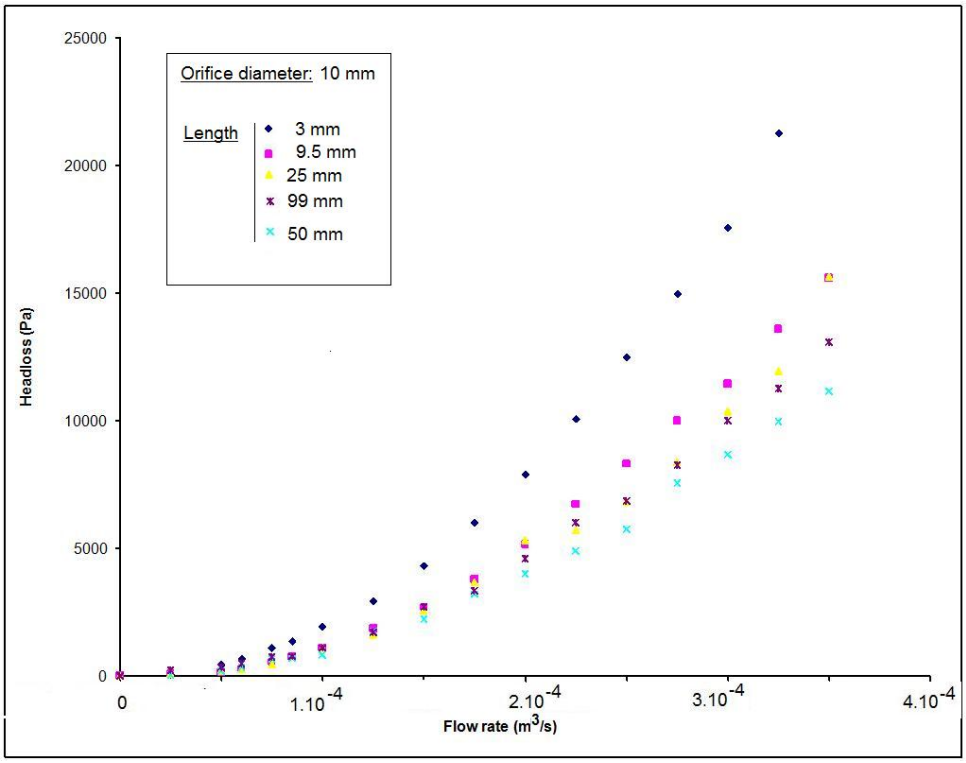

Figure 2.27: Study of the influence of the thick orifice plate length on the head loss

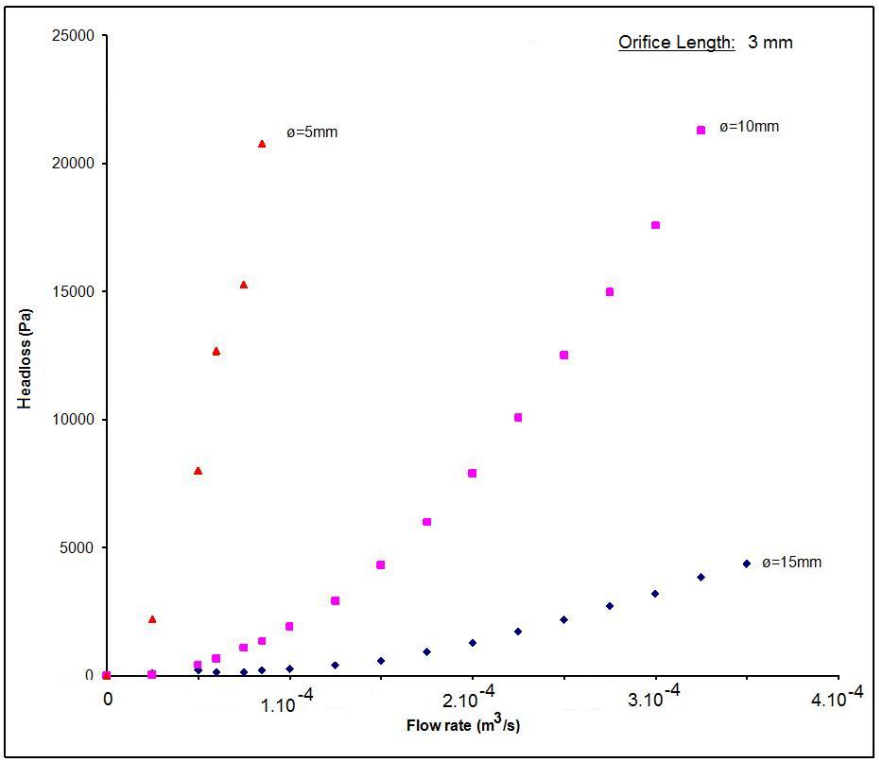

Figure 2.28: Study of the effect of the orifice plate diameter on the head loss

Computational fluid dynamics simulations

Considering that the pressure measurements made with water and with the different fibrous suspensions match quite well together, we can hypothesize that a computational fluid dynamics analysis could be made using only pure water as the flowing fluid. This is true for the macro-scale behaviour at a standard headbox consistency. However we must be aware that at a smaller scale (floc size) this approach is not possible and another modelling method should be employed. A standard $k - \epsilon$ turbulence model was used.

Now, considering the turbulence study, it can be seen that when the length of the orifice plate was modified, there was little variations of turbulence dissipation, intensity and length (see figures 2.29, 2.30 and 2.31). This can be explained by the fact that the velocity profile has enough time to be reformed in these thick orifice plates. So, whatever the length of the small pipe in between (in the limits of reasonable values), the turbulence dissipation and length are very close for the studied cases.

The main parameter for changing the amount of energy dissipated in this setup is the variation of the orifice diameter. For this study, we have chosen a 3 mm long orifice plate and then changed its diameter. We can see in figure 2.32 that the turbulence dissipation remarkably changes from the 15 mm in-diameter orifice to the 5 mm one, passing from 25 W/kg of fluid to a maximum of 850 W/kg of fluid. In other words the turbulent dissipation is multiplied by a factor of 34 when the diameter is reduced three times. It is

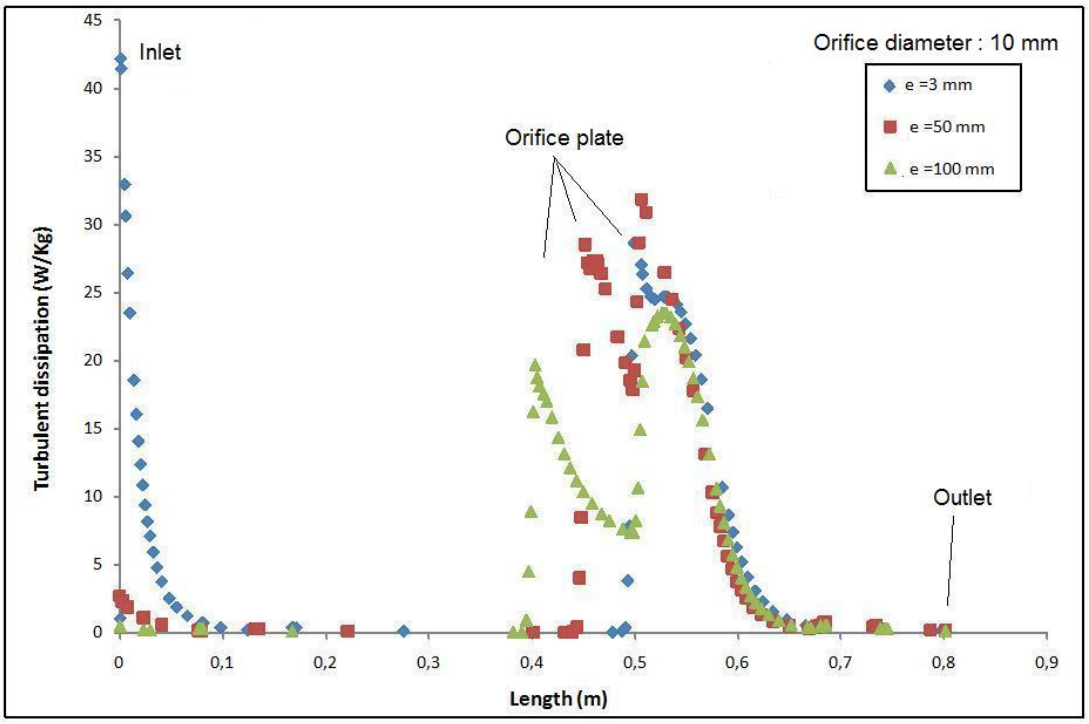

Figure 2.29: Turbulent dissipation for different orifice plates with different lengths

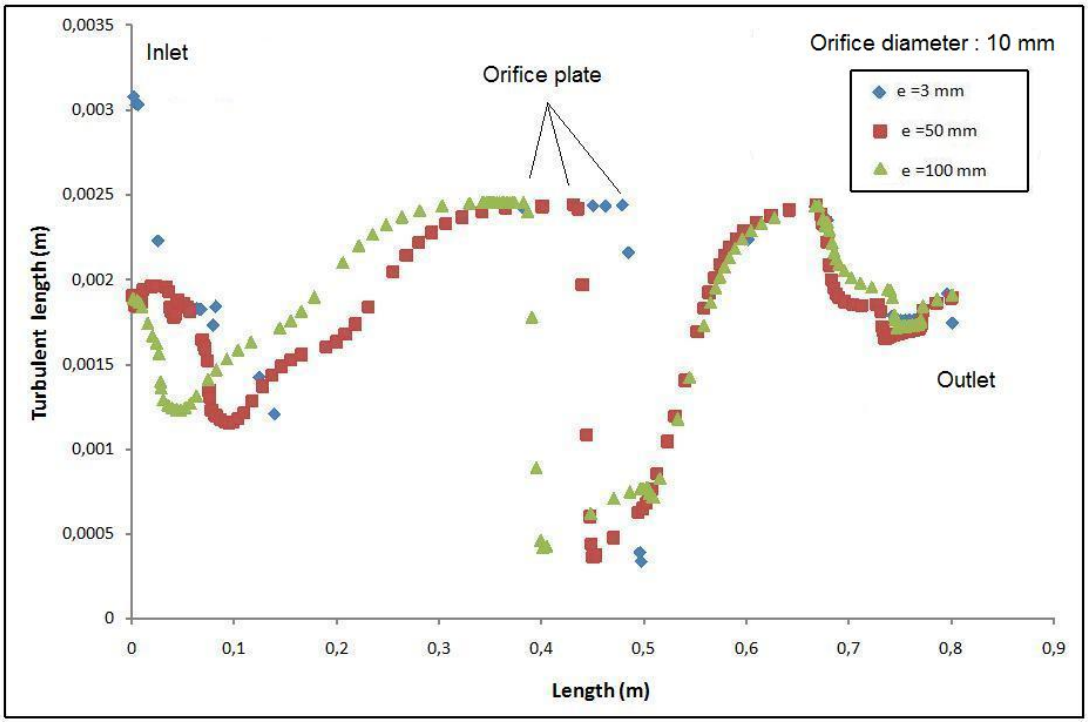

Figure 2.30: Turbulence length for different orifice plates with different lengths

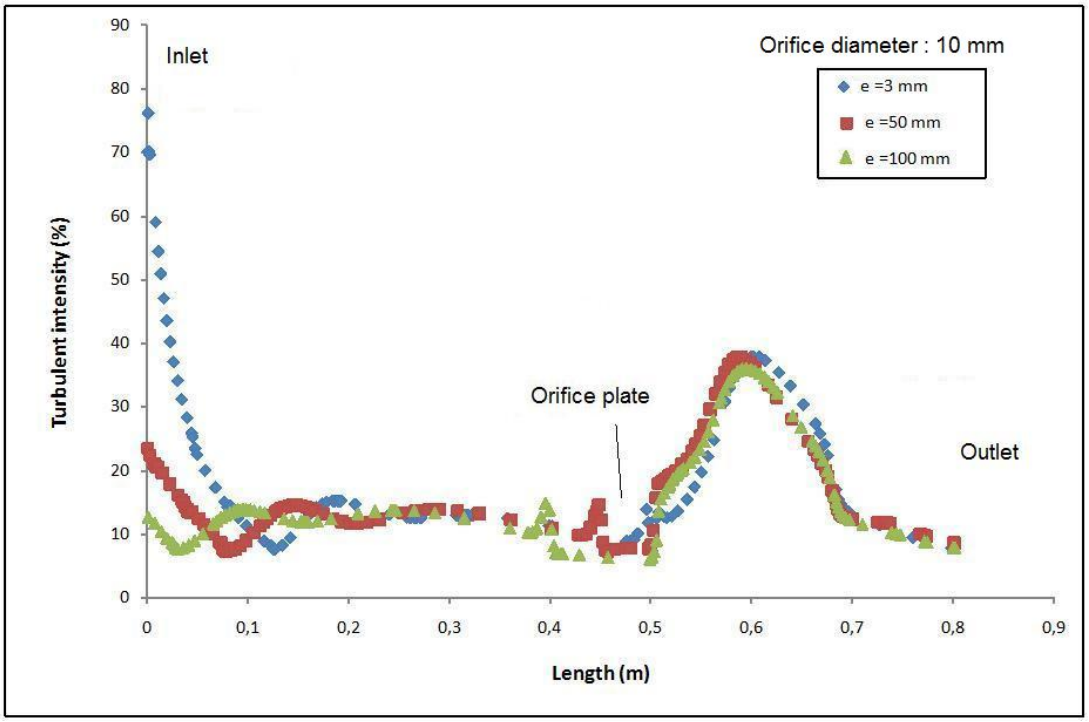

Figure 2.31: Turbulence intensity for different orifice plates with different lengths

quite interesting to see that between the 15 mm and 10 mm diameter cases there is no such a big difference in terms of turbulence dissipation, passing from 25 W/kg of fluid to 50 W/kg of fluid for the second case. The same behaviour was observed for the turbulence length (figure 2.33). However the relative difference between all the cases is much smaller than for the turbulence dissipation. Finally, for the turbulence intensity (figure 2.34 there is a clear difference between the 5 mm in-diameter orifice and the others.

It is interesting to analyse, now, what is the effect of this energy on the flocculation state of the fibrous suspensions. To this effect, we performed a qualitative study of the fibrous suspensions before and after the passage through the orifice plates. For most of the cases observed, there is no noticeable difference of the floc size before and after the orifice plate. Only for the 5 mm in-diameter, 3 mm thick orifice plate there is a more homogeneous pulp at the end. However, the amount of energy disposed in this configuration is too high to be used in industry (around 1 kW per kilogram of pulp).

Just at the end of the constriction a homogeneous pulp is observed but this homogeneity disappears at the end of the big recirculation length. In other words, it could be possible that the passage through the other constrictions produces a certain degree of deflocculation, but the big recirculation eddies turn over the fibres regenerating the flocs that were just broken.

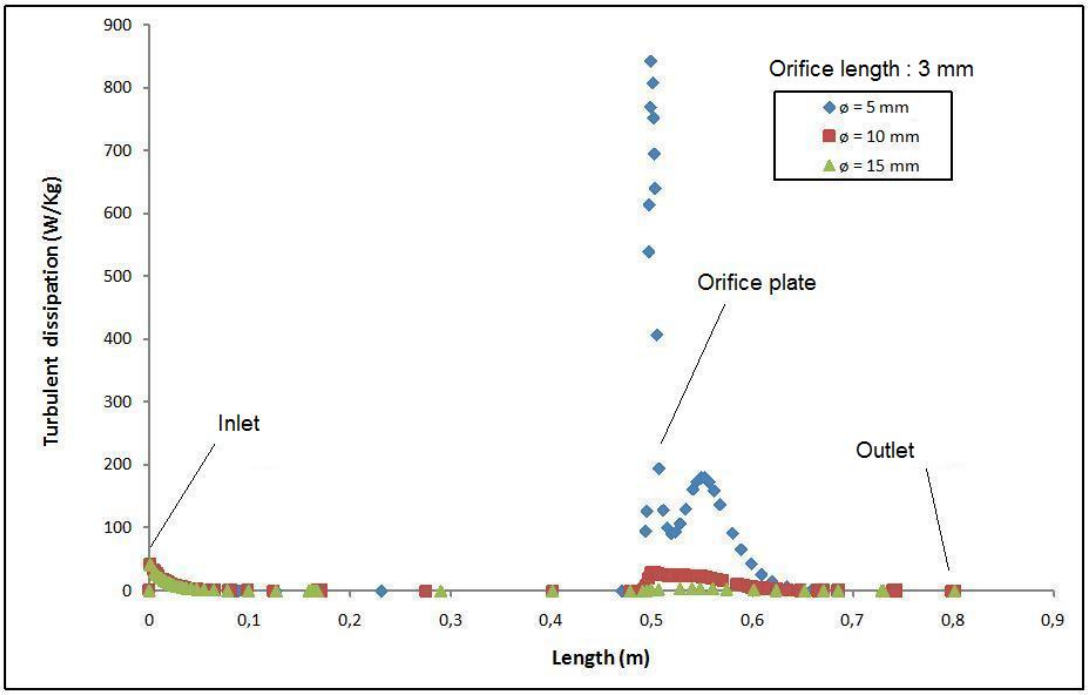

Figure 2.32: Turbulent dissipation for different orifice plates with different diameters and similar length

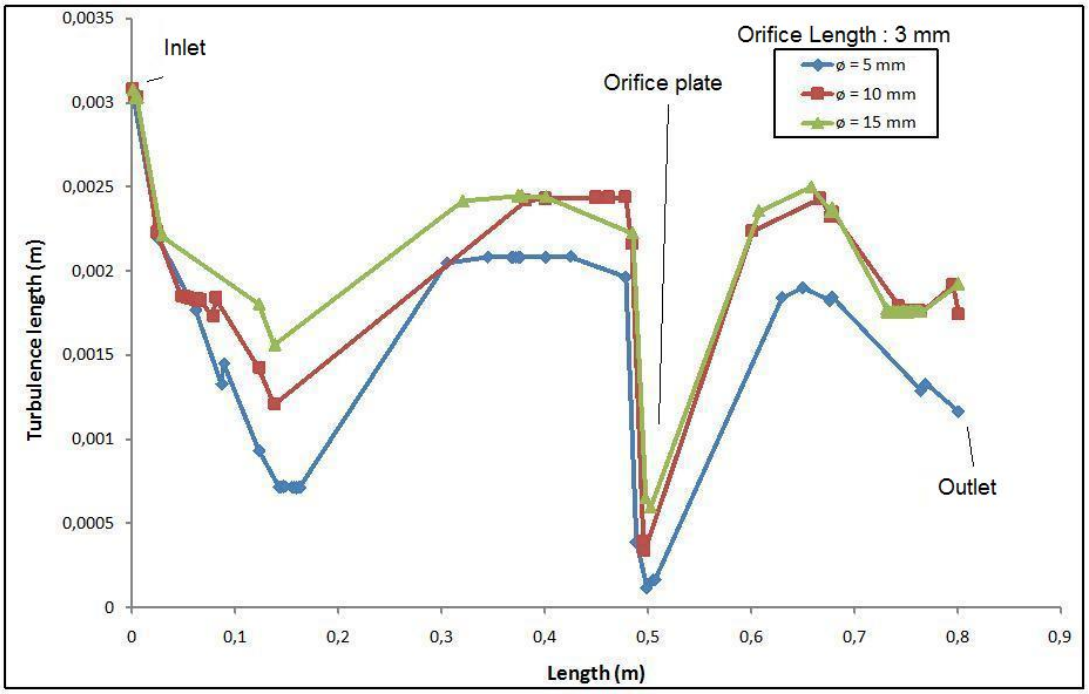

Figure 2.33: Turbulent length for different orifice plates with different diameters and similar length

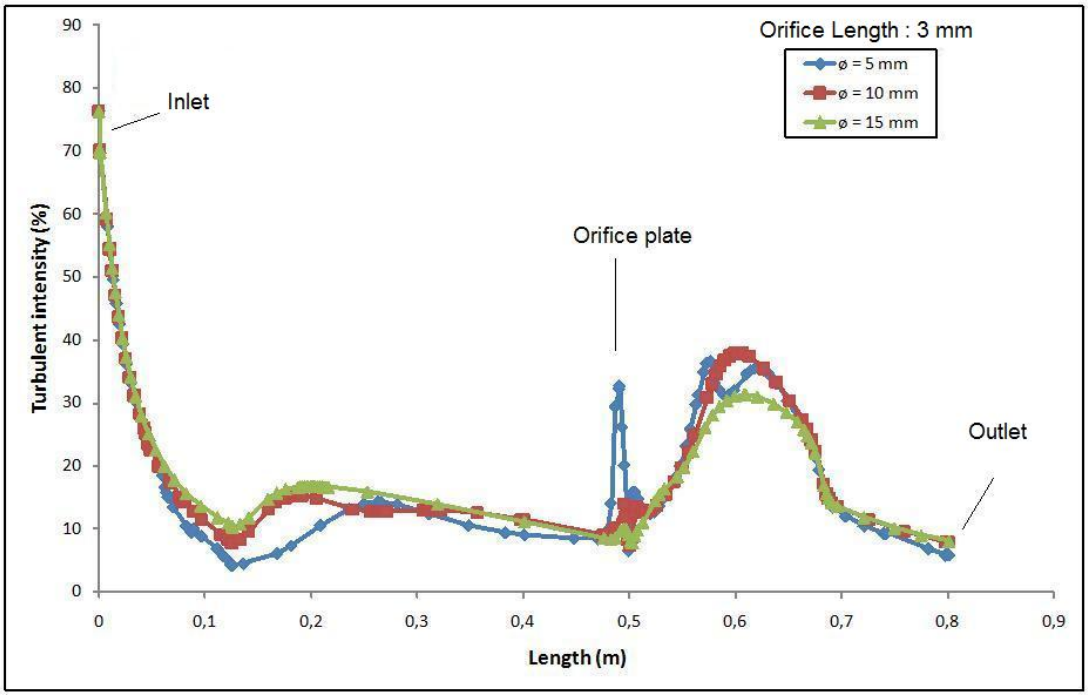

Figure 2.34: Turbulent intensity for different orifice plates with different diameters and similar length

Coanda effect

Contrary of what has been published (see article [53]) there is no symmetry in the recirculation length found after the constriction. This asymmetry is related to the Coanda effect and was confirmed even at very high Reynolds numbers by Cherdron [54].

This Coanda effect was found to be related to the step height of the sudden expansion. This can be seen by comparing the streamline analysis of the 10 mm in-diameter orifice plate (figure 2.35) and the streamline figure of the 5 mm in-diameter orifice plate (figure 2.36). The asymmetry of the eddies produces a higher level of instability inside the flow. To avoid this phenomenon, gradual steps or streamlined tubes are commonly used. Here we must point out the two different theoretical process involved with these two different technologies of turbulence generators. The first one takes into account the fact that flocs are broken by the strong acceleration at the inlet of the tube bank. Then, using a constant enlargement gradient (streamlined), the flow is distributed inside the nozzle in the most possible continuous way. In other words, elongational stress, as described before in section 1.3, is used to break up flocs. Turbulence intensity is applied at the beginning of the tube and then and then a homogeneous pulp is distributed into the nozzle using a constant gradient enlargement. The second theoretical description considers that acceleration at the inlet only modifies the shape of flocs (stretching them) and deflocculation occurs owing to the strong shear stresses produced at the wakes of a step jump. It has been demonstrated [55] that the turbulence intensity and scale at the wake is related to

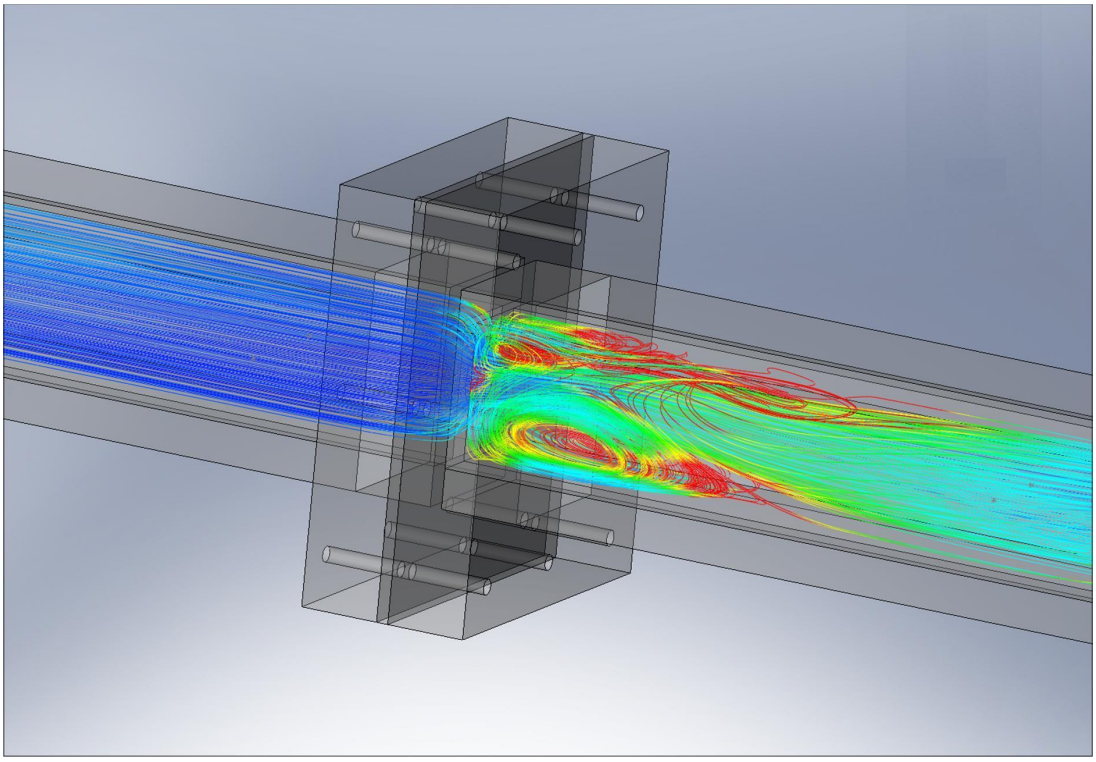

Figure 2.35: Streamline analysis after an orifice plate (10 mm in-diameter orifice) coloured by turbulence intensity

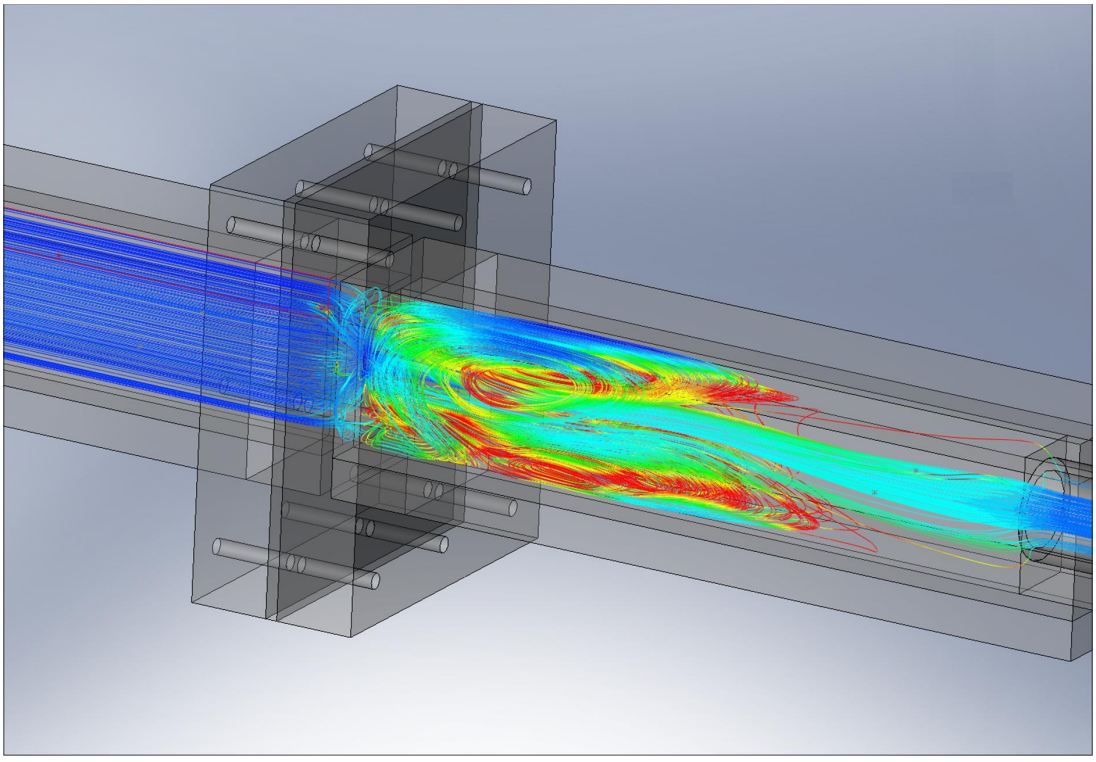

Figure 2.36: Streamline analysis after an orifice plate (5 mm in-diameter orifice) coloured by turbulence intensity

the step height. If the turbulence scale is smaller than the mean floc size, then the floc can be eroded at its surface and reduced in size. If we repeat this operation several times changing the step jump, then most of the flocs should disappear at the outlet of the tube bank and the Coanda effect reduced.

2.3.2 Application to a tube bank

The tube bank studied in this section is a three step sudden expansion tube bank. The first step is a cylindrical tube of 17 mm in diameter, the second step is a cylindrical tube of 22 mm and the last step is a squared tube of 27 mm interior side. The total tube bank consists in a 17 by 3 matrix as shown in figure 2.37. A streamlined turbulence generator is studied later in this section. We should keep in mind that, in an industrial setup, some geometrical restrictions apply. The inlet of each tube is generally of circular section with an internal diameter of around 17 mm. This value was determined empirically to avoid fibre clumps of the entire setup. The outlet of the tube bank should fill the entire headbox width to avoid wakes in the flow and by this avoid perturbation at the nozzle zone. This is why the tube bank outlet is generally not of a circular section but most of the time of rectangular or hexagonal section that entirely covers the nozzle section. The way the outlets are distributed is also of extremely importance. If they are placed in a column structure some secondary waves could be created originating some small scale perturbations at the flow. These perturbations can be the origin of the streaks structures found in a sheet of paper. This phenomenon was already treated and verified by Aidun [56]. As Aidun suggested, these streaks can be minimised by a staggered placement of the outlets of the turbulence generators.

Computational fluid dynamics simulations

It can be seen (see figure 2.38) that the Coanda effect is not present at a real tube-bank geometry using gradual steps of sudden expansions. In other words the recirculation length found in this geometrical configuration is symmetrical in all axes. This is due to the flow speed and the size of the steps that are small enough to keep a symmetrical flow. However the turbulent intensity is quite high, the recirculation structures are still present in this flow and they are of a certain length, which could be rather disturbing for regaining a stable velocity profile. It has been shown before that the rotational movement of the flow (eddies formed at the jump step) regenerates strong flocs structures. The presence of big re-circulation eddies inside a turbulence generator must be taken with caution because of the final balance between eroded flocs versus new generated flocs which can be quite annoying for papermaking. With this process we are transforming an almost continuum of interlinked fibres into several small-size flocs attached together with hard-to-break links.

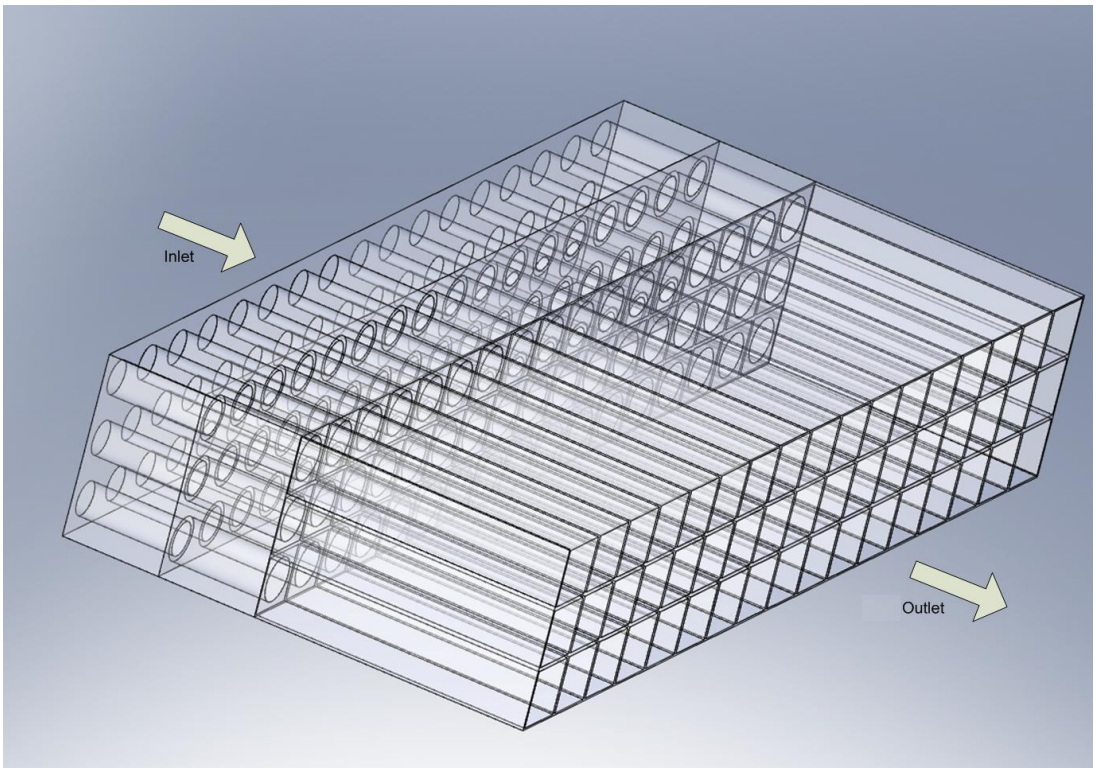

Figure 2.37: Tube bank setup

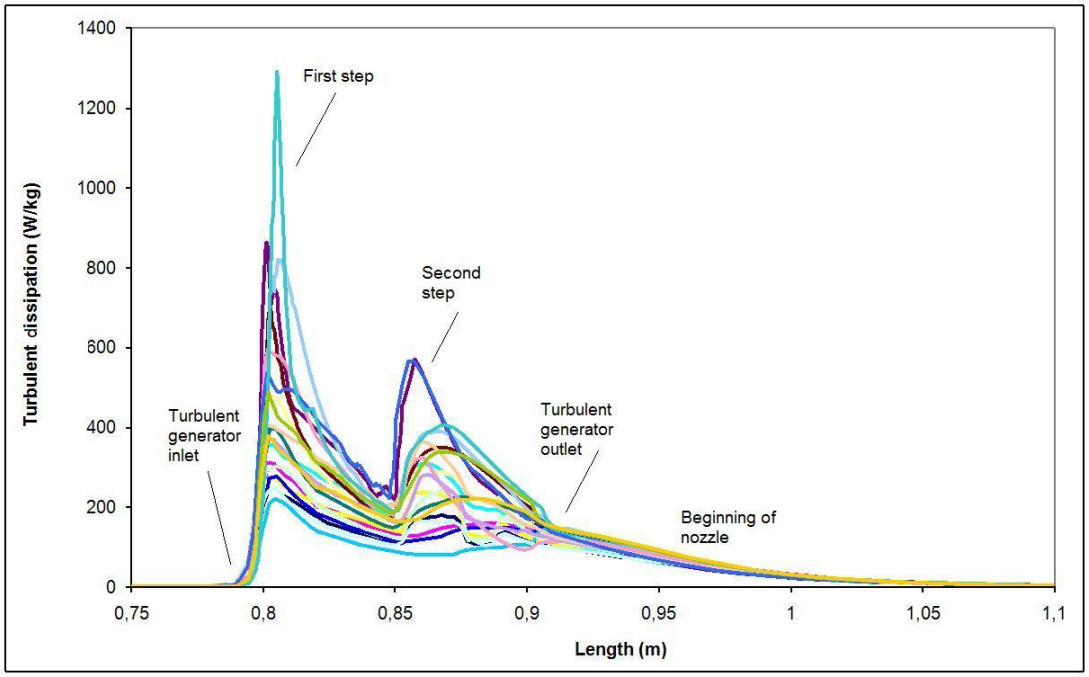

Figure 2.38: Turbulence dissipation inside a tube bank with steps (20 traces)

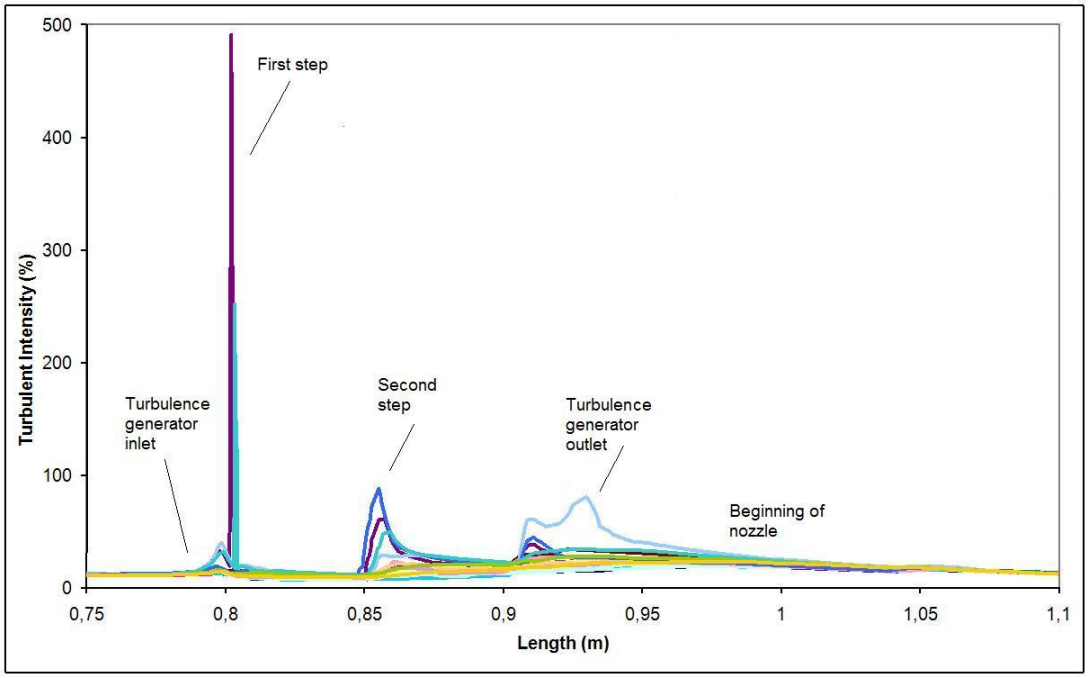

Figure 2.39: Turbulence intensity inside a tube bank with steps (20 traces)

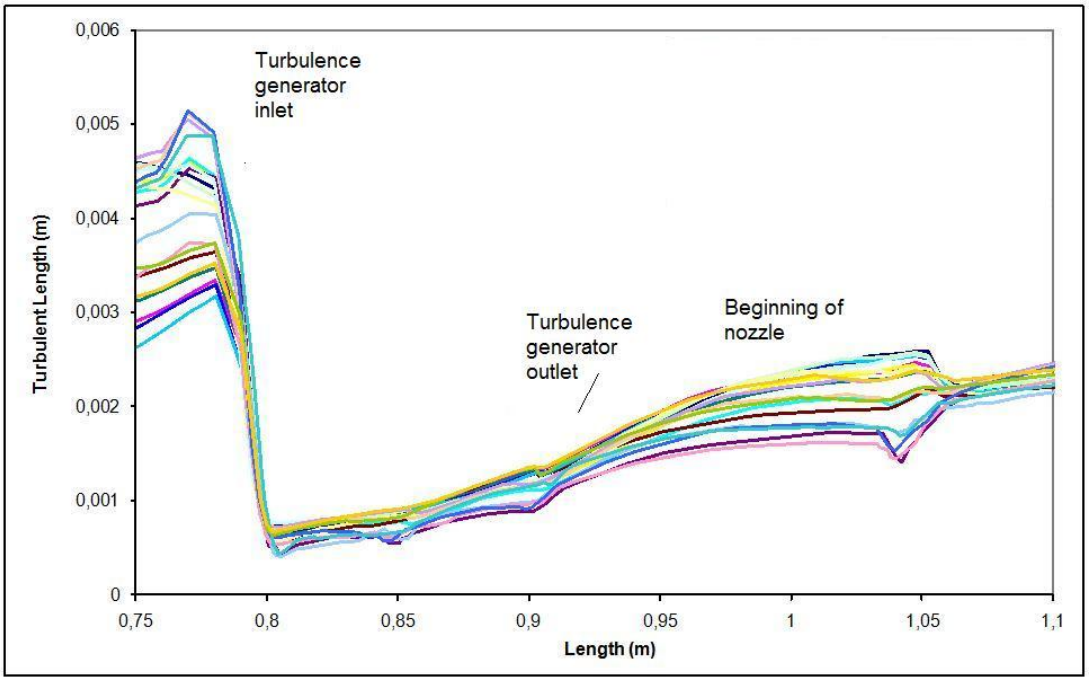

Figure 2.40: Turbulence length inside a tube bank with steps (20 traces)

If we look at the results concerning the streamline study inside the turbulence generator (see figures 2.41 and 2.42), we can see that no Coanda effect is present after the biggest sudden expansion. Even though some big eddies are observed at figure 2.41, the size of these eddies is not big enough to perturb the global flow as shown in figure 2.42.

For the turbulence study we injected 200 particles at the inlet of the setup and then we recovered the traces of these particles. For each of these curves we can calculate all the fluid parameters, i.e. turbulence intensity, turbulence dissipation, etc. For graphical reasons we have kept 20 of this traces in the next figures. The tube bank begins at a total length of 0.8 metre and ends at 1.05 metre. The turbulence dissipation figure 2.38 shows that the mean value at the inlet of the tube bank is around 700 W/kg of fluid. We can observe that for a certain trace the value of turbulence dissipation can reach 1200 W/kg. This particular trace is the one with the highest acceleration, i.e. the trace near to the bottom wall in this particular case. For the first sudden expansion (around 0.85 metre of the total length), the turbulence dissipation has a mean value of 300 W/kg of fluid. We can notice that the turbulence dissipation can reach almost 600 W/kg for some traces, depending on the recirculation structures. For the second sudden expansion (at 0.9 metre of total length) there is a mean turbulence dissipation of about 180 W/kg.

At the turbulence intensity figure 2.39 we can notice that most of the traces have a small value of turbulence intensity (less than 50%). However, high turbulence intensity was found for some traces. These high values of turbulence intensity are related to the particles having the highest acceleration. The turbulence length figure 2.40 is very interesting. We can see that at the entrance of the tube bank the mean value of turbulence length is about 4 millimetres. Then, at the inlet itself, the turbulence length is reduced to 0.5 millimetre. After all the sudden expansions the turbulence length reaches a mean value of around 2 millimetres.

We take now a streamlined tube bank as shown in figure 2.43 and trace the same figures as above. However, an equivalent amount of turbulence intensity is applied at the inlet of this tube. This type of turbulence generator is at least as efficient as the other type. It therefore can be concluded that the main deflocculation parameter is not the shear stress at the step jump but the elongational stress of the accelerating flow at the inlet. It can also be concluded that high turbulence intensity and small size turbulence length are needed to get a better deflocculation process.

From another point of view, there is a paramount question that is still without answer: Is this turbulent energy applied efficiently to the fibres by a step turbulence generator or by a streamlined one?

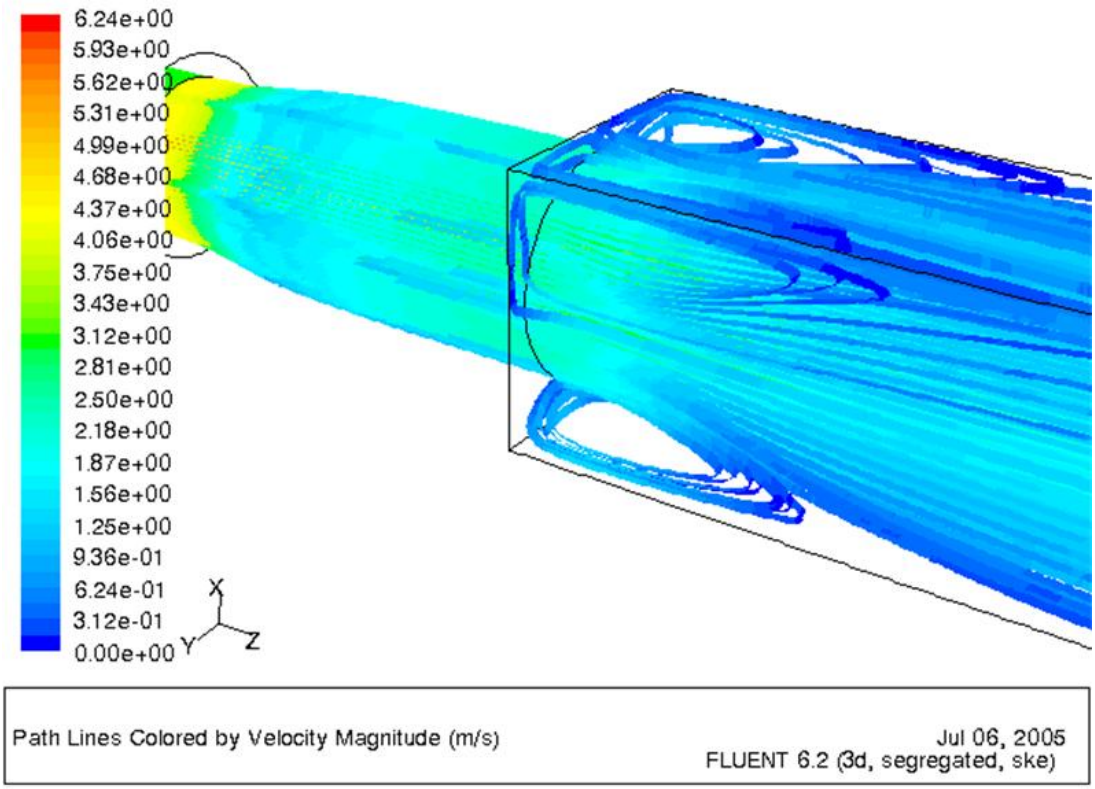

Figure 2.41: Streamline analysis of a single tube (recirculation structure)

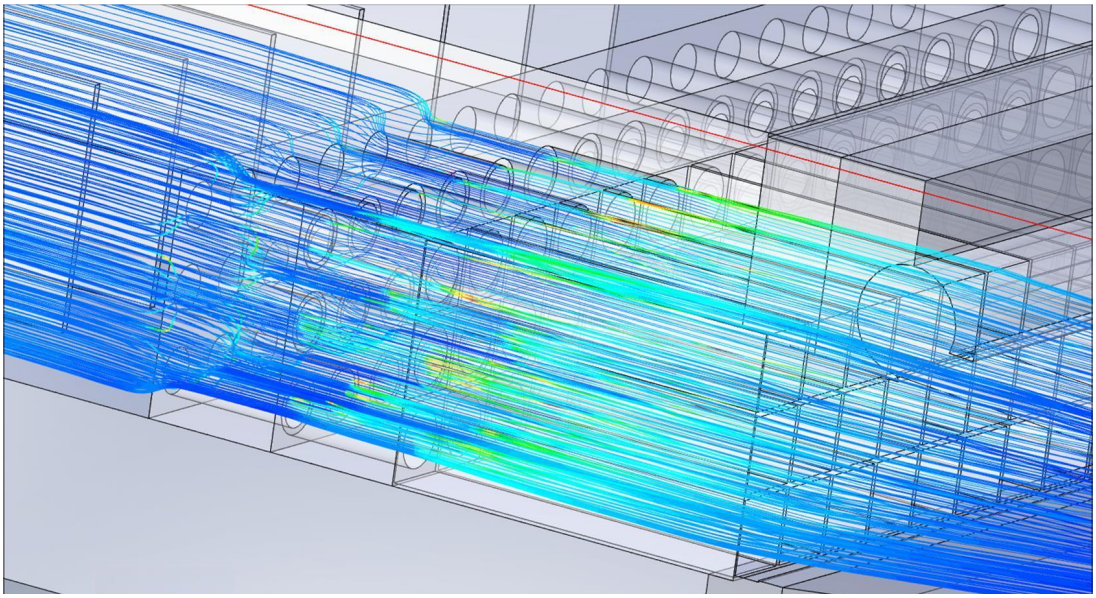

Figure 2.42: Streamline analysis for a tube bank

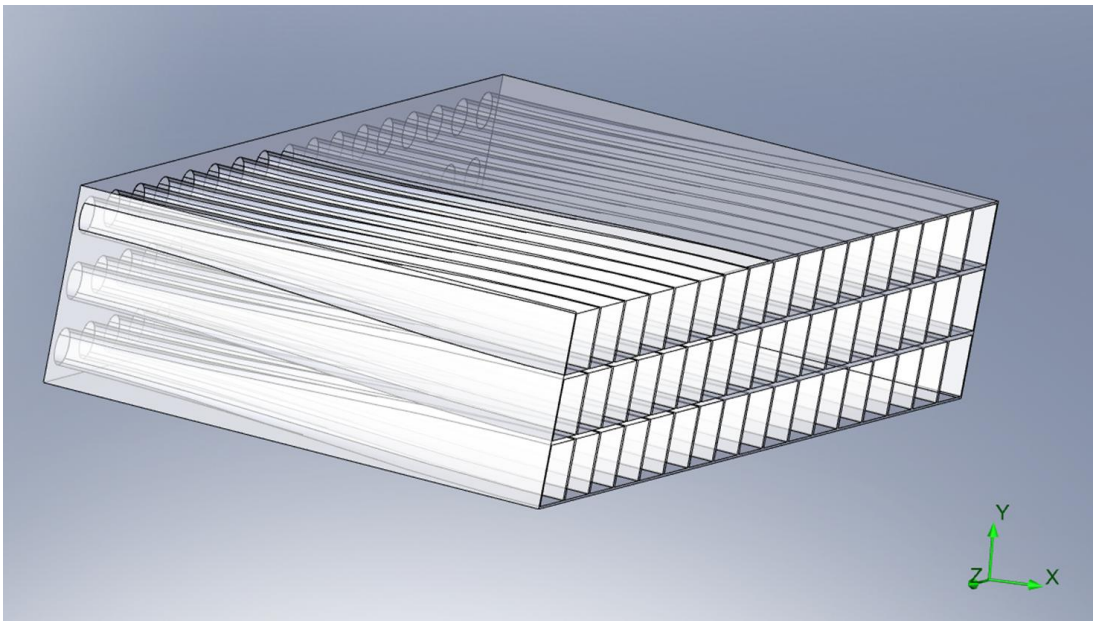

Figure 2.43: Streamlined tube bank setup

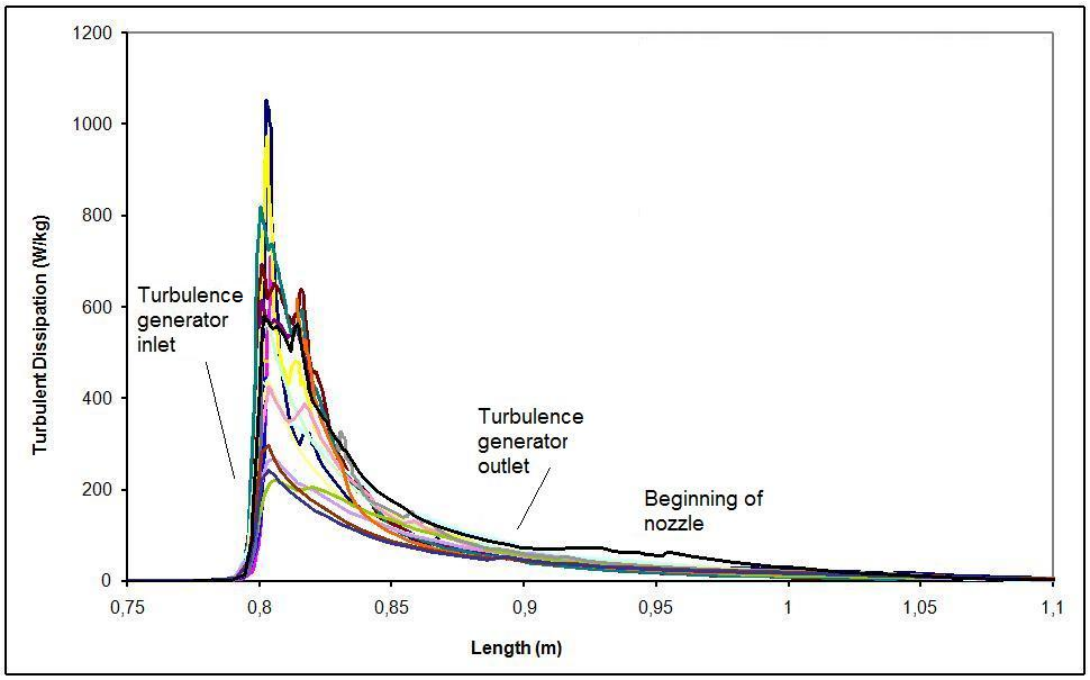

Figure 2.44: Turbulence dissipation inside a streamlined tube bank (20 traces)

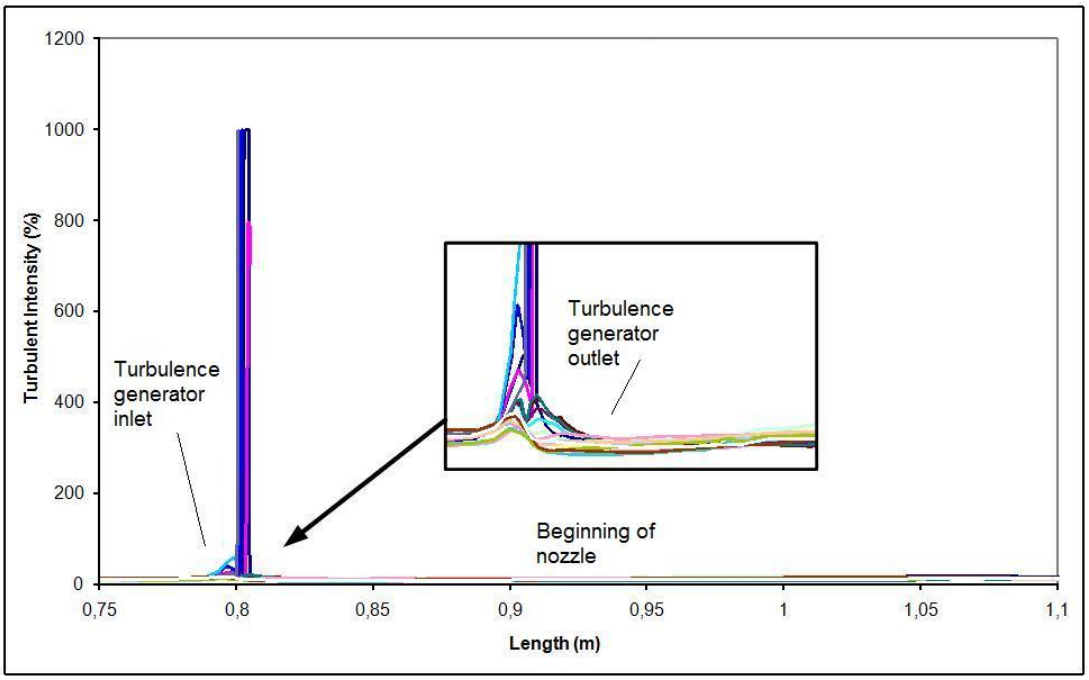

Figure 2.45: Turbulence intensity inside a streamlined tube bank (20 traces)

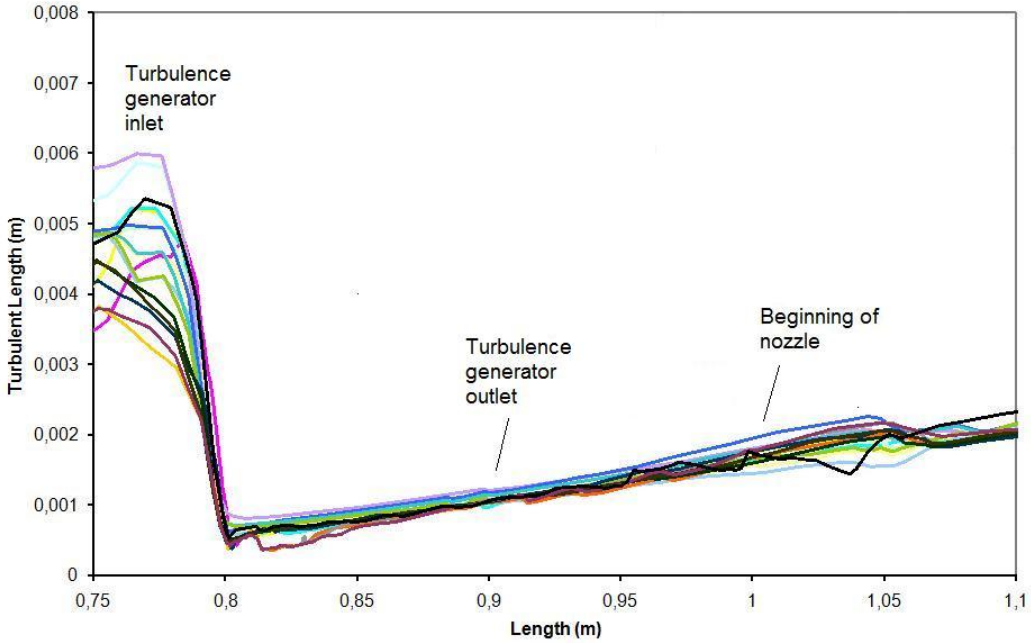

Figure 2.46: Turbulence length inside a streamlined tube bank (20 traces)

Several high speed motion images were taken before and after the tube bank at normal industrial flow conditions. From our observations, there is no noticeable deflocculation effect. Many flocs were observed and measured by image analysis techniques. No differences were found, at least in size matters, of flocs at these two locations. These observations make us believe that most of the energy applied at the tube bank is wasted in the liquid itself and not used for the deflocculation process. However, industrial experience has shown us that there was an improvement in paper formation by the use of a turbulent generator. We could think of three possible reasons to explain this phenomenon. The first one could be summarised as a problem of observation scale. Some searchers think that the big size flocs are not as important as the small size flocs to get proper formation. This would mean that even though we could observe big structures flowing inside the nozzle they are going to be properly disrupted at the sheet forming stage. Only small size flocs are going to disturb the forming process. From our observations, big structures are generally formed by a collection of small flocs at the inlet of the turbulence generator and these small structures are also seen after the passage through the tube bank. However it was impossible to us to determine a population of flocs of a certain scale before and after the turbulence generator. We believe that the size of flocs could be one of the most important parameter, because if a floc is eroded or broken, then the size of flocs at the nozzle should be inferior to the ones found before the turbulence generator. Knowing that a floc is reformed in only a few milliseconds, it is quite logical to think that the size of a structure found at the nozzle section could be similar to the original one, then we could ask: What is the point to apply a strong turbulent intensity knowing that, at the nozzle, the flocs are going to be reformed in a similar way? Our observations were made in the near-wall region (where the most of the shear stress is applied), then we must conclude that in the middle-flow region there are bigger structures than the ones observed.

A second possibility for explaining the efficiency of a tube bank is the memory effect which was described before (see section 2.2). If this effect exists then it would mean that the size of flocs does not change but the inter-fibre link strength does. I thought of an analogy to try to explain this idea: If we take a wool knot and then we apply a sudden energy (blowing in it) most of the times this knot is not going to disappear but its fibres are going to loosen one to each other and then the inter-fibre links are going to be weaker and the knot will be easier to disrupt. Similarly, the energy applied to the flocs could give this loosening to the fibre links and therefore the flocs do not change in size but in coherence. This sounds quite logical, but it is almost impossible to measure.
The third explanation is related to the incertitude of the measuring techniques applied to determine a deflocculation level. Most of the techniques known up to day worked in a narrow vane that is not representative of the real boundary conditions inside a headbox,

giving us some wrong conclusions about the deflocculation process. There is no practical method nowadays to determine a precise floc size in a 3D flow. We always have certain incertitude of the depth of field of the images taken, and if we reduce the size of the gap between walls then the wall effects change the flowing conditions. Several optical methods were proposed during the last 10 years. However there are no meaningful values for these measurements because they depend on the threshold level imposed at the image analysis. This threshold level is arbitrary imposed and can completely change our conclusions of the deflocculation level, furthermore there is always the scale problem in the definition of a floc. A floc is defined whenever a fibre has three or more contacts restraining it to any possible movement in the space. If we keep this definition in mind then, the whole fibrous suspension, at an industrial consistency level, can be considered as a single floc. Now, in this giant floc, if we take care to look in a more detailed way we can see that it is not homogeneous and several concentrated fibrous regions are attached to each other, and this structure can be found almost at any scale. This "semi-fractal" representation of the pulp flocculation is one of the main problems with the flocculation definition, because we should speak of a certain degree of flocculation for a corresponding scale and not of a general flocculation degree. This approach was found in the doctoral thesis work by Yan [57] where he developed a wavelet description of the pulp. This representation should be more studied to a better application in industrial conditions. In our case it was impossible to use this methodology because of the depth of the headbox and the amount of light needed for the high speed motion images.

Conclusion of turbulence generator study

A complete characterisation was made of a laboratory scale thick orifice plate used as a single step turbulence generator. This setup was used to make a comparison between water and different pulps. From an energetical point of view we can say that the turbulent generators can be designed using only water as the flowing fluid. Some geometrical considerations should be kept on mind:

- The smallest inlet diameter should be kept but not small enough to clog the entire setup. A 15 mm diameter should be a good compromise.
- The length of the tube bank should be designed to regain a stable velocity profile but not a squared velocity profile.
- The geometry of the tube bank should be modified according to the type of pulp and its concentration. These results are in complete agreement with the work of Salmela [55] where he showed the efficiency of deflocculation according to the step height as shown in figure 2.47
- The Coanda effect should be avoided. This could be made by choosing small enough step jumps. It is better to have several small step jumps than few big ones.

- Even better is to have a streamlined turbulence generator in order to avoid the recirculation lengths.
- The outlet walls should be as thin as possible to avoid wakes.
- A staggered configuration is necessary to minimise the formation of streaks

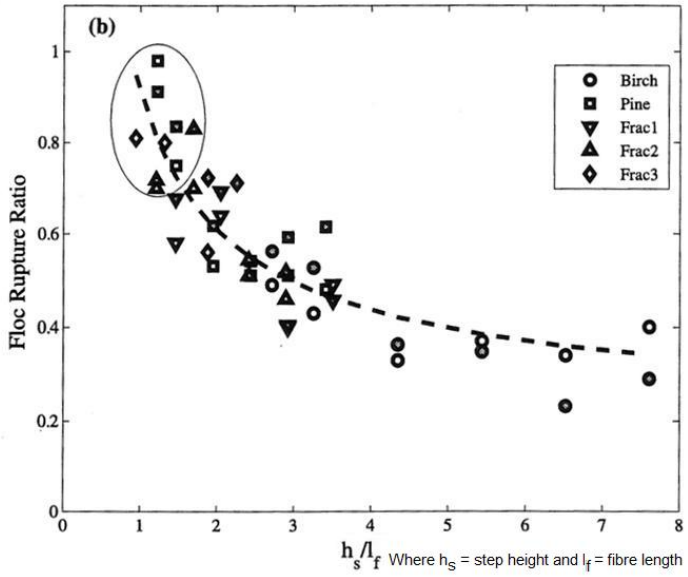

Figure 2.47: Results obtained by Salmela regarding floc rupture as a function of step height

Even if all these parameters are respected, a more interesting discussion was developed about the utility of a tube bank and its real effect on a fibrous suspension. Some high speed images were taken and no noticeable changing, in size matters, was remarked. This would mean that the energy disposed in this device is completely lost in the liquid medium and not employed for a deflocculation process. Another kind of turbulence generator technology could be proposed, such as an ultrasound device, giving only a certain degree of activation to fibres and not water. A similar operation was already studied and developed by Ultra technology Europe AB (http://www.ultratechnology.se/). They have developed an ultrasonic foil that gives activity to fibres only and not water. We could think that this kind of technology can be used inside a turbulence generator but due to the volume of suspension to be treated, the amount of ultrasonic energy needed makes this operation too expensive to be considered. Furthermore this big amount of ultrasonic energy could be too risky to the personal working in the near by region.

However, industrial experience showed us a real improvement in sheet formation when a turbulence generator is operational. Three different approaches were tried to explain this, unfortunately the measuring techniques available did not allow us to reasonably measure the floc size and the inter-fibre strength. Another measuring technique should be developed to better understand the real effect of turbulence inside a floc structure.

2.4 Nozzle and slice section study

As it was described before, the principal function of the nozzle is to accelerate the pulp to an acceptable industrial speed. Most of the people think that this is the only function of the nozzle. However some design advice should be kept in mind to get the most coherent jet core. The next advices are conceived for coherent water jet production especially applied in mining applications (from [58]) but they can be applied for our case because it is the same type of problematic. We present first the general design advice for a general nozzle and then the papermaking restrictions or working parameters actually used in industry:

- *Nozzle inlet flow should be free of large scale turbulent eddies, and be free of any rotational or swirl components.* In papermaking the inlet of the nozzle is at the end of the tube bank, generally big turbulent eddies can be found, depending on the tube bank geometry and the flow rate passing through it. If no fabrication default is present at the tube bank, there should not be swirl flows. However, depending on the layout of the tube bank outlet some periodical rotational flows could be found.
- *The nozzle inlet should have a minimum turbulent intensity.* In our case, it consider that to keep a high deflocculated pulp a small scale, high turbulent intensity is needed all along the nozzle.
- *Protruding gaskets must be avoided between inlet piping and the nozzle itself, if steps are unavoidable they should be expanding rather than contracting and ideally step height should be restricted to the order of the local laminar sublayer thickness.* Considering our pilot headbox, the nozzle studied is not symmetrical. This forced the use of a step or a joint between the tube bank and the nozzle. No disturbances were observed at this place, but it could be a source of non-homogeneity at the jet. A big discussion could be taken out at this point, whenever we worked with a Newtonian liquid it seems logical to think that the step height should be restricted to the order of the laminar sublayer thickness, however, when we use a fibrous suspension we cannot talk of a laminar sublayer and we cannot either say that it is a homogeneous fluid at this scale. The presence of fibres changes the whole behaviour of the flow and if there is a laminar sublayer its thickness is reduced to such a small value that it is hard to think that there is an influence on the behaviour of the flow.
- *Nozzle exit core flow turbulence intensities should be minimised by providing a sufficient contraction ratio of $10<CR<45$.* The contraction ratio is defined as the ratio between the heights of the inlet and the outlet. In our case it was 11.45 which is almost a lower limit of the contraction ratio wanted.

- *Nozzle exit boundary thickness should be minimised by ensuring some degree of nozzle exit taper, a minimum nozzle aspect ratio and a hydraulically smooth wall flow from nozzle approach section to nozzle exit.* The use of a slice at the end of the nozzle gives a sudden acceleration and avoids a parallel exit that is going to act as the nozzle taper mentioned above. The nozzle aspect ratio is defined as the ratio between the total length of the nozzle and the inlet height of it. It should trend to unity, in our headbox it was 4.39. Aidun [56] found that less streaks are formed whenever the nozzle aspect ratio becomes closer to unity.
- *Boundary layer separation at the nozzle inlet and subsequent generation of large-scale turbulence in resultant recirculation zones should be prevented.* This is related to the previous point, the nozzle aspect ratio should trend to unity but it should be taken quite cautiously because a separation of the boundary layer could be found generating big turbulent eddies. A cubic arc wall is advised at the inlet of the nozzle to prevent this effect.
- *Cavitation near the nozzle exit due to sharp changes in wall curvature and isolated roughness elements should be prevented.* In papermaking, the use of a slice at the nozzle end is quite common. This slice is generally a sudden change of inclination of the nozzle wall. If this angle is steep enough, cavitation should occur. However this is not the only problem, some dead zones with recirculations could appear in this region.
- *Retransition of a relaminarised boundary layer should occur within the nozzle.* This phenomenon, as explained before, is possible with a homogeneous fluid. With a fibrous suspension, the re-laminarisation of the boundary layer (if there is one) is almost improbable owing to the presence of fibres in the near wall region.

In order to keep a well deflocculated suspension, some headbox designers add at the nozzle interior some flexible vanes. Theses vanes are horizontal smooth separations inside the nozzle (see figure 2.48 for more details). This configuration is optimal to keep a high intensity, small-scale turbulence. The shear stress applied by the friction of these vanes is also used to get a higher deflocculation. The second advantage of this system is the possibility to make a multi-layer sheet combining the different mechanical properties of softwood and hardwood pulps in only one step. This allows the development of new products. These vanes, even if they give many advantageous properties to sheet formation, could generate other problems, like vibrations or z-direction mixing coming from a wake generation at the end of the vane. In our case we have not used vanes.

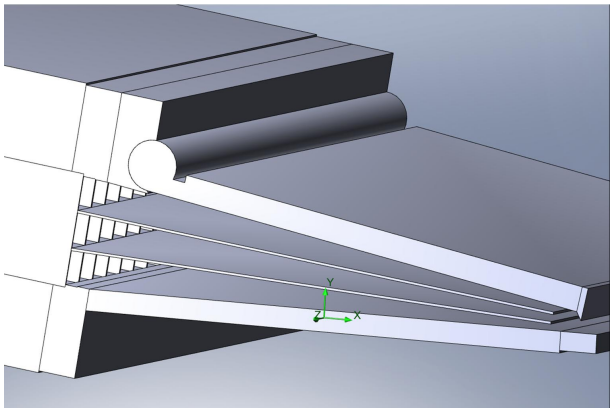

Figure 2.48: Headbox with vanes

The slice

The slice at the end of the nozzle is used to control the jet shape and to give a final acceleration to the fibrous suspension. In the papermaker's jargon it is common to say that the slice is used to "*flatten the jet*". In this work we were interested in the real use of this slice and to determine if it is really necessary or not. The first step to do is to determine if this slice could be the source of disturbances to the headbox good functioning. For this we have made detailed observation of this zone using the high speed motion camera at a frame rate of 4000 frames per second and using a fibrous suspension of a mixed hardwood-softwood pulp at 0.5% consistency. For all the angles of slice tested, the observations made us conclude that there is no separation of the boundary layer and the streamlines follows the shape of the slice. For some cases, with an angle superior to 80°, a really small dead-zone appears but its size is too little to cause a significant disturbance to the jet core. Nevertheless, it should be kept in mind as a source of disturbances, especially for streak formation at the jet surface. In order to validate these observations, a 2D computational fluid dynamics simulation was made using a commercial software (Fluent 6.2). The unstructured grid was performed using Gambit and the final grid used was tested to verify the independence of the grid size to the results. Of course, it is nearly impossible to simulate a real fibrous suspension with the hardware available for this work. Simulations with water were performed to compare to visual observation. The obtained results are really close to those observed with the high speed camera.

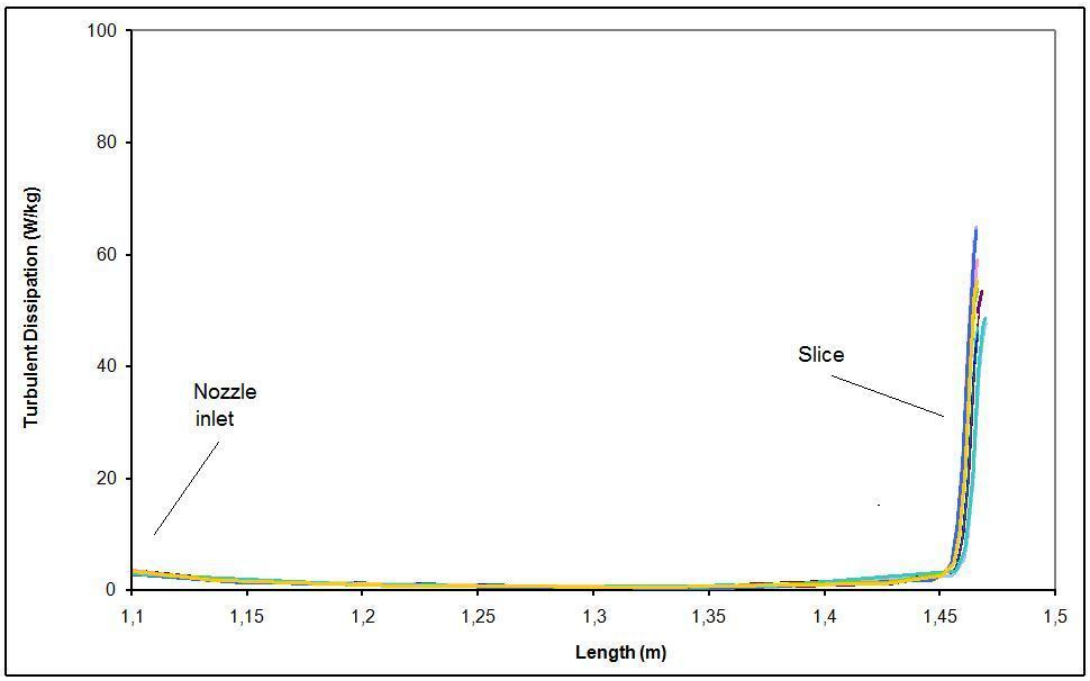

Figure 2.49: Turbulence dissipation inside nozzle (20 traces)

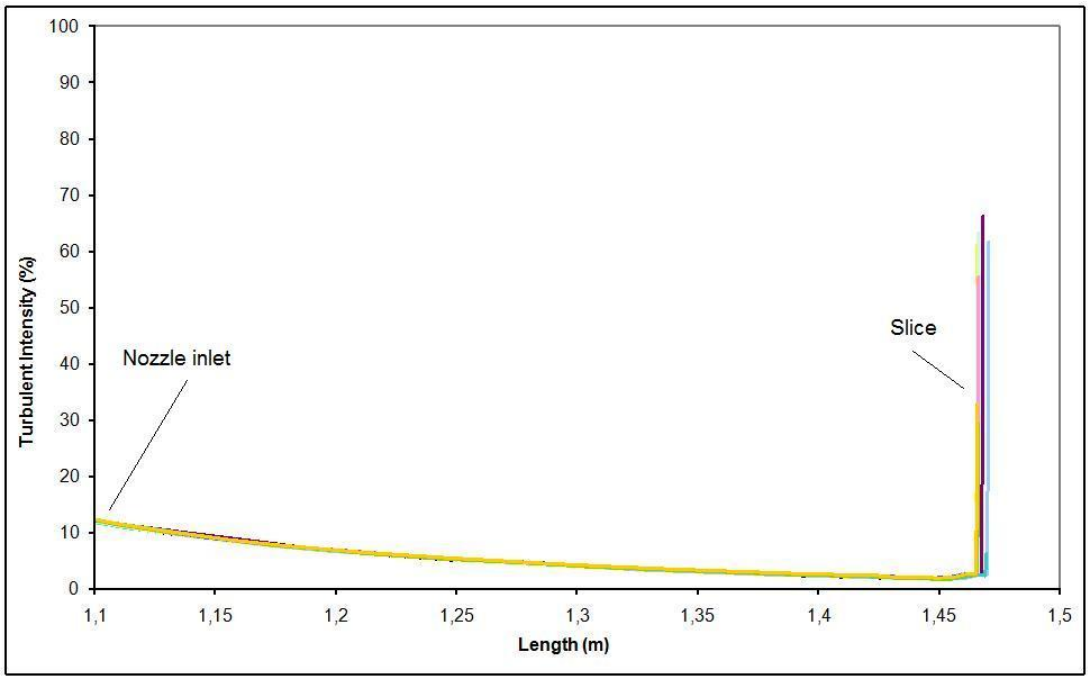

Figure 2.50: Turbulence intensity inside nozzle (20 traces)

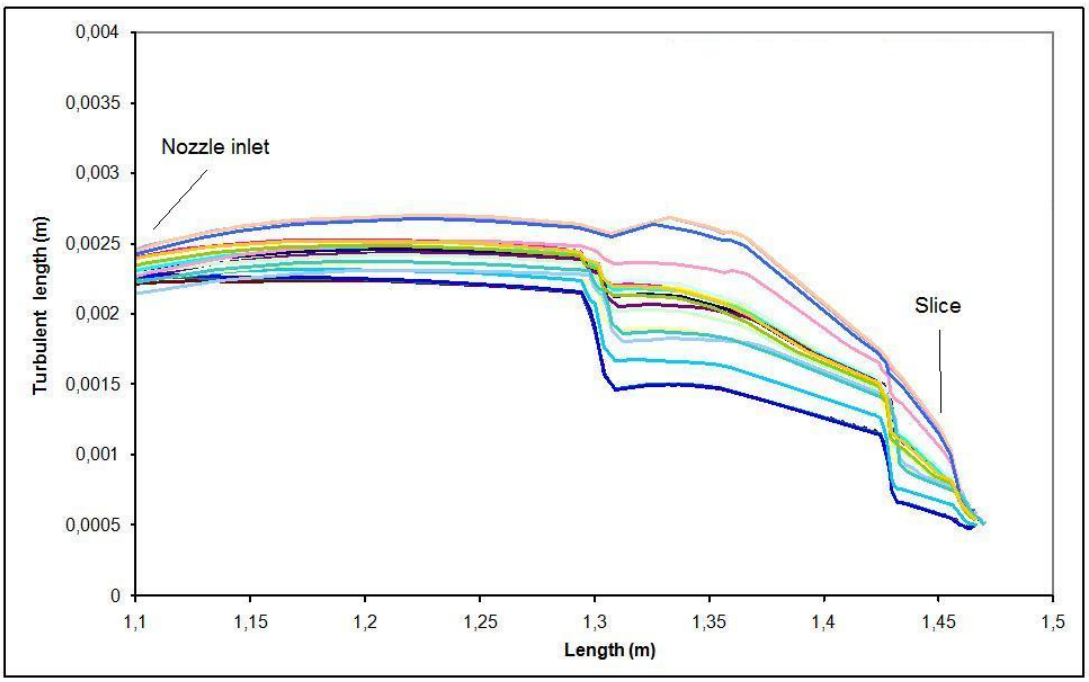

Figure 2.51: Turbulence length inside nozzle (20 traces)

Conclusion of nozzle and slice study

We can conclude that there is no dead zone at the intersection between the nozzle and the slice, or no significant dead zone, and there is no separation of the boundary layer. The visual observation let us see some flocs deforming at the sudden acceleration of the slice, however no floc rupture was seen. It is claimed that the slice works like a jet control. It was shown previously, at section 1.6.4, that geometrical values of the slice modified the jet shape. This is very interesting information because it means that knowing the exact geometrical configuration of the nozzle, the jet shape could be predicted and the jet impact calculated. Kerekes developed a practical method to predict the jet shape but only two conventional angles were treated. These results can be found at TAPPI technical information sheets 0410-03 [59] and 0410-04 [60]. No application to other geometrical setups was found and no validation for modern headboxes was either found. The first logical approach is to develop an easy numerical model and to compare these results to physical measured values of jet shape. For this, we have developed several models that are going to be presented in the next chapter.

2.5 Total headbox study

A computational fluid dynamics study of the entire headbox was made. The idea was to determine the influence of each device in a global operation of the headbox. For this we have begun from a simple headbox configuration and then started changing some geometrical parameters to verify the hypothesis made before. The cases analysed are described in table 2.4.

Cases analysed	General Description	Difference with other cases
Case N°1	800 mm long stabilisation chamber Three step turbulence generator 400 mm long nozzle 45° slice	Stabilisation chamber without compartments.
Case N°2	Exactly the same geometry as the prototype setup used for physical validation. 800 mm long stabilisation chamber Three step turbulence generator 400 mm long nozzle 45° slice	Stabilisation chamber with compartments
Case N°3	800 mm long stabilisation chamber with compartments. Streamlined turbulence generator 400 mm long nozzle 45° slice	Streamlined turbulence generator
Case N°4	400 mm long stabilisation chamber with compartments. Three step turbulence generator 400 mm long nozzle 45° slice	Half length stabilisation chamber
Case N°5	800 mm long stabilisation chamber Three step turbulence generator 400 mm long nozzle with lames 45° slice	Nozzle with vanes

Table 2.4: Different cases studied in this section

For each model a standard $k - \epsilon$ turbulence model was used. The inlet flow was considered as a completely developed turbulent flow. The first model analysed, as shown in figure 2.52, consists of a headbox with eight 43 mm diameter inlet pipes, with no compartments in the stabilisation chamber, a double step turbulence generator with an inlet of 17 mm, 240 mm total length and a squared 28 mm outlet, a nozzle with a contraction ratio of 11.45 and an angle of 10 degrees with respect to the horizontal plane. A slice of 7.8 mm length with an angle of 60 degrees with respect to the horizontal plane and a lip opening of 10 mm.

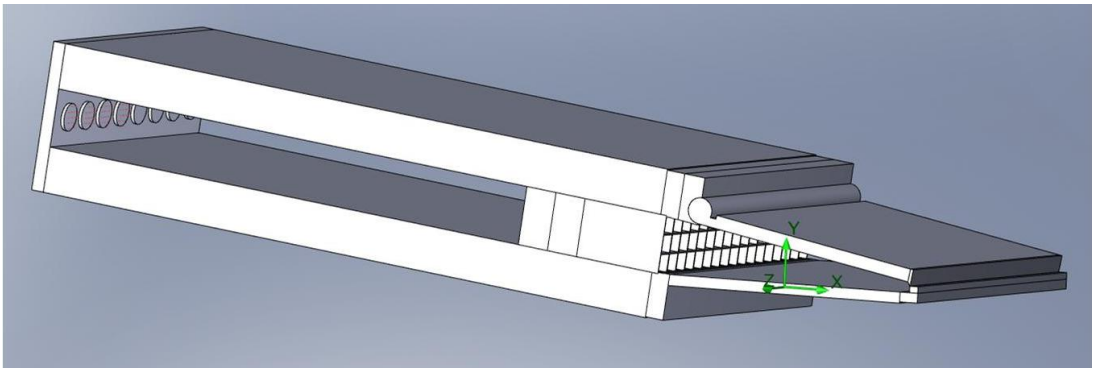

Figure 2.52: First Headbox configuration

The round/rectangular passage at the inlet of the stabilisation chamber generates big disturbances. These disturbances are going to generate secondary flows at the stabilisation chamber. This disturbed flow passes through the turbulence generator. The turbulence generator in this case acts as a homogenisation grid but this grid is not small enough to eliminate all the previous disturbances. Secondary flows appear once again in the nozzle section which should make the fibre mass distribution uneven. We must point out that in these conditions the secondary flows generated at the step turbulence generator are not important compared to the magnitude of the other perturbations.

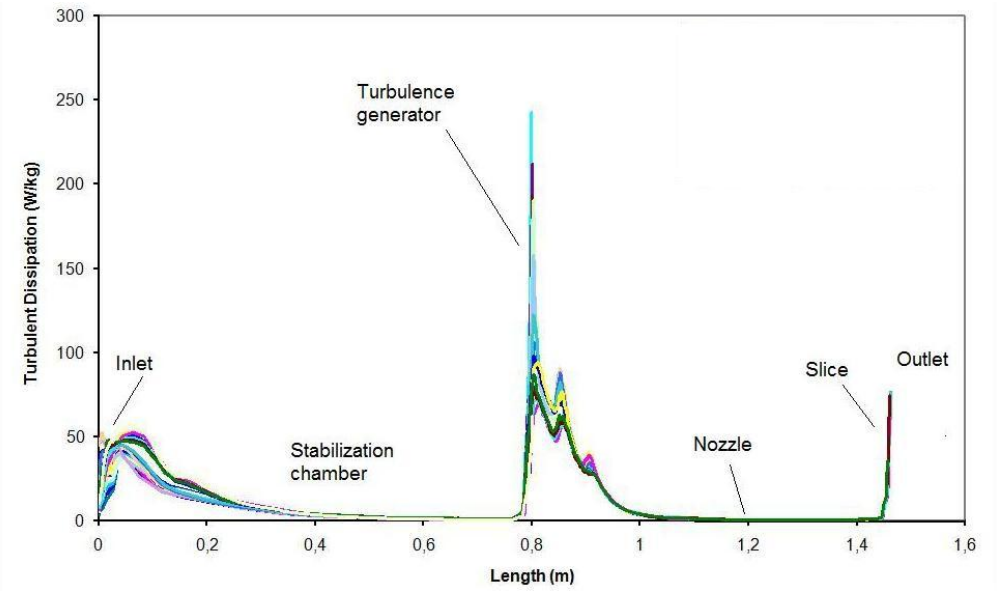

Figure 2.53: Turbulence dissipation inside the first headbox configuration (50 traces)

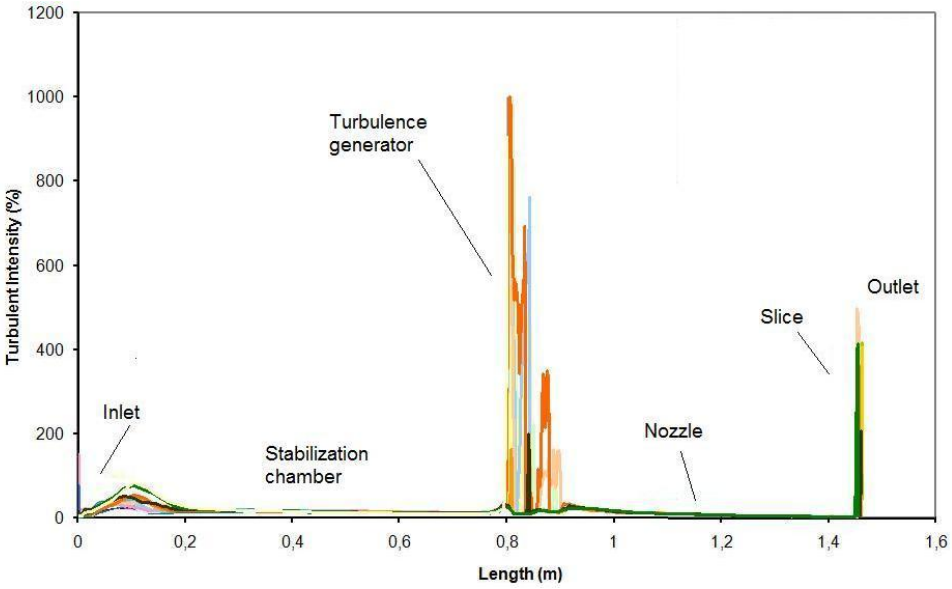

Figure 2.54: Turbulence intensity inside the first headbox configuration (50 traces)

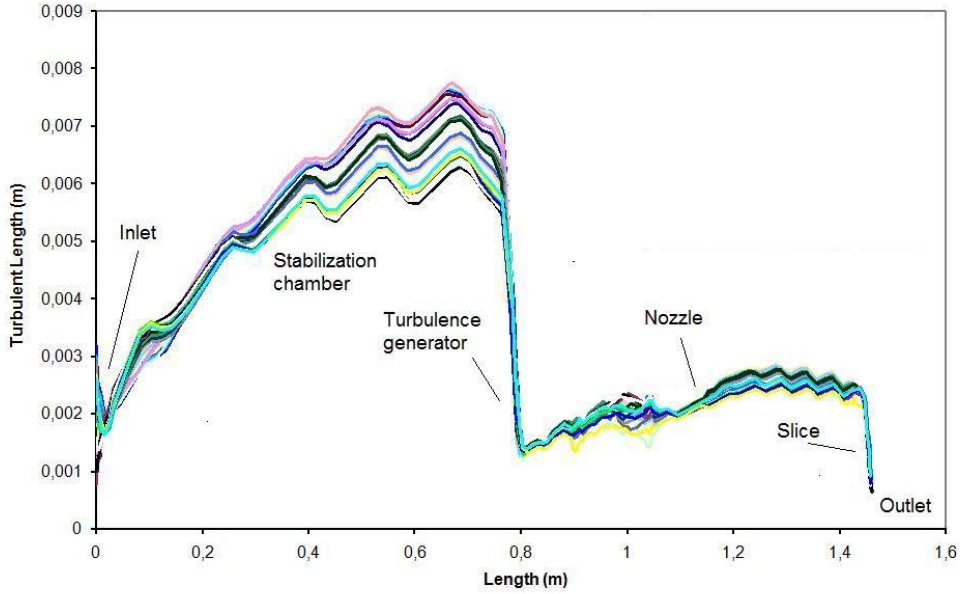

Figure 2.55: Turbulence length inside the first headbox configuration (50 traces)

The second model studied is the same headbox as before but with the application of the compartments in the stabilisation chamber (as shown in figure 2.56), a small mixing chamber was left just before the turbulence generator in order to ensure a perfect pressure gradient just before the entrance of the turbulence generator but small enough to avoid cross-direction mixing. The results for this kind of configuration are much better than the previous ones. Even though the recirculation structures are still present at the inlet of the stabilisation chamber, there is no mixing in the cross-direction, so a local control of the mass distribution is possible. The secondary flows generated at the step turbulence generator play a bigger role now so that the other disturbances in the cross-direction are minimised.

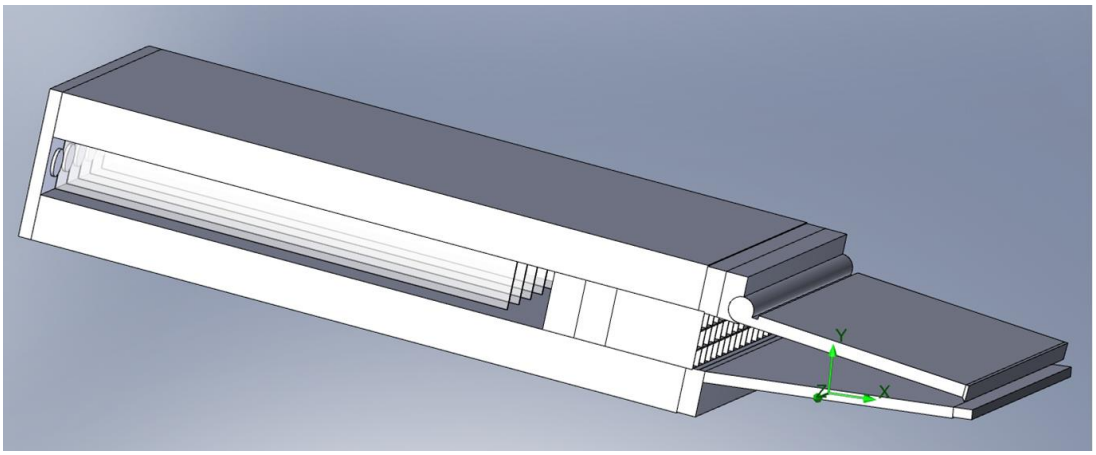

Figure 2.56: Second headbox configuration

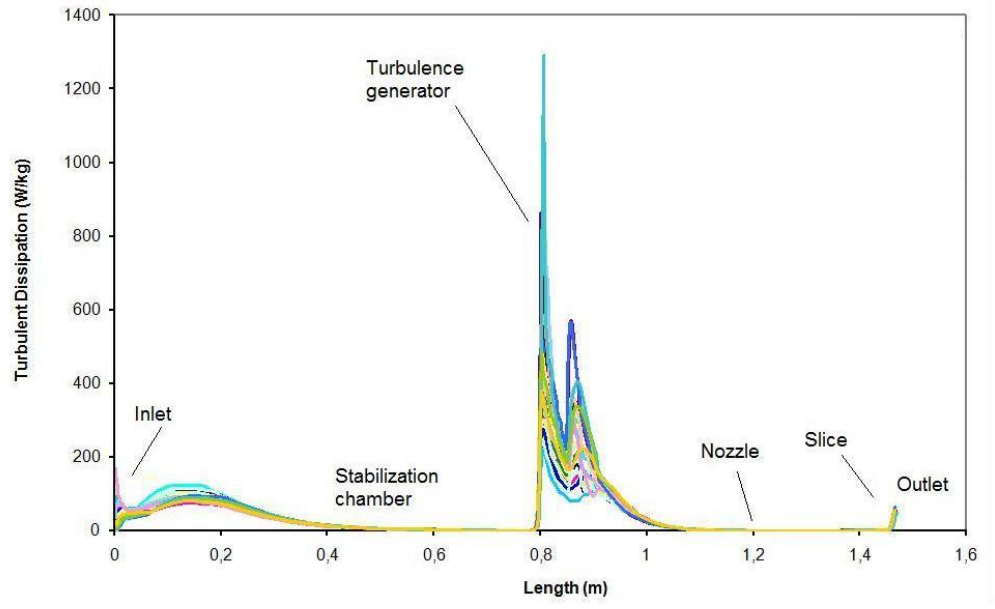

Figure 2.57: Turbulence dissipation inside the second headbox configuration (50 traces)

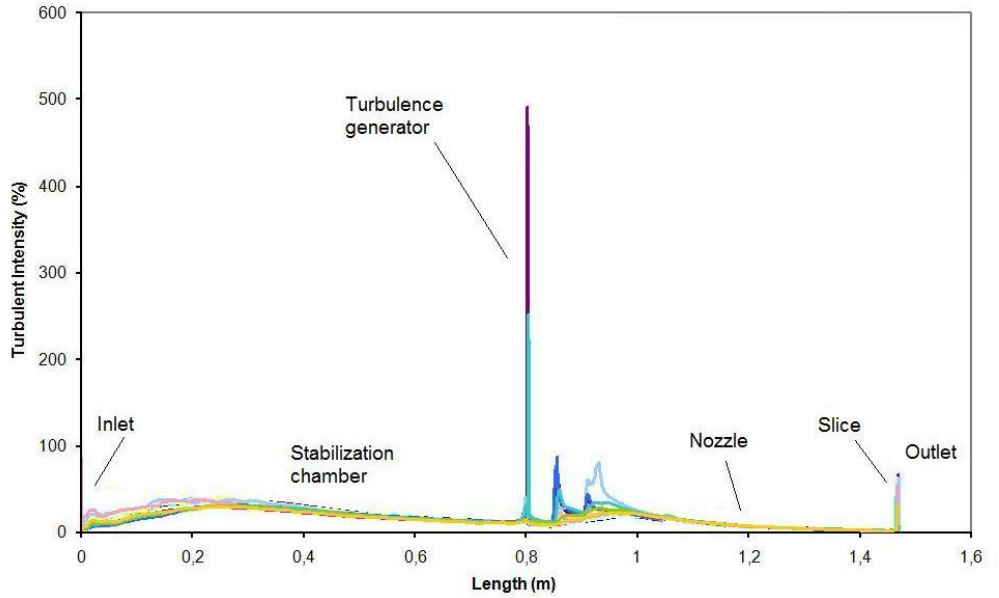

Figure 2.58: Turbulence intensity inside the second headbox configuration (50 traces)

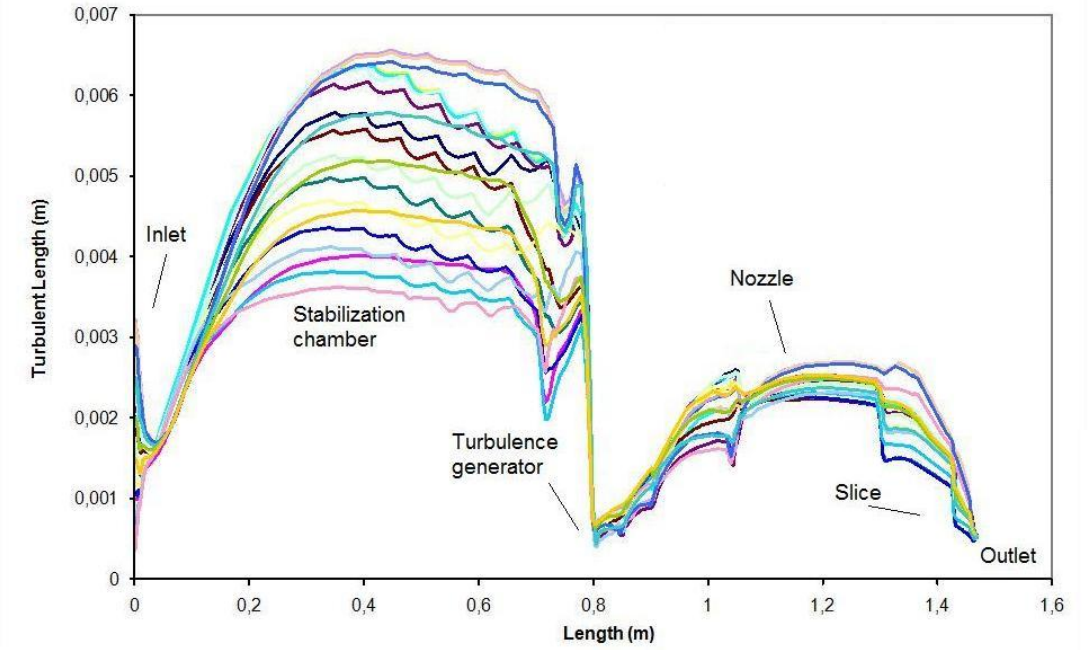

Figure 2.59: Turbulence length inside the second headbox configuration (50 traces)

The third model studied consists of the same headbox configuration as the previous one (model 2) but with a streamlined turbulence generator. This type of turbulence generator has already shown its efficiency and minimised the appearance of secondary flows due to the recirculation structures of a step turbulence generator. The results are quite encouraging because a more stable fluid arrives to the nozzle section but similar turbulence intensity is applied into the liquid.

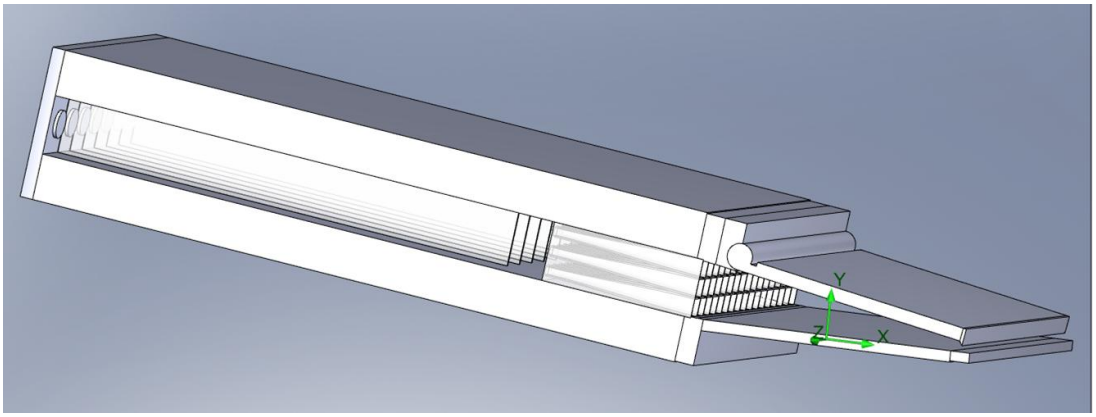

Figure 2.60: Third headbox configuration

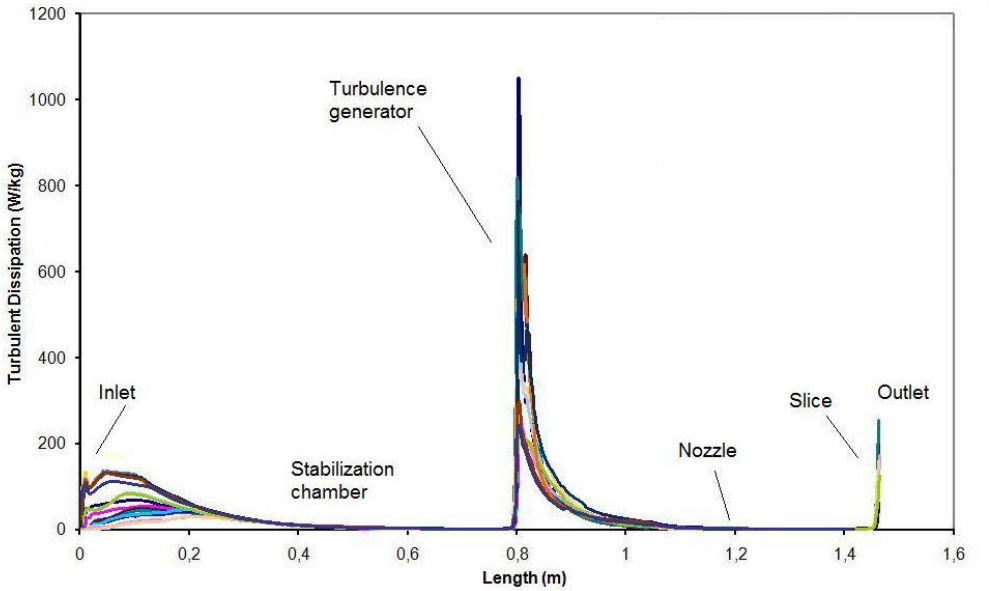

Figure 2.61: Turbulence dissipation inside the third headbox configuration (50 traces)

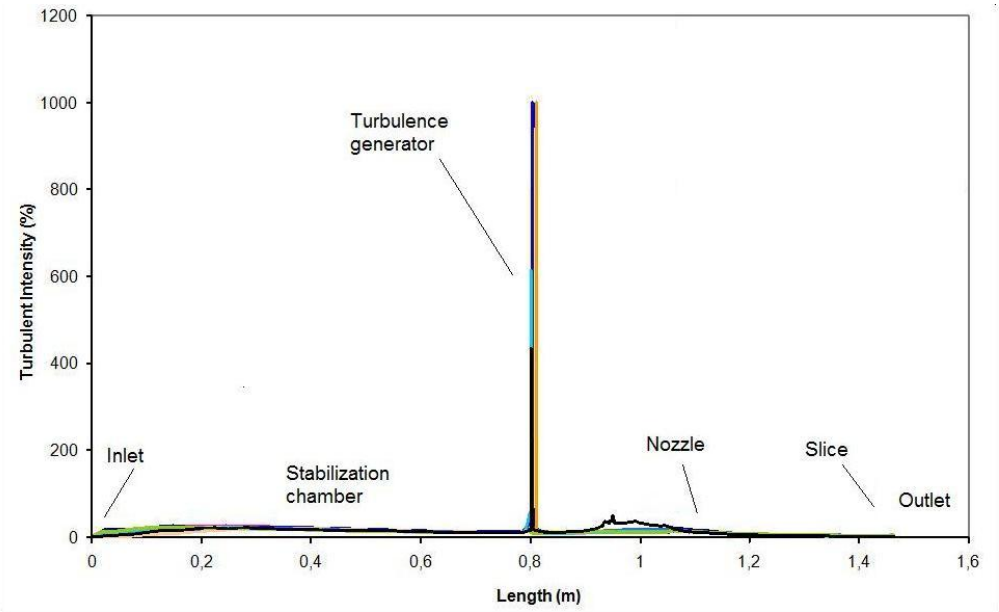

Figure 2.62: Turbulence intensity inside the third headbox configuration (50 traces)

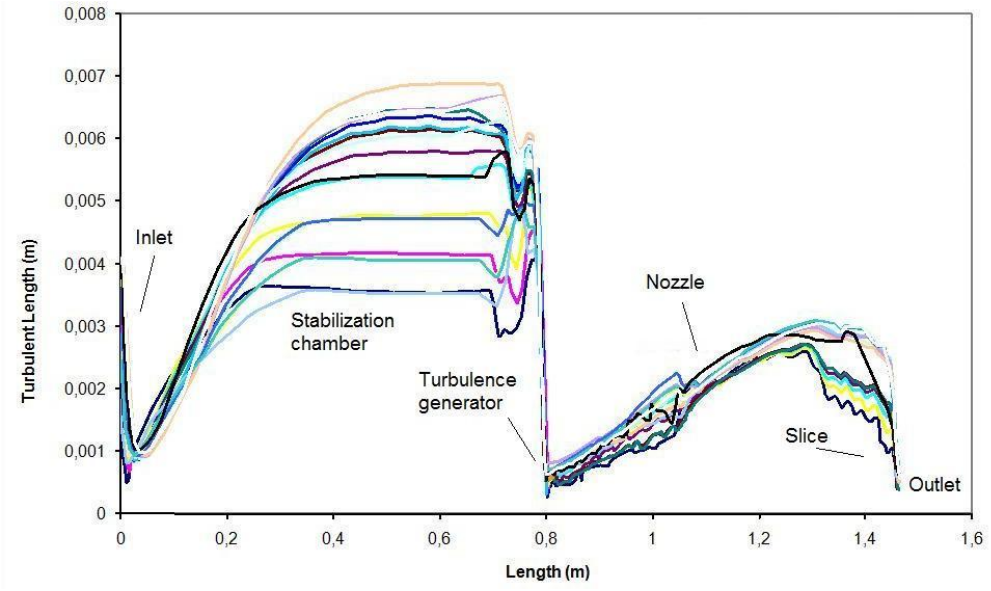

Figure 2.63: Turbulence length inside the third headbox configuration (50 traces)

The fourth model studied consists of the same geometrical configuration of the turbulence generator section and nozzle section as the second model described before. In this model this stabilisation chamber length was reduced to the half of the size (see figure 2.64). This kind of solution could be very interesting for the paper mills that want to evolve to this kind of headbox but are limited in space. The results of this model are quite interesting because even that the stabilisation chamber was reduced to its half, the results are quite the same as the previous model, showing us that another geometrical structure is possible if the flowing conditions are kept.

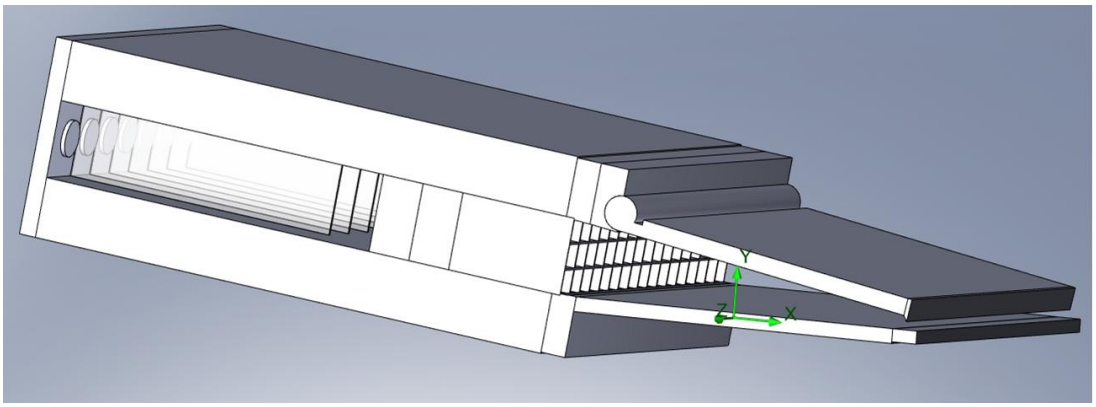

Figure 2.64: Fourth headbox configuration

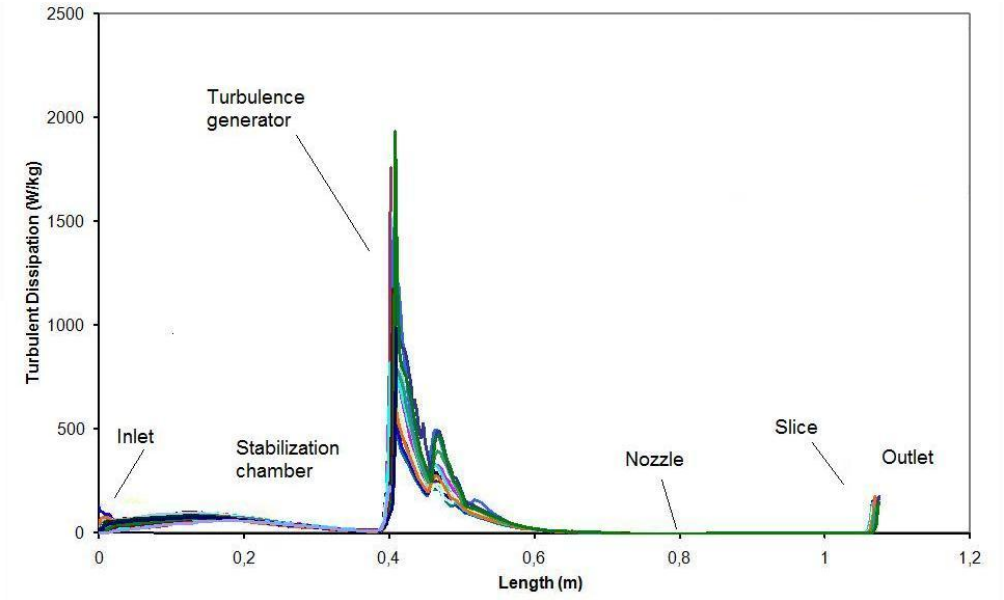

Figure 2.65: Turbulence dissipation inside the fourth headbox configuration (50 traces)

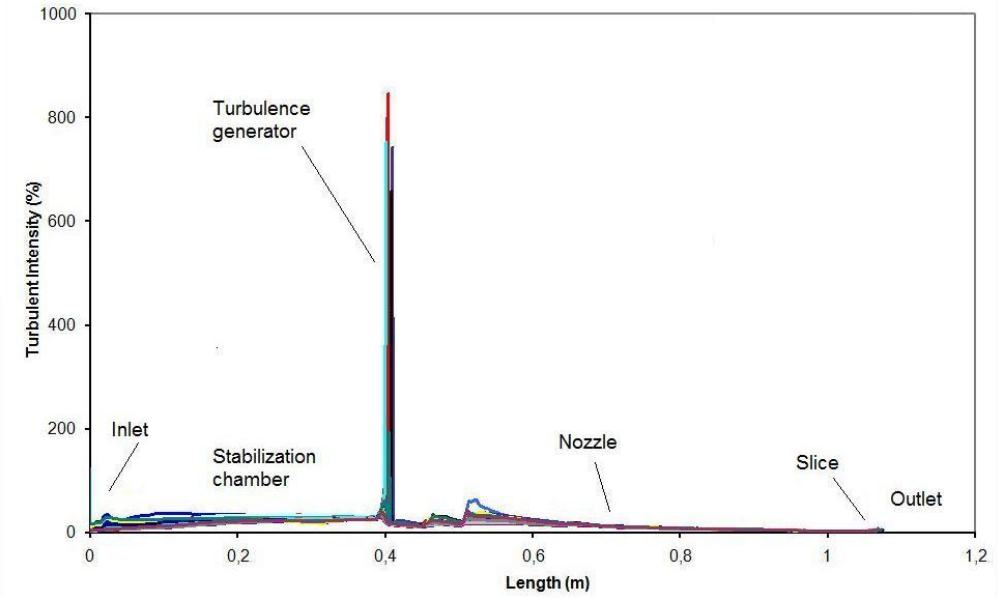

Figure 2.66: Turbulence intensity inside the fourth headbox configuration (50 traces)

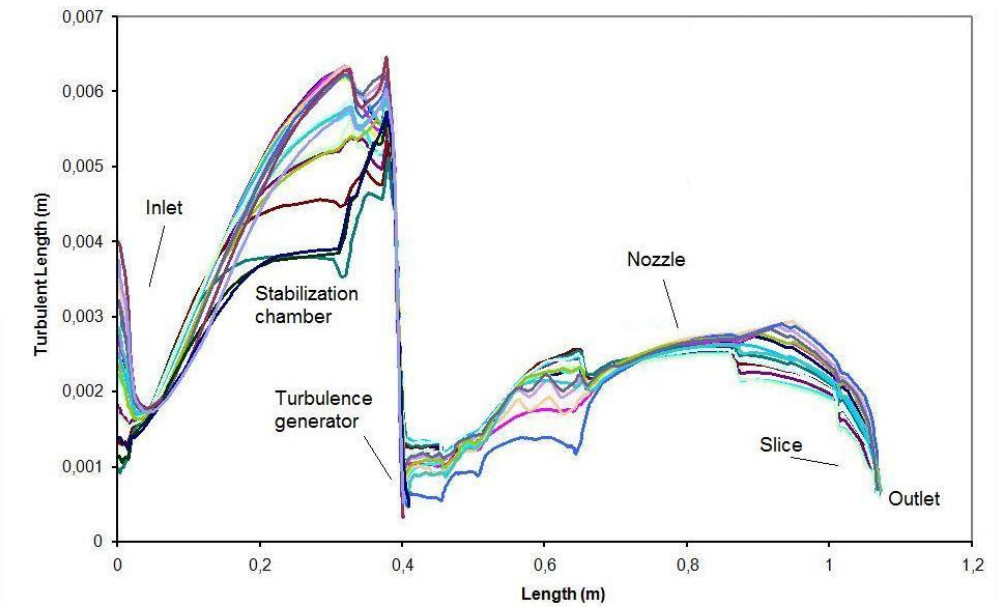

Figure 2.67: Turbulence length inside the fourth headbox configuration (50 traces)

The last model studied in this section consists of the same geometrical structure as the model before but this time the nozzle was optimised with the use of vanes as proposed in section 2.4. Vanes were tested in industrial papermaking conditions and they give a better result in terms of deflocculation. This could be confirmed by the length of turbulence found at the nozzle section. We can see in figure 2.71 that there is a notable reduction of turbulence length by the use of these lames and a very small turbulence length is achieved at the slice.

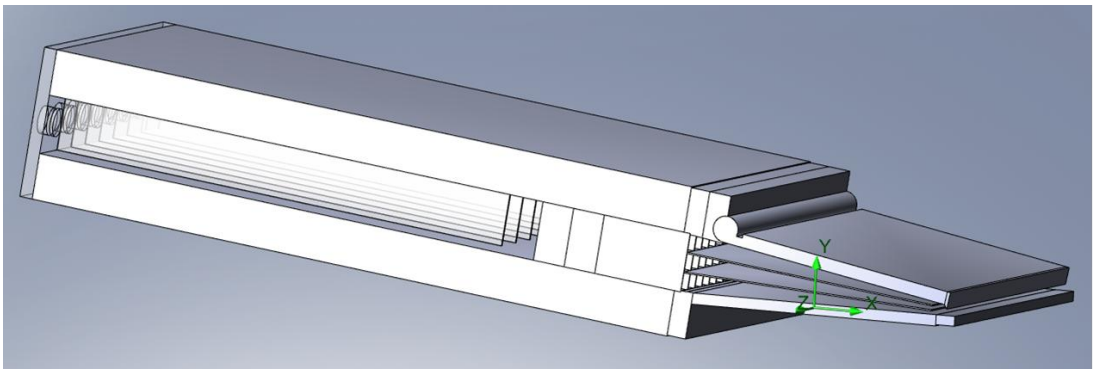

Figure 2.68: Fifth headbox configuration

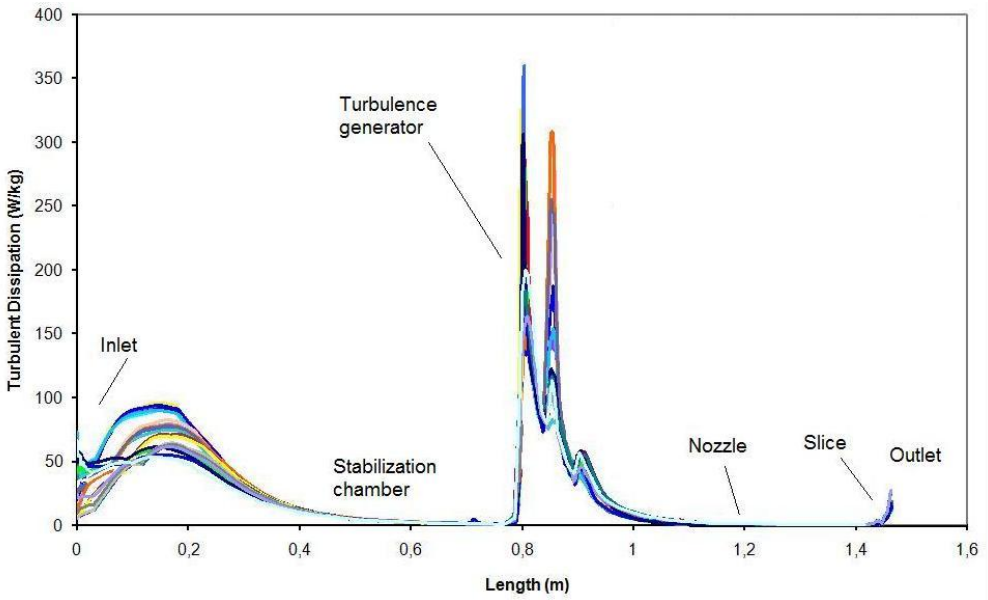

Figure 2.69: Turbulence dissipation inside the fifth headbox configuration (50 traces)

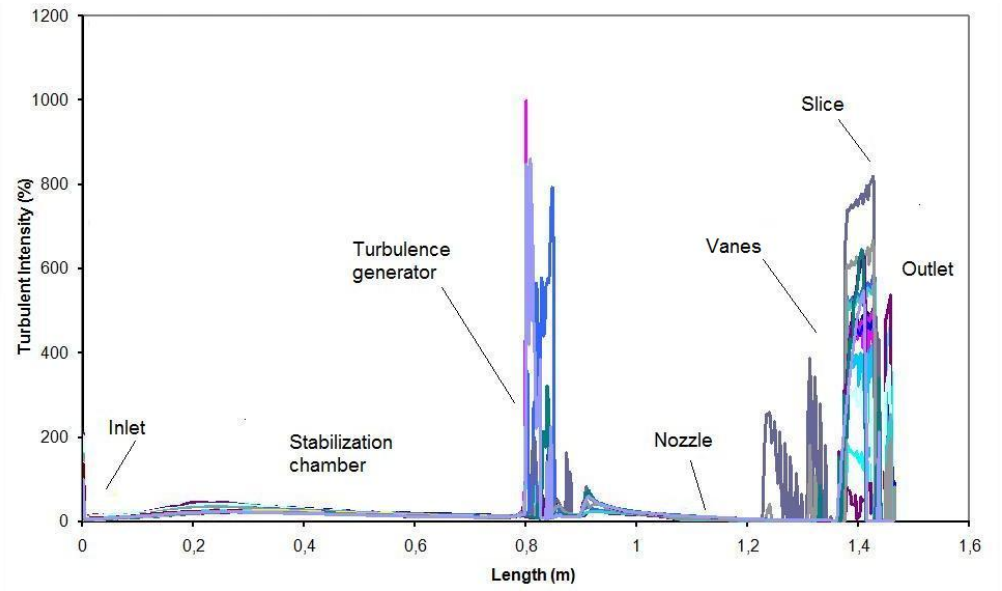

Figure 2.70: Turbulence intensity inside the fifth headbox configuration (50 traces)

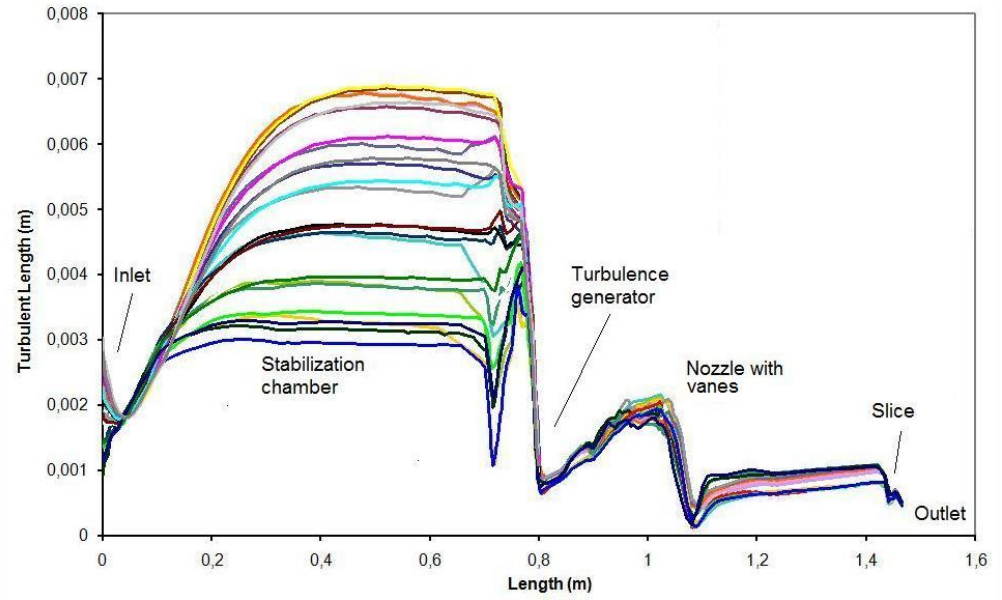

Figure 2.71: Turbulence length inside the fifth headbox configuration (50 traces)

2.6 Conclusion of this chapter

In this chapter, each part inside a headbox was analysed and experiments were performed on specific test benches in order to analyse the phenomena taking place.

Several orifice plate geometries were studied. It was seen that a certain deflocculating effect is got but at high energy rates. This amount of energy is related to the small constriction that has to be imposed at the inlet of the tube bank. It was shown also that to optimise this constriction, its size should be related to the type of pulp passing through it. In other words if the pulp passing through the constriction is a softwood pulp then the constriction should be smaller (energy applied higher) than if it is a hardwood pulp where the constriction could be a larger. Considering the high energy rates and the risk to block out the entire headbox, these optimised constrictions can not be kept in industrial conditions, however it can be interesting to try a movable constriction of the tube bank related to the consistency of the pulp and the length of fibres used. For the normal tube bank geometries, especially the geometries used nowadays in the papermaking industry, no notable deflocculating process was seen. Nevertheless, industrial testimonies described a better paper formation by the use of this type of geometry. Several theories were proposed to try to describe this phenomenon, unfortunately no experimental method was found to validate these theories. We believe that most of the energy applied at the tube bank is wasted in the fluid medium and not applied at the deflocculating process. If this is true, it will mean that a certain slip exists between the fibres and the fluid, even though the fibres represent only a little amount of volume inside the fluid. This could be essential for the total understanding of the deflocculating process because it would mean that the same amount of energy applied by the tube bank should be applied by other ways (ultrasound by instance) directly to the fibres and not into the fluid if we want to optimise this process.

The Coanda effect was found at the inlet of the stabilisation chamber in the pilot used. This disturbing effect should be minimised by a streamlined inlet at the headbox. This is important firstly because if a proper, homogeneous pulp distribution is already achieved at the stabilisation chamber, then the headbox can be optimised and, secondly, because any disturbance found inside the headbox can interfere to the whole functioning of the headbox.

It was also shown that the geometrical configuration of a tube bank is closely related to some disturbances found downstream at the sheet formation. These disturbances can be minimised if a streamlined profile is respected for the design of the turbulence generator and a staggered placing method is used to avoid secondary flows.

The nozzle itself, even though it does not represent a main parameter at the headbox design for many people, should be reconsidered. Comparing to other researches made for mining industry it was shown that for obtaining a more coherent jet some geometrical rules should be applied to the nozzle design. We noticed that these recommendations are not respected in the pilot used in this present work. It might be interesting to revisit these design parameters to obtain an optimised jet. From the CFD simulations made inside the headbox, no noticeable effect could be seen to conclude that these parameters are the best ones for the papermaking industry. Nevertheless, a CFD model can not replace a real experimental setup where the evolution of the jet can be observed and compared to other geometries. It could be very interesting to see if these geometrical nozzle parameters can be optimised to get a better jet, without secondary flows and breaks up.

From a deflocculating point of view, some big structures reformed at the nozzle and then stretched at the lips were observed. No deflocculating process was seen at this point. This is quite logical because inside the nozzle turbulence decays. It can be said now, that the scale and intensity of turbulence should be kept inside this nozzle. This justified the use of vanes inside the nozzle that will keep as long as possible the turbulence intensity and scale over the nozzle. Several works treated this subject and much literature can be found in the optimisation parameters of these vanes.

From all these remarks, it can be seen that the design of an optimised headbox is possible but the quality and the shape of the jet flowing out of the headbox is unknown. A prediction of the jet shape for a better positioning of the headbox in the paper mill is not made and a predefinition of the headbox capacity (range of jet speed, angle, etc) is completely unknown for the papermaker. Considering this, we will try in the next section to predict the jet shape using the geometry configuration of the headbox to get this whole information.

Chapter 3

Study of the Jet control

The control of the jet exiting a headbox is extremely important in modern papermaking operation. Indeed the quality of paper is dependent on the flow velocity of the pulp as well as the angle of the jet at the impact point by means of the fibre orientation inside a paper sheet. The control of these parameters is quite delicate and needs most of the time a trial/error operation that causes a waste of time and money in modern productions. Nowadays, the actual method to control these parameters uses the Bernoulli equation (or an approximation by means of the Torricelli equation) to give the jet speed and the contraction ratio of this jet. The angle of the jet can be approximated using a simple ballistic equation. However, these methods do not give the total information needed for a better control because it is almost impossible to determine the total shape of the jet and the exact angle at the impact point. In the following sections we are going to describe different mathematical models used to predict the total shape of the jet considering the geometry of the nozzle only. We are going to determine as well the limitations and the uses of each one of these models.

3.1 Classical control method

The classical way to measure the speed of the jet at the slice of the headbox is to measure the hydraulic height at the headbox. This way of control comes from the times when only open headboxes could be found at the paper mills and the use of the Torricelli's law was justified. The Torricelli's law states that the speed of a fluid flowing out of an opening under the force of gravity is proportional to the square root of the product of twice the acceleration of the gravity multiplied by the height h, the distance between the level of the surface and the positioning of the vena contracta. This law must agree with several working hypothesis:

- The hole diameter must be small enough to be neglected compared to the height of flow.

- The free surface must be much bigger than the jet surface, in other words the height between the level of the surface and the jet does not depend of time.
- Any point A at the surface could be linked to any point B at the jet by means of a streamline.

If gravity is constant for the whole recipient, then the Bernoulli equation can be used

$$p_{\mathrm{A}} + \rho g h_{\mathrm{A}} + \frac{1}{2}\rho v_{\mathrm{A}}^2 = p_{\mathrm{B}} + \rho g h_{\mathrm{B}} + \frac{1}{2}\rho v_{\mathrm{B}}^2 \tag{3.1}$$

where P is the static pressure at point A and B; h is the height between these points; v is the flow speed; ρ is the fluid density and g is the gravitational constant.

It is known that the pressure at the vena contracta equals the surface pressure, i.e. the atmospheric pressure. Moreover the flow speed at A can be neglected, then the speed in the point B can be calculated using

$$v_{\mathrm{B}} = \sqrt{2gH} \tag{3.2}$$

Where $H = h_A - h_B$

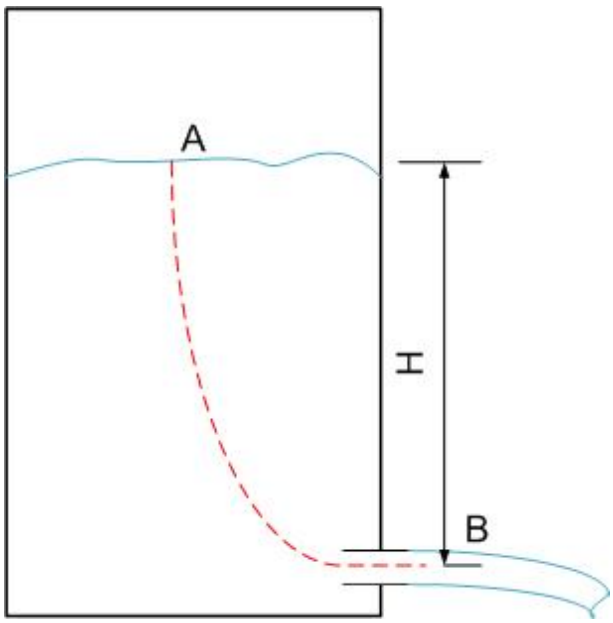

Figure 3.1: Torricelli's law

For an open headbox this method can be applied easily. However can this formula be applied to a hydraulic headbox without loosing sense? In modern industrial applications (hydraulic headboxes) a pressure sensor is placed at the beginning of the nozzle. This static pressure is then converted in the equivalent height of water gauge and then introduced in equation 3.2. An advantage of this kind of calculation is its ease of application. Furthermore, knowing the flow rate passing through the headbox, an estimation of the contraction coefficient can be made. By definition a flow rate Q is the flow speed V times

the passing surface S. From this definition the flow speed can be expressed as the ratio between the flow rate and the section, as shown in equation 3.3.

$$V = \frac{Q}{S} \tag{3.3}$$

If V is determined by means of the Torricelli's law, Q was measured, then the passing surface at the vena contracta S_{vc} can be calculated. The ratio between this passing surface at the vena contracta and the slice opening surface S_{slice} is, by definition, the contraction coefficient Cc commonly used in papermaking applications as shown in equation 3.4

$$Cc = \frac{S_{vc}}{S_{slice}} \tag{3.4}$$

Unfortunately, this method takes into account only the static pressure measured at the wall of the nozzle and not the total pressure. No measuring method can be applied to measure the dynamic pressure at a fibrous suspension without perturbing the whole installation.

3.2 Other control methods

3.2.1 Ideal fluid models

During decades, ideal fluid models were used to give an answer to complex situations. Nowadays these kinds of calculations are still used because of their simplicity and the accurate values got. When we talk of ideal fluids in this work, we refer to the Euler's definition for incompressible, non-viscous flow as described in the partial differential equation 3.5:

$$\rho \left\{ \frac{\partial u_i}{\partial t} + \sum_{k=1}^{3} u_k \frac{\partial u_i}{\partial x_k} \right\} = -\frac{\partial p}{\partial x_i} + \rho g_i \tag{3.5}$$

where u is the local flow velocity; p is the static pressure; ρ is the density and g is the gravitational constant. This equation can only be satisfied by an irrotational, volume conserving flow as described in equation 3.6:

$$\begin{cases} u = \nabla U \\ \nabla^2 U = \sum_{i=1}^{3} \frac{\partial u_i}{\partial x_i} = \sum_{i=1}^{3} \frac{\partial^2 U}{\partial x_i^2} = 0 \end{cases} \tag{3.6}$$

In this first section, we will analyse ideal plane flows from funnels. The general method used in this work can be summarised from Birkhoff and Zarantonello [61] as follows: In plane flows, the fluid particle position in the physical plane can be represented by a single

complex coordinate $z = x + iy$. The complex conjugate of the vector velocity is denoted as $\zeta = \xi + i\eta$ so that $\xi = u_1$ and $\eta = -u_2$.
If the complex potential W is defined as $\varphi + i\psi$ where φ is the velocity potential and ψ is the stream function, then $W(z)$ is a complex analytic function where $dW/dz = \zeta$ so $z = \int \zeta^{-1} dW$ and the boundaries conditions reduced to:

$$\begin{cases} \psi = \text{constant on the fixed boundaries} \\ |\zeta| = \text{constant on the free boundaries} \end{cases} \tag{3.7}$$

In some cases, especially polygonal ones, ideal plane flow satisfying the last equations can be found by conformal mapping.

Attwood's model expansion

It was explicitly shown by Attwood [62] that the total jet shape can be calculated using a potential flow by means of a conformal mapping in the case when the nozzle is like the one described at figure 3.2. In this figure we can see that for this case the nozzle is considered coming from the infinite with an angle equal to $\theta = \pi/n$, and with an opening equal to b. The method proposed by Attwood is a special case of the complex potential (equation 3.8) of the flow of a free jet proposed by Birkhoff and Zarantonello [61] when the convergent angle is equal to π/n, with n integer. The position of each fluid particle inside the jet can be obtained by equation 3.9 where the real and imaginary parts of z represent the x and y coordinates of each fluid particle respectively. This last equation is valid at any location in the jet.

$$W = n \cdot \ln(\zeta) - \ln\left(\zeta^n - e^{in\alpha}\right) - \ln\left(\zeta^n - e^{-in\alpha}\right) \tag{3.8}$$

$$z = -\frac{n}{\zeta} - \sum_{k=0}^{n-1} e^{-i\left(\frac{2\pi k}{n}+\alpha\right)} \ln\left[\zeta - e^{i\left(\frac{2\pi}{n}+\alpha\right)}\right] - \sum_{k=0}^{n-1} e^{-i\left(\frac{2\pi k}{n}-\alpha\right)} \ln\left[\zeta - e^{-i\left(\frac{2\pi}{n}+\alpha\right)}\right] \tag{3.9}$$

Considering the hardware limitations during the sixties, only some typical angles of incidence corresponding to $\theta = \pi/n$ with integer values of n were considered. Only these angles can be solved analytically.

This analytically solution is possible due to the huge simplification of the complex integrals to be solved. Using modern computational tools, a numerical solution of these complex integrals can be obtained and therefore every angle of incidence can be calculated. Our mathematical development starts also from the complex potential proposed by Birkhoff and Zarantonello (equation 3.8). It can be demonstrated that equation 3.8 can be also be written as equation 3.10 or in an even simplest way as shown in equation 3.11.

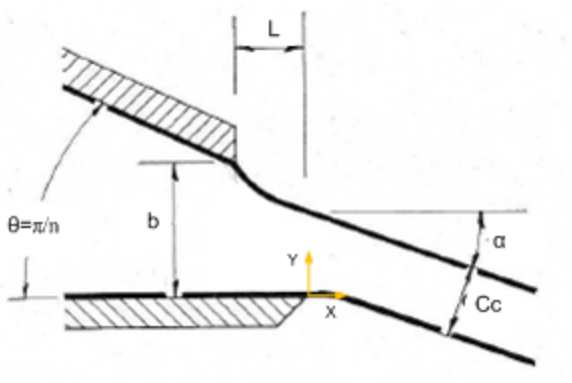

Figure 3.2: Nozzle description by Attwood [62]

$$W = \ln\left(\frac{\zeta^n}{(\zeta^n - e^{in\alpha})\,(\zeta^n - e^{-in\alpha})}\right) \tag{3.10}$$

$$W = \ln\left(\frac{\zeta^n}{\zeta^{2n} - 2\cos(n\alpha)\,\zeta^n + 1}\right) \tag{3.11}$$

It can be shown that at the boundaries of the free jet we have $|\zeta| = 1$. This will lead us to describe the potential flow for the upper and lower streamlines of the jet as it is shown in equations 3.12 and 3.13 respectively.

$$W = -\ln(2) - \ln(\cos(n\varphi) - \cos(n\alpha)) \qquad (0 \leq \varphi < \alpha) \tag{3.12}$$

$$W = -\ln(2) - \ln(\cos(n\alpha) - \cos(n\varphi)) + i\pi \qquad (0 \leq \varphi < \alpha) \tag{3.13}$$

It can be also shown that:

$$\frac{dz}{d\varphi} = \frac{dW}{d\varphi} \cdot \frac{1}{\zeta} \tag{3.14}$$

This last equation allows us to plot the equipotential lines between the two boundary lines inside the jet. Equations 3.12 and 3.13 become equation 3.15 for the upper boundary and equation 3.16 for the lower boundary.

$$\frac{dz}{d\varphi} = \frac{n \cdot \sin(n\varphi) \cdot e^{-i\varphi}}{\cos(n\varphi)} \tag{3.15}$$

$$\frac{dz}{d\varphi} = \frac{n \cdot \sin(n\varphi) \cdot e^{-i\varphi}}{\cos(n\varphi) - \cos(n\alpha)} \tag{3.16}$$

When n is neither an integer value nor a rational fraction, the lower and the upper streamline profiles can only be calculated thanks to a numerical resolution of these equations. In this present work the Euler method for numerical integration was used.

Incomplete Beta function model

Mathematically, any convergent angle can be obtained by the use of a rational fraction $n = r/s$ where r and s are integers, and r is greater than s. So equation 3.9 can be expressed as:

$$z = I_n\left(\zeta, e^{i\alpha}\right) + I_n\left(\zeta, e^{-i\alpha}\right) - I_n\left(\zeta, v\right) - I_n\left(\zeta, v^{-1}\right) \tag{3.17}$$

where v is the velocity in the nozzle i.e. $v < 1$. Each complex function I_n can be expressed as a function of r and s in the following way:

$$I_{r/s}\left(\zeta, \zeta_1\right) = r\int_0^{\zeta} \frac{u^{r-s-1}}{u^r - u_1^r} du \tag{3.18}$$

where $u = \zeta^{1/s} = t^{1/r}$

Since r is greater than s then the integrand is finite at u equals 0. Then z can be expressed in terms of elementary complex functions. Each complex function I_n can also be written as an incomplete beta function as described in equation 3.19:

$$B_\beta\left(\tau\right) = B\left(\beta, 0; \tau\right) = \int_0^{\tau} \tau^{\beta-1}\left(1-\tau\right)^{-1} d\tau \tag{3.19}$$

with $\beta = \left(n-1\right)/n$.

Indeed each complex integral becomes

$$I_n\left(\zeta, \zeta_1\right) = -\zeta_1^{-1} B_\beta\left(\zeta^n/\zeta_1^n\right) \tag{3.20}$$

The advantage of using this function is the unified scheme for resolving this complex functions. This method allows us to get a precise result in only few seconds. The source of error due to the iterative method is minimised.

In the same way as before, if $n = r/s$ is rational with integer values of r and s then the incomplete beta function becomes $B_\beta(\tau) = B(1 - \frac{r}{s}, 0; \tau)$ and the complex functions I_n can be expressed in terms of elementary functions:

$$z = \frac{-(e^{i\alpha} - e^{i\alpha}) \cdot v \cdot B_\beta(e^{-in\alpha} \cdot \zeta^n) + B_\beta(v^{-n} \cdot \zeta^n) + v^2 B_\beta(v^n \cdot \zeta^n)}{v} \tag{3.21}$$

Appel's model

Appel and Yu from the University of Kansas showed the importance of the contraction ratio of the nozzle to the jet shape calculation [63]. They assigned that most of the real jets come from an approach duct that delivers the flow in a nozzle and not from an infinite reservoir as in the previous model, using the transformation proposed by Siao and Hubbard which was described in McNown's work [64]. In which the coordinates of any

particle inside the streamlines is given by the integration of equation 3.22. Appel and Yu have found a relationship between the jet shape and the contraction ratio.

$$z = \frac{c}{\pi} \sum_{r=0}^{m-1} \int f(\tau) d\tau \tag{3.22}$$

with

$$f(\tau) = \left[-\frac{c^{-1} e^{-2ir\alpha}}{\tau - c^{1/n} e^{2ir\alpha/n}} - \frac{c\, e^{-2ir\alpha}}{\tau - c^{-1/n} e^{2ir\alpha/n}} + \frac{e^{-i(2r\alpha+\beta)}}{\tau - e^{i(2r\alpha+\beta)/n}} + \frac{e^{-i(2r\alpha-\beta)}}{\tau - e^{i(2r\alpha-\beta)/n}} \right]$$

where β is the final jet angle and c is the relative jet thickness d/h. This relationship is restricted to nozzle angles of rational fractions of π, with r and s integers and $r > s$. The $\zeta' - plane$ and the $t - plane$ for this problem are shown in figure 3.3.

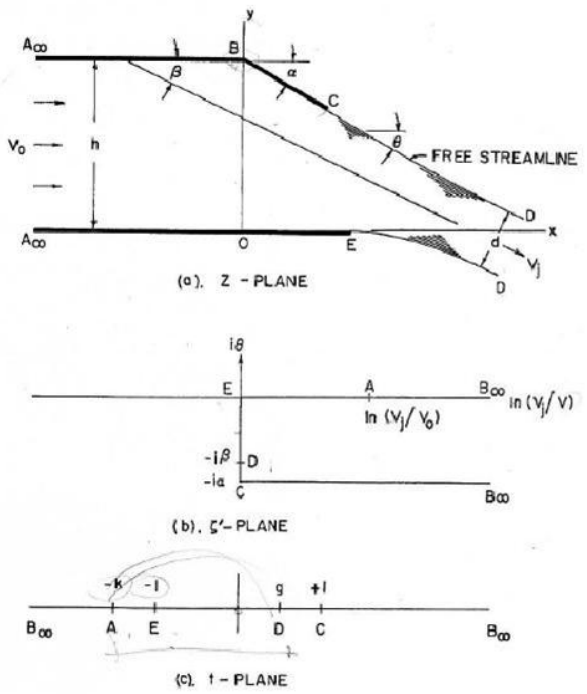

Figure 3.3: Transformation planes used by Appel and Yu

With the hardware limitations of the early sixties, only some nozzle angles (like 90°, 45° and angles smaller than 10°) could be solved. The reason of this choice is that the sum of integrals could be reduced to a simpler expression for these angles. These nozzle angles are the origin of the TAPPI Technical information Sheets, [59] and [60].

The Schwarz-Christoffel's equation

Analysing in detail the method used by Appel and Yu, it comes out that a Schwarz-Christoffel transformation was used. The principal objective of a Schwarz-Christoffel

mapping is the transformation of the complex plane that maps the upper half-plane conformally to a polygon. The Schwarz-Christoffel formula is defined as:

Definition Let P be the interior of a polygon Γ in the W plane, having vertices w_1, w_2, ..., w_n and interior angles $\alpha_1, \alpha_2, \ldots, \alpha_n$, where $-\pi < \alpha_k < \pi$ in counterclockwise order. There exists a one-to-one conformal mapping $w = f(z)$ from the upper half-plane H^+ onto P that satisfies the boundary conditions: $w_k = f(x_k)$ for $k = 1, 2, \ldots, n-1$ and $f(\infty) = w_n$ where $x_1 < x_2 < \ldots < x_{n-1} < \infty$

The derivative $f'(z)$ is expressed as follows:

$$f'(z) = A(z - x_1)^{-\alpha_1/\pi}(z - x_2)^{-\alpha_1/\pi}...(z - x_{n-1})^{-\alpha_{n-1}/\pi} \tag{3.23}$$

So the Schwarz-Christoffel formula can be expressed as an indefinite integral:

$$f(z) = B + A \int (z - x_1)^{-\alpha_1/\pi}(z - x_2)^{-\alpha_2/\pi}...(z - x_{n-1})^{-\alpha_{n-1}/\pi} dz \tag{3.24}$$

where A and B are suitably chosen constants. Two of the points x_k may be chosen arbitrarily. The constants A and B determine the size and position of P.

The method proposed by Dias, Elcraft and Trefethen.

Mathematically, even if the classical jet theory is elegant, it has major limitations. Only few simple geometries can be treated in a closed form. The reason is that the solution is related to the conformal mapping of Schwarz-Christoffel type that is impossible to determine analytically unless the nozzle contains two or three corners only. Dias, Elcrat and Trefethen [65] solved this limitation for computing two dimensional ideal jets from any arbitrary polygonal container. This method is based on numerical procedures developed for solving the Schwarz-Christoffel transformation with a modified Schwarz-Christoffel integral for the free streamlines. This modified integral is necessary because the free streamlines are not straight lines. The formulation of the problem can be summarised from the work by Dias, Elcrat and Trefethen [65] as follows: An ideal incompressible fluid in the complex z-plane flows out of a nozzle bounded by two walls extending to infinity as shown in figure 3.4.

The upper wall consists of a finite number of straight line segments delimited by finite vertices $z_1, \ldots, z_{L-1}$ and the infinite vertex $z_L = \infty$. The segment (z_k, z_{k+1}) is denoted by Γ_k. Similarly, the lower wall is denoted by z_L and by finite vertices $z_{L+1}, \ldots, z_n$. The indices are ordered so that the flow region lies to the left as one traverses the boundary in the direction $z_1, \ldots, z_L, \ldots, z_n$. From a fluid dynamics point of view, the problem is

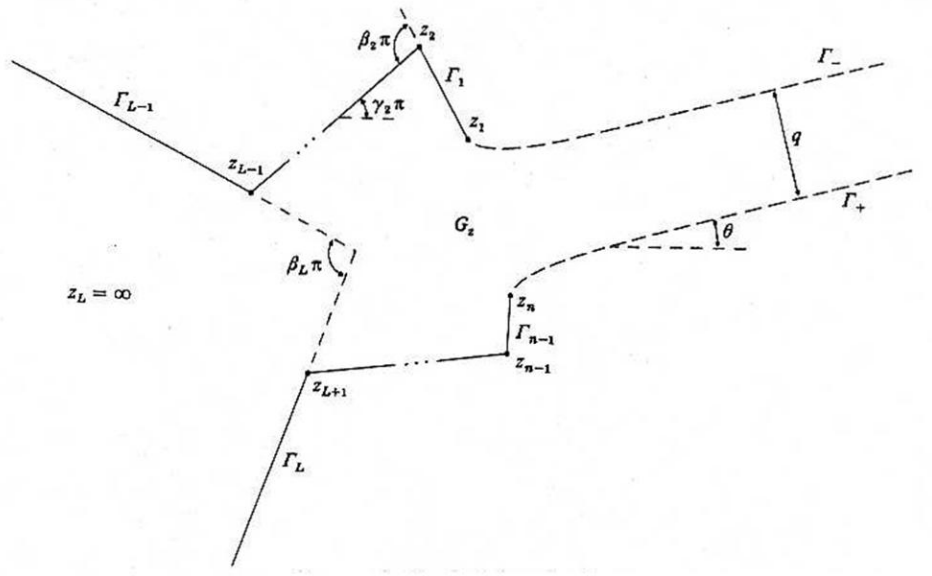

Figure 3.4: Physical domain by Dias *et al.*

to determine a potential flow $v(z)$ through the nozzle that continues to $z = \infty$ as a jet bounded by two free streamlines Γ_- and Γ_+ on which the speed of flow is constant.

$$|v(z)| = 1 \; for \; z \in \Gamma_\pm \tag{3.25}$$

The solution comes from the Bernoulli's equation: a jet will have constant pressure p equal to ambient pressure on its bounding streamlines, and in the absence of gravity, this implies that the velocity of the flow, $|v|$, is constant there. Three physical quantities are to be determined in the solution: the shape of the free streamlines, the angle θ of the jet at infinity, and q the discharge rate. Because of the normalization given by equation 3.25 the discharge rate q is equal to the width of the jet at infinity. This flow problem can be reduced to a problem in complex analysis as follows: Since the flow in G_z is irrotational and incompressible, $v(z)$ is the gradient of a real velocity potential $\phi(z)$ defined in G_z that satisfies $\nabla^2\phi = 0$. Let $v(z)$ be thought of as a complex scalar, and let ζ be its complex conjugate, the hodograph variable,

$$\zeta(z) = \overline{v}(z) \tag{3.26}$$

Then ζ is the complex derivative of a complex velocity potential $w(z) = \phi(z) + i\psi(z)$, similar to the previous cases.

$$\zeta(z)\frac{dw(z)}{dz} \tag{3.27}$$

where the stream function ψ is the harmonic conjugate of ϕ. The function $w(z)$ is analytic in G_z, and maps G_z conformally onto an infinite strip G_w of height q as shown in figure 3.5.

Without loss of generality we shall fix $w_n = 0$. The point w_1 then lies at a location to be determined on the line $\Im w = q$.

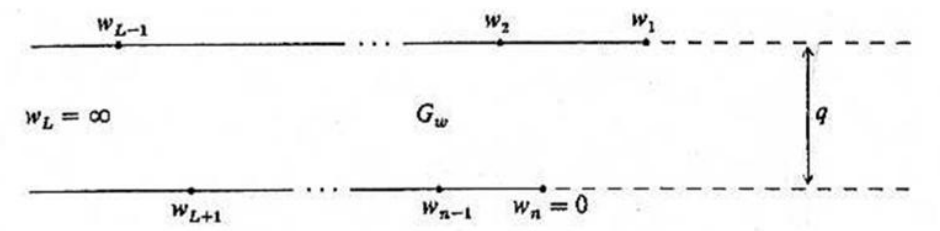

Figure 3.5: Velocity-potential domain by Dias *et al.*

It will be convenient to reduce G_w to the upper half of the unit disk (as shown in figure 3.6, with w_1 and w_n corresponding to the points -1 and 1, respectively.

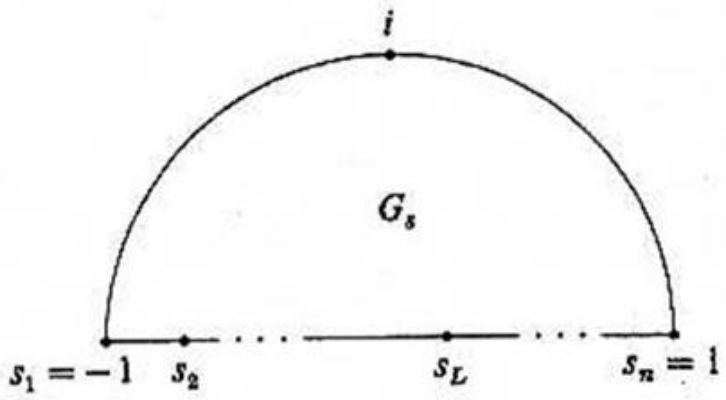

Figure 3.6: Computational domain by Dias *et al.*

The following mapping was used between the infinite strip and the half-disk.

$$w = \frac{q}{\pi} \log \left(\frac{\frac{2s}{(1+s^2)} - \frac{2s_L}{(1+s^2)}}{1 - \frac{2s_L}{(1+s^2)}} \right) \tag{3.28}$$

$$s = \frac{1 - \left(1 - \left(e^{\frac{\pi w}{q}} (1 - \sigma_L) + \sigma_L\right)^2\right)^{\frac{1}{2}}}{e^{\frac{\pi w}{q}} (1 - \sigma_L) + \sigma_L} \tag{3.29}$$

The restatement of the jet problem as a problem of complex analysis goes as follows: The goal now is to find a complex analytic function $z(s)$ in G_s that satisfies the following conditions:

$$\arg \frac{dz}{dw} = \gamma_{n-1}\pi \qquad at\, s = s_n\,, \tag{3.30}$$

$$\Delta \arg \frac{dz}{dw} = \beta_k \pi \qquad at\, s = s_k,\ 2 \leq k \leq n-1, \tag{3.31}$$

$$\left|\frac{dz}{dw}\right| = 1 \qquad for\ |s| = 1,\ \Im s \geq 0, \tag{3.32}$$

$$|z(s_{k+1}) - z(s_k)| = |z_{k+1} - z_k|\,, \quad 1 \leq k \leq L-2,\ \ L+1 \leq k \leq n-1, \tag{3.33}$$

$$z(s_1) - (s_n) = z_1 = z_n \tag{3.34}$$

The classical approach to determining $z(s)$ is to make use of the hodograph domain G_ψ, which is the region in the ψ-plane corresponding to G_z. G_ψ is bounded by radial lines and circular arcs, which become horizontal and vertical lines under a complex logarithm. Therefore, a disk or a half plane can be mapped onto $log\,(G_\psi)$ by a Schwarz-Christoffel transformation. However, except for the simplest nozzle geometries, $log\,(G_\psi)$ turns out to be not a planar polygon but a polygonal Riemann surface, with a boundary topology that is not fully determined a priori, and the required Schwarz-Christoffel map is of a generalised kind whose determination is not straightforward. To get around all these problems Dias proposed a modified Schwarz-Christoffel formula defined by

$$h_k(s) = \left(\frac{s - s_k}{1 - s_k s}\right)^{-\beta k} \tag{3.35}$$

with the branch chosen so that $h_k(s) > 0$ for $s \in (s_k, 1)$. Then h_k maps G_s onto a pie slice (if $\beta_k < 0$) or the complement of a pie slice (if $\beta_k > 0$), as shown in figure 3.7.

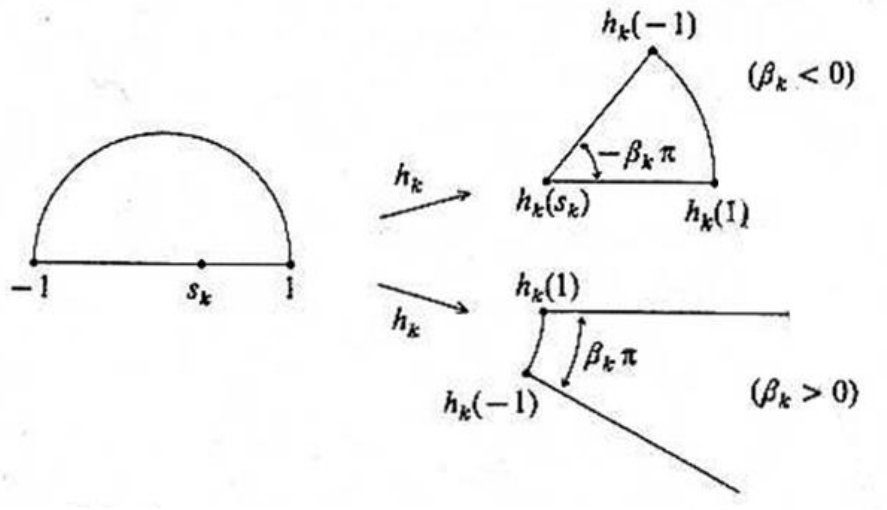

Figure 3.7: The factor h_k in the modified Schwarz-Christoffel integral [65]

For an explicit representation of the function d_z/d_w we can simply take a product of factors h_k and then we get:

$$\frac{dz}{dw} = e^{i\gamma_{n-1}\pi} \prod_{k=2}^{n-1} \left(\frac{s - s_k}{1 - s_k s} \right)^{-\beta_k} \tag{3.36}$$

This formula satisfies the argument conditions (3.30 and 3.31) and it satisfies the magnitude condition (3.32) too, since each factor satisfies it individually. The integration gives a modified Schwarz-Christoffel formula for the map from G_s to G_z.

$$z(s_b) - z(s_a) = e^{i\gamma_{n-1}\pi} \int_{w_a}^{w_b} \prod_{k=2}^{n-1} \left(\frac{s - s_k}{1 - s_k s} \right)^{-\beta_k} dw \tag{3.37}$$

It is more useful for this formula to integrate with respect to s rather than w. Thanks to equations 3.28 and 3.29, dw can be replaced by:

$$dw = \frac{dw}{ds} ds = \frac{q}{\pi} \frac{(1 + s_L^2)(1 - s^2)}{(1 - s^2)(s - s_L)(1 - s_L^2)} ds \tag{3.38}$$

and the integral becomes:

$$z(s_b) - z(s_a) =$$

$$\frac{q}{\pi} (1 + s_L^2) e^{i\gamma_{n-1}\pi} \int_{s_a}^{s_b} \frac{1 - s^2}{(1 + s^2)(s - s_L)(1 - s_L s)} \prod_{k=2}^{n-1} \left(\frac{s - s_k}{1 - s_k s} \right)^{-\beta_k} ds \tag{3.39}$$

This completes the mathematical formulation of the jet problem proposed by Dias. The geometric conditions (equations 3.33, 3.34) can be accomplished by adjusting q and $s_2, \ldots, s_{n-1}$ by numerical procedures.

Application to a headbox geometry.

We have applied this method to the same geometry proposed by Appel with the distribution of nodes chosen as shown in figure 3.8. For the case of a real headbox nozzle geometry, it was said above that the fact that the fluid passes through a double convergent section (nozzle convergent and slice) can change the jet shape. The geometry tested with the corresponding nodes is shown in figure 3.9.

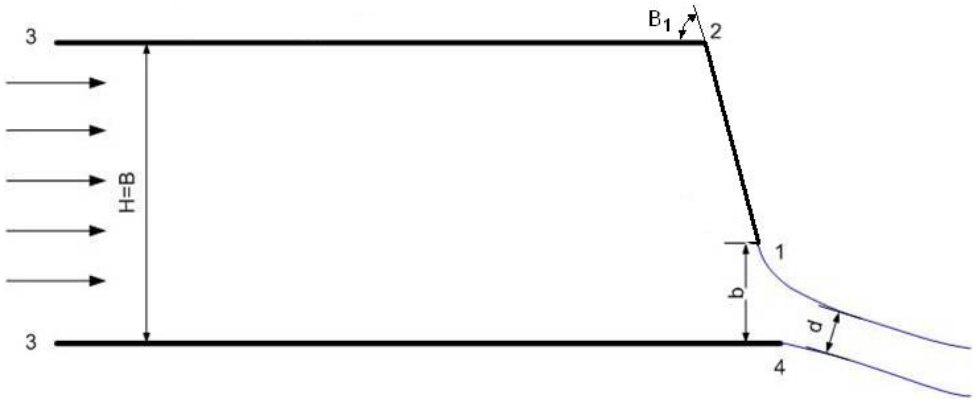

Figure 3.8: Single convergent nozzle geometry

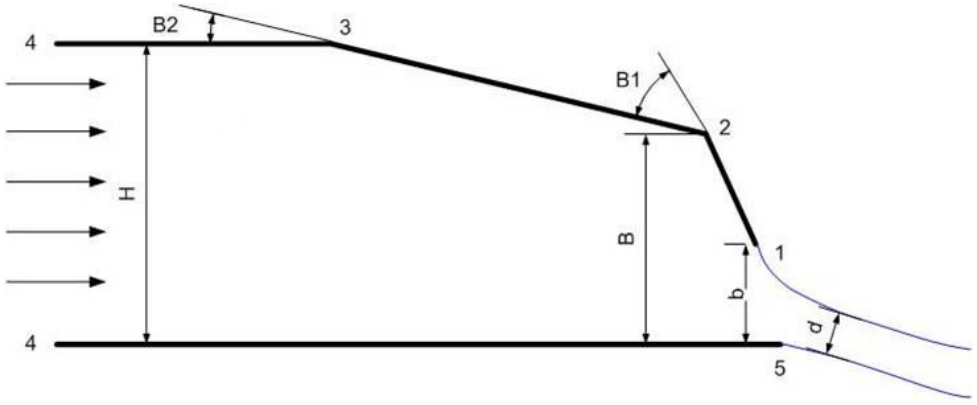

Figure 3.9: Double convergent nozzle geometry

3.2.2 Location of the vena contracta

Two criteria were used to assess the position of the vena contracta inside the jet. This information would be of high importance for the papermaker because the whole papermaking operation, fabrics/jet speed ratio, fibre orientation and exact location of the jet impact depends on this value. The first criterion taken into account was the cord over the arc length ratio. This ratio compares the value of the cord length to the arc length (the arc corresponding to the equipotential curves) at a certain location of the jet.

When this ratio is closer to unity, then it can be said that the velocity vectors become all parallel and the pressure in the whole section of the jet equals the atmospheric pressure. The threshold value chosen in this work is ratio < 1.00001.

The second criterion is similar to the previous one, but this time the ratio was normalised by π, this was done to eliminate any possible scale error of the conformal mapping. The threshold was chosen to be inferior to 0.0001. Some results obtained are shown in figures 3.10. It is interesting to see that the vena contracta is always inside the lower lip extension. In other words the impact to the fabrics could be fixed just before the lower lip ending. So there is no need of a long free-jet.

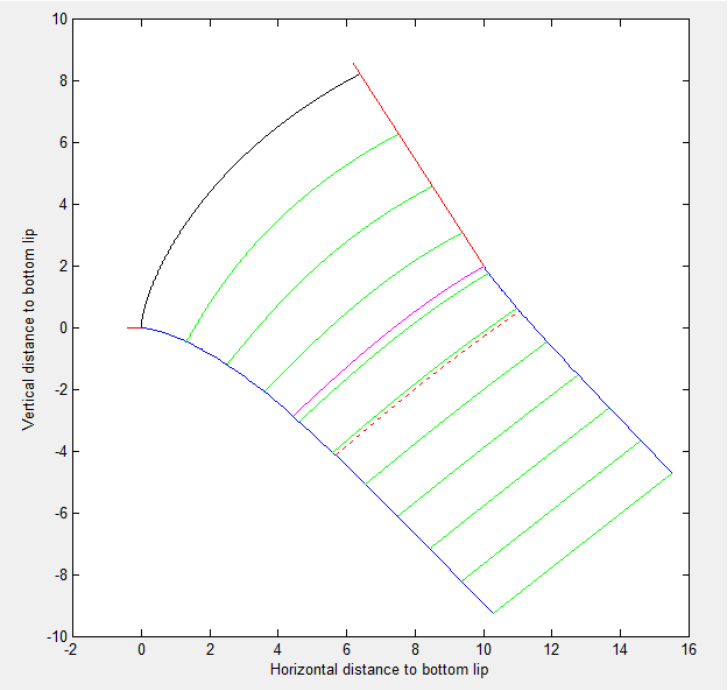

Figure 3.10: Positioning of the vena contracta for a negative L/b value

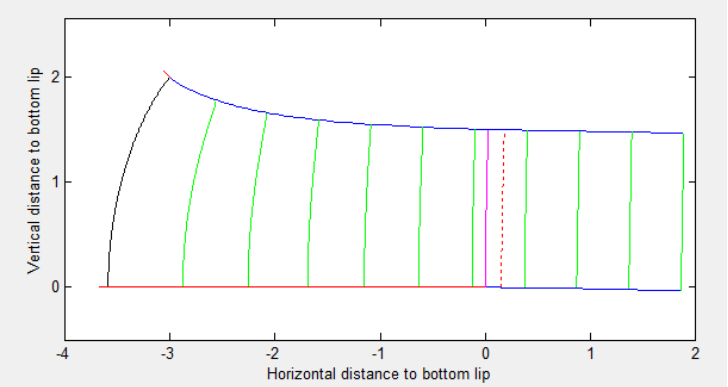

Figure 3.11: Positioning of the vena contracta for a positive L/b value

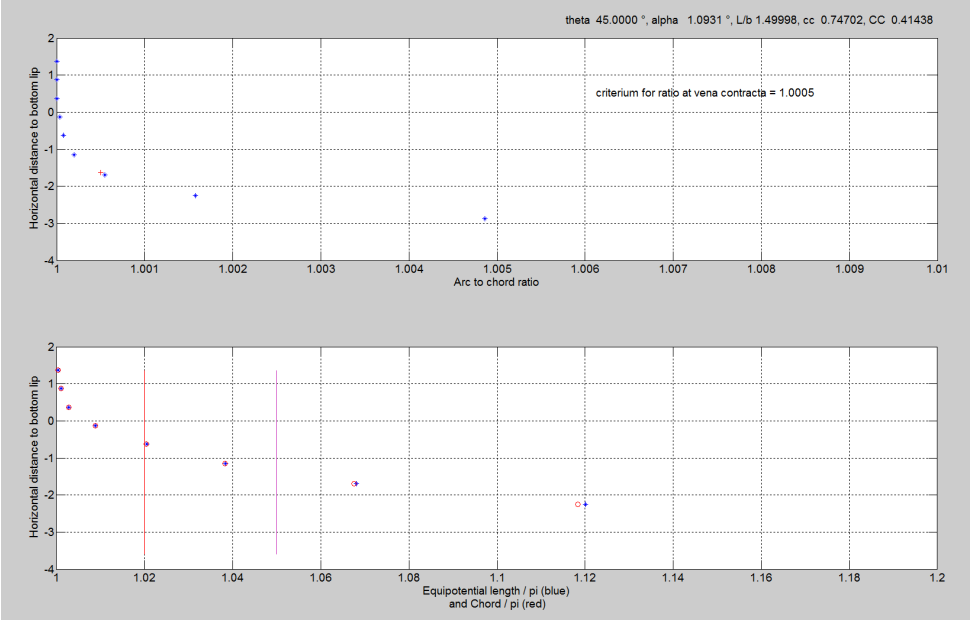

Figure 3.12: Positioning of the vena contracta according to both criteria

3.2.3 Two-phase computational fluid dynamics model

Considering that the jet shape is sensibly the same all over the width of the headbox, we can conclude that a 2D model can be applied to get the information we are looking for. It is well known that the ratio between the viscosities of the fluid flowing out of the nozzle and that of the environmental static fluid is one of the main parameters in jet formation.

- In this work we decided not to study the influence of this parameter in our case, even though is a main parameter, because in industrial conditions the vector fluid used is water with a small concentration of fibres so its rheological behaviour is very similar to a Newtonian fluid and the environmental static fluid is air. Normally these fluids can not be changed in a classical industrial installation so we can not think of an actual industrial practical application. Nevertheless, we can imagine a possible scenario where this phenomenon can be applied in order to obtain a more coherent jet. For this, there are two possible solutions, either use a more viscous vector fluid for the pulp or have an environmental fluid thinner than air. The advantage of using a more viscous fluid is the limitation of flocculation of fibres and therefore obtention a more homogeneous paper. This could be an interesting future development for papermaking. However it should be kept in mind that the whole wet-end should be re-designed, because the vacuum levels at the wire using a more viscous fluid will increase and the transportation of such a fluid will also cost more money because of higher energy consumption.

- For our purpose, a restriction is imposed by the impossibility of using a submerged jet for modelling this jet, therefore such jet can not be used as a laboratory scale equipment (like an air-air jet) to validate the jet shape nor a single-phase model programmed in CFD. To solve this restriction, we have chosen to use a two-phase numerical model to get the free-streamline boundaries of the jet.

The model that adapts the better to this kind of problems is a Volume of fluid (VOF) formulation proposed in the commercial package Fluent^{TM}.

The VOF model is a fixed grid technique designed for two or more in miscible fluids where the position of the interface between the fluids is of interest. In the VOF model, a single set of momentum equations is shared by the fluids, and the volume fraction of each of the fluids in each computational cell is tracked throughout the domain. Applications of the VOF model include the prediction of jet breakup, the motion of large bubbles in a liquid, the motion of liquid after a dam break, and the steady or transient tracking of any liquid-gas interface.

The VOF formulation works as follows: For each individual phase added to the model, a new variable is introduced, which is the volume of fraction of the phase in the computational cell. The variables and properties in any given cell are either purely representative of one of the phases, or representative of a mixture of the phases, depending upon the volume fraction values. The control-volume formulation used by Fluent^{TM} requires that convection and diffusion fluxes through the control volume faces be computed and balanced with source terms within the control volume itself. There are four schemes in Fluent^{TM} for the calculation of faces fluxes for the VOF model: a geometrical reconstruction, donor-acceptor, Euler explicit and implicit. The geometric reconstruction scheme represents the interface between fluids using a piecewise-linear approach. It is the most accurate scheme available at Fluent^{TM} and is applicable for general unstructured meshes (see the work realised by Youngs to this matters [66]). The geometric reconstruction scheme assumes that the interface between two fluids has a linear slope within each cell, and uses this linear shape for calculation of the advection of fluid through the cell faces (see figure 3.13).

The first step in this reconstruction scheme is calculating the position of the linear interface relative to the centre of each partially-filled cell, based on information about the volume fraction and its derivatives in the cell. The second step is calculating the advecting amount of fluid through each face using a computed linear interface representation and information about the normal and tangential velocity distribution on the face. The third step is calculating the volume fraction in each cell using the balance of fluxes calculated during the previous step. When this geometric reconstruction scheme is used, a time-dependent solution must be computed. The continuity equation for the volume fraction

of one or more phases is solved using an explicit time-marching scheme. Fluent^{TM} automatically refines the time step for the integration of the volume fraction. However, for better precision, we have chosen to use a 10^{-6} second step.

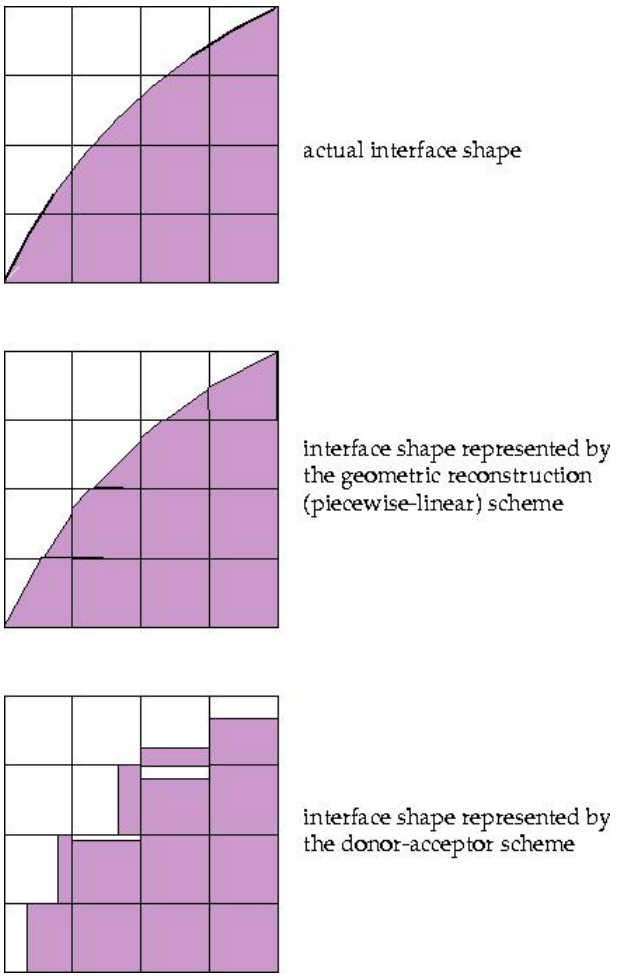

Figure 3.13: Fluent Geometrical reconstruction scheme

For more realistic results, a surface tension formulation was added at the VOF model. The surface tension model in Fluent^{TM}is the continuum surface force (CSF) model proposed by Brackbill *et al.* [67]. With this model, the addition of surface tension to the VOF calculations results in a source term in the momentum equation.

The turbulence model chosen was the realizable $k-\epsilon$ model proposed by Fluent^{TM}. This model was proposed by Shih [68] and gives more accurately predictions of the spreading rate of both planar and round jets. It is also likely to provide superior performance for flows involving rotation, boundary layers under strong adverse pressure gradients, separation, and recirculation. The realizable $k-\epsilon$ model requires very little more computational effort compared to the standard $k-\epsilon$ model.

The pressure-velocity coupling method chosen was the SIMPLE-consistent algorithm proposed by Fluent^{TM}. A conservative pressure-correction under-relaxation value was chosen to ensure the convergence of the physical model. The pressure interpolation scheme chosen was the PRESTO (PREssure STaggering Option) scheme that uses the discrete continuity balance for a "staggered" control volume about the face to compute the "staggered" (i.e., face) pressure. This scheme is extremely useful when there are jumps or large gradients in the momentum source terms between control volumes, or when the pressure profile has a high gradient at the cell face and cannot be interpolated using a standard scheme.

3.3 Results and Discussion

3.3.1 Results of ideal models

Results using Attwood model

An iterative algorithm was used to model the jet flow using the Attwood model. Figure 3.14 shows the algorithm structure used for the calculation.

The functioning of this algorithm is quite straight forward. From geometrical parameters of the headbox nozzle, we have determined the real value of the ratio L/b, then using an arbitrary value of α (angle of jet at the infinite), the opening of the nozzle b and the angle of the nozzle θ, we determine a new L/b ratio for that value of α. Both L/b ratios are then compared and if they do not coincide, then the value of alpha is corrected. This procedure is repeated until the difference between the real and the modelled ratio value is inferior to 10^{-5}. Finally, the streamlines and the equipotential lines of the calculated jet are plotted. The 3D-charts shown in figure 3.15 and in figure 3.16 present the results for the positive and the negative L/b ratio respectively. These values were validated using either direct measurement at the jet, or by image analysis of the jet shape overlapped to the calculated jet shape. Results show that, comparing the calculated jet to an image of the jet, the results fit very well for small values of b as depicted in figure 3.17(a) but not for bigger openings, i.e. figure 3.17(b).

As it is shown in figure 3.18, only the jet angle measured for values of nozzle opening b inferior to 15 mm coincide with the modelled values. In order to analyse the model validity, we have computed two other values, shown in red in figure 3.18, for nozzle openings of 20 mm and 22 mm. The deviation between measured and modelled angles for these two points is important, i.e. measured angles 6.0° and 6.3° while modelled angles are 8.0° and 8.7°. Therefore they are excluded from the linear regression analysis.

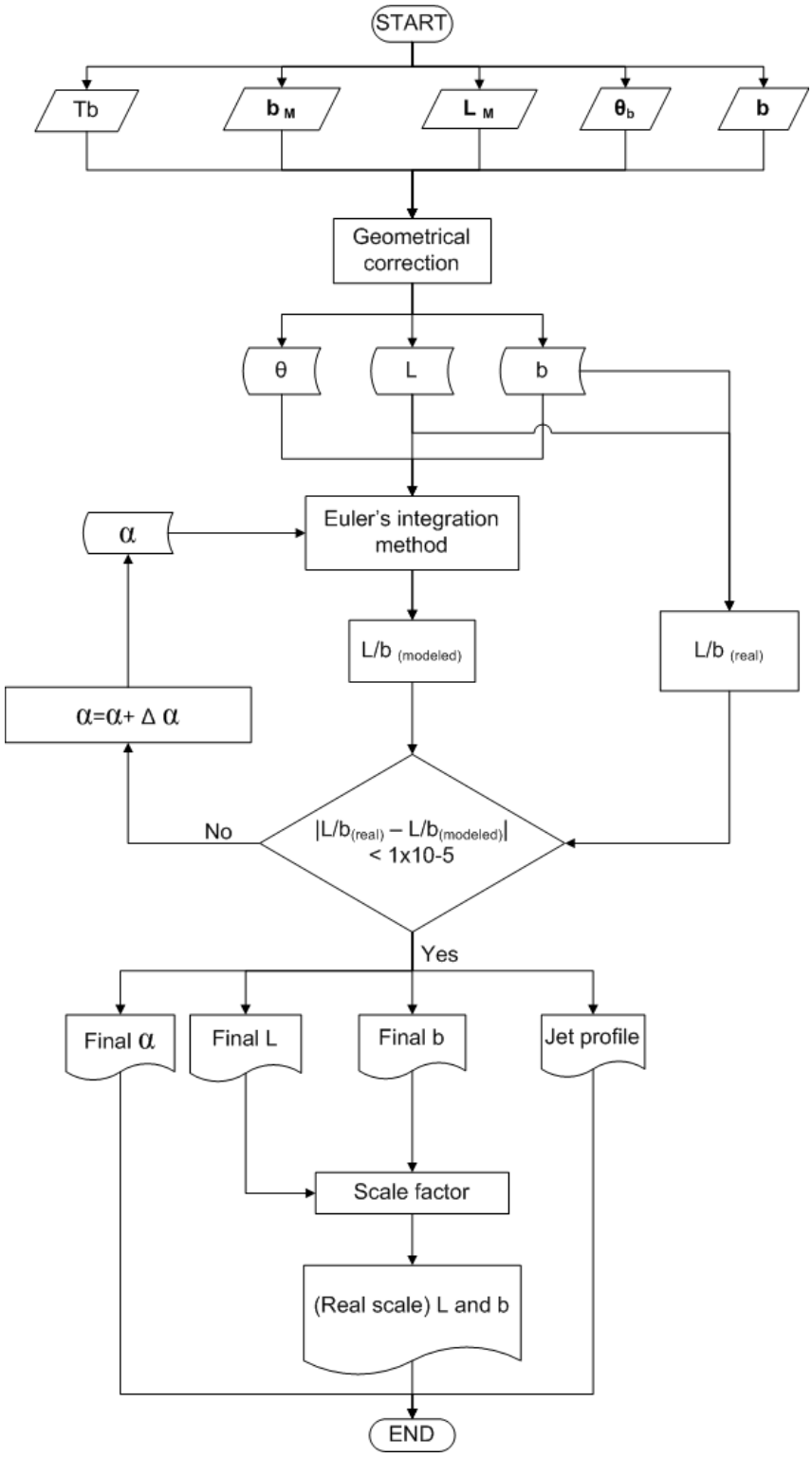

Figure 3.14: Algorithm structure

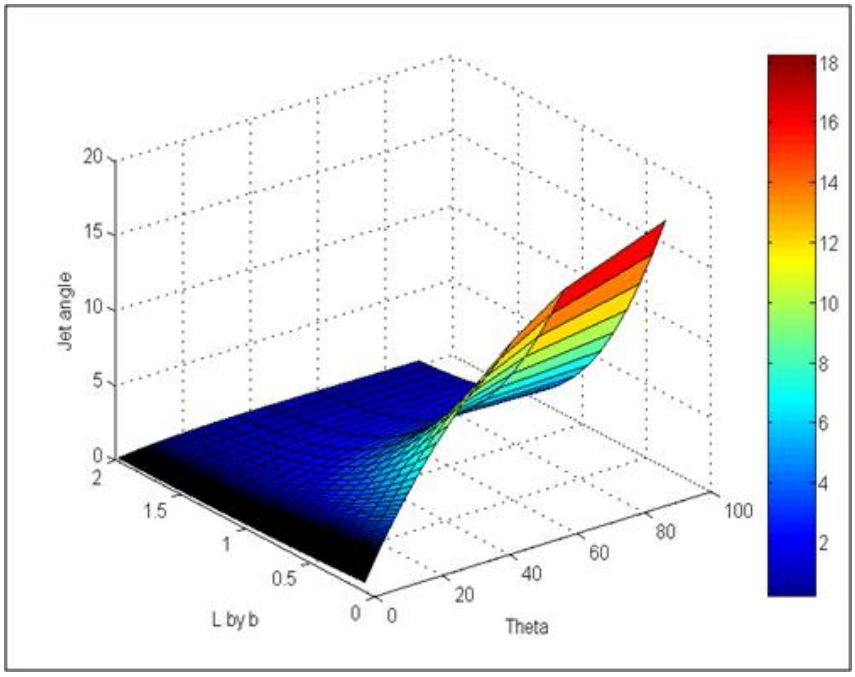

Figure 3.15: 3D chart of the jet angle as a function of the convergent angle (θ) and positive values of the L/b ratio

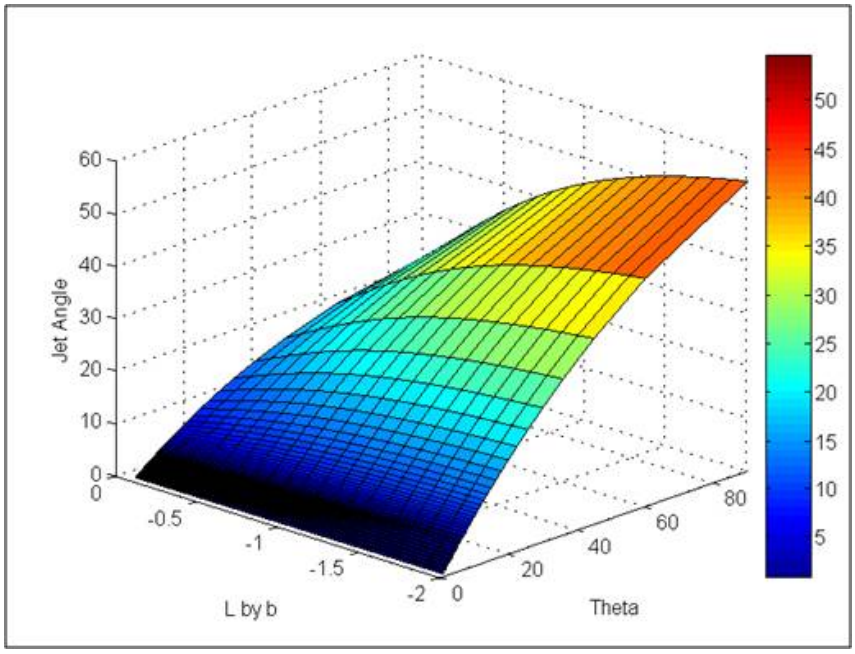

Figure 3.16: 3D chart of the jet angle as a function of the convergent angle (θ) and negative values of the L/b ratio

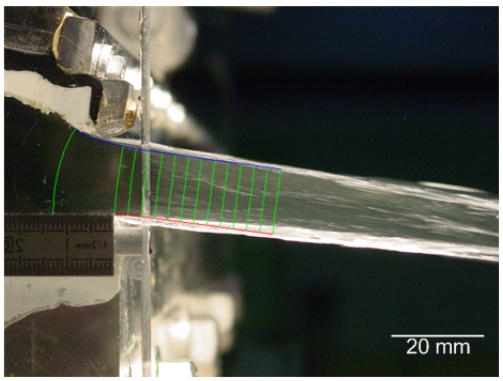

(a) b=14 mm

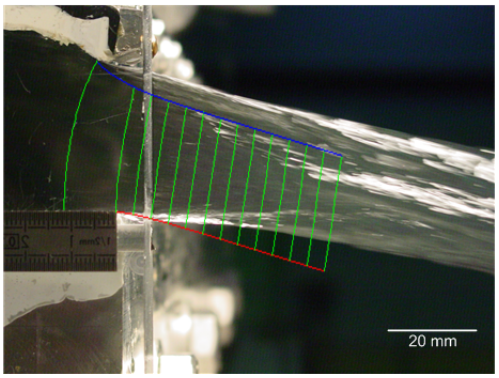

(b) b=22 mm

Figure 3.17: Comparison of the jet shape and the predicted values by the model

The 5 % error obtained between the measured and modelled values for openings inferior to 15 mm is acceptable owing to the difficulty of measuring the jet angle.

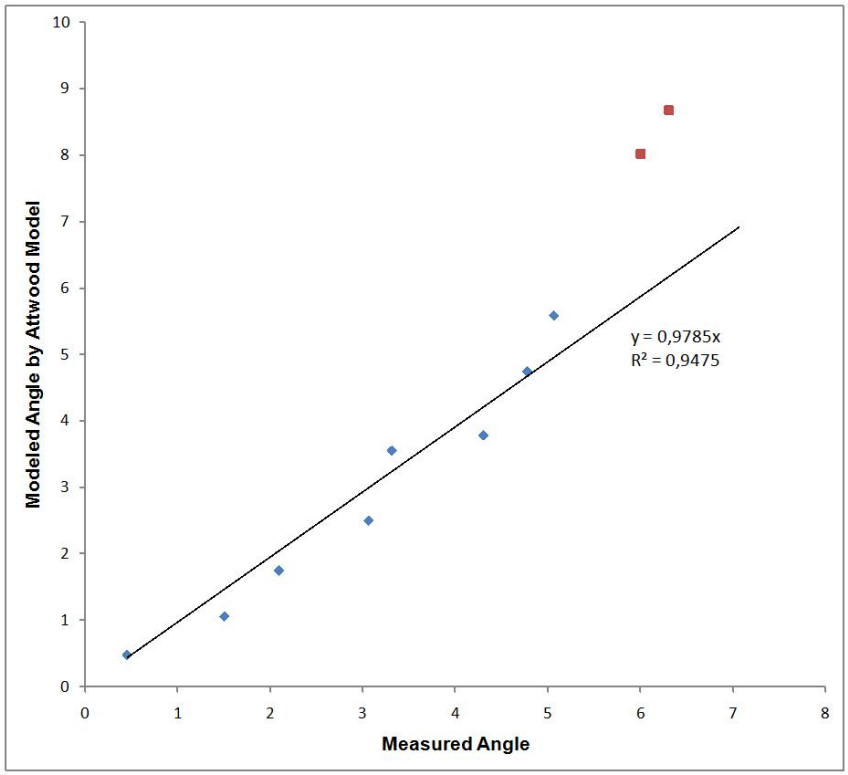

Figure 3.18: Comparison of the predicted jet angle and the measured jet angle

Results using Beta model

As expected, the results obtained with this method and the previous one are very similar. However, the computation is simpler with a library for computing the incomplete beta function. Furthermore, the possibility of getting any possible angle by means of a rational fraction is possible. Nevertheless, we must notice that the angles obtained by this model, as well as the previous one, do not fit to measured ones for values of b bigger than 15 mm i.e. figure 3.19. This can be explained by the fact that the flow comes from an infinite nozzle and in reality this is not the configuration used. As it was remarked by Appel, the contraction ratio of the nozzle plays a major role in the accuracy of the jet shape prediction.

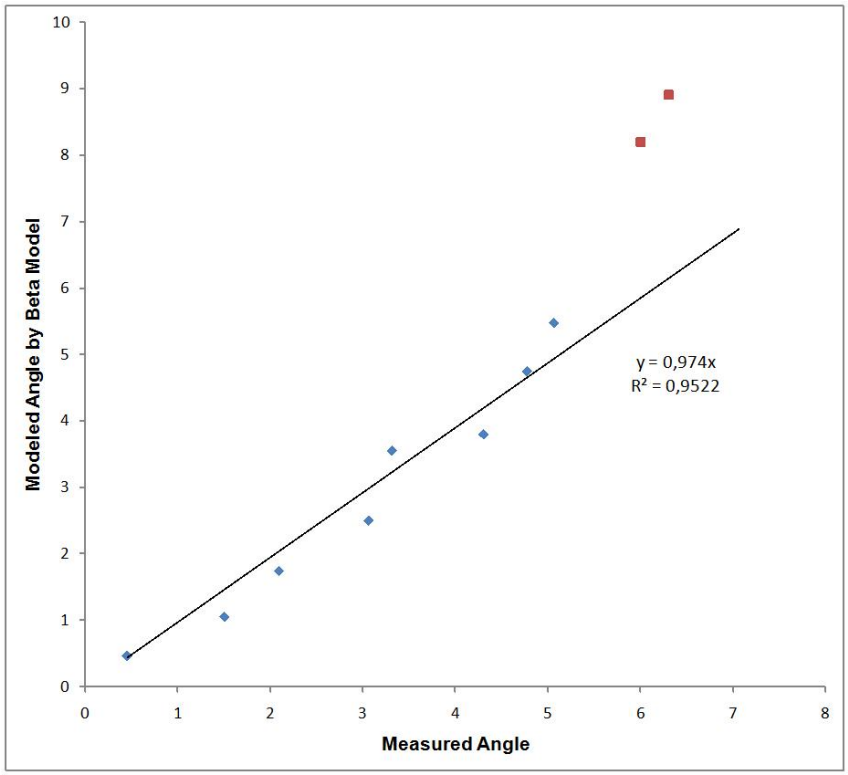

Figure 3.19: Comparison of the predicted jet angle and the measured jet angle

Results using the Schwarz-Christoffel model

Using Dias equation, we decided to revisit the analytical solution proposed by Appel for the geometry shown in figure 3.8 and to give an answer for every kind of nozzle. For a given convergent angle we computed the jet angle and contraction coefficient as a function of L/b for every contraction ratio of the nozzle (b/B). A typical result for a 60° convergent is shown in figures 3.20 and 3.21. As expected the results given by Appel model are similar to those obtained by the equation proposed by Dias. Nevertheless the Dias method enables us to compute a solution for any convergent angle.

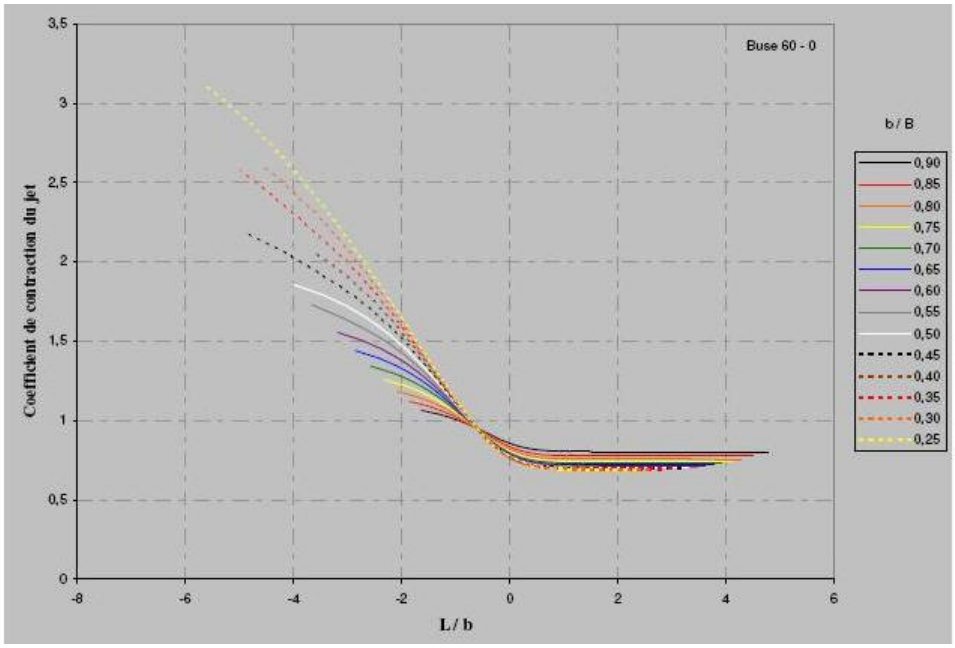

Figure 3.20: Jet contraction ratio as a function of the L/b ratio for every contraction ratio of the nozzle proposed by Appel for a convergent angle of 60°

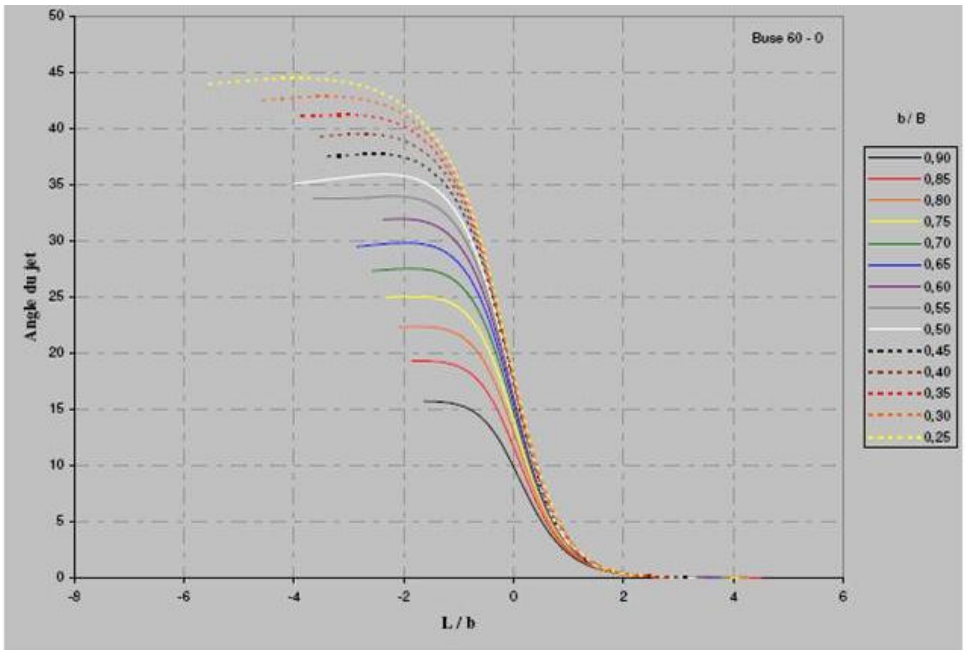

Figure 3.21: Jet angle as a function of the L/b ratio for every contraction ratio of the nozzle proposed by Appel for a convergent angle of 60°

Furthermore it was observed that the method proposed by Dias can be customised to get a better precision. If a double convergent nozzle geometry is used, as the one described in figure 3.9, not only the ratio b/B is important. Indeed, the presence of a double convergent can modify the jet angle as well. Some results obtained for a double convergent nozzle are shown in table 3.1, and compared to the values obtained for a single convergent. The angles used for this comparison are described in the figures 3.8 and 3.9 shown previously.

		Double convergent				Simple convergent			
L/b	b/B	β_2, °	$\beta 1$, °	b/C	α , °	$\beta 1$, °	α , °	$\beta 1$, °	α , °
0,8146	0,9508	10	60	0,6896	3,12	70	2,41	60	2,35
0,7155	0,9508					70	3,12		
0,6464	0,9508							60	3,12
0,8388	0,9490	10	60	0,9155	2,71	70	2,36	60	2,39
0,7559	0,9490						2,71		
0,7411	0,9490							60	2,71
0,3557	0,8390	10	60	0,6168	8,72	70	7,87	60	7,61
0,2831	0,8390					70	8,72		
0,2600	0,8390							60	8,72
0,2221	0,8293	10	50	0,6657	10, 38	60	9,38	50	8,92
0,1436	0,8293					60	10,38		
0,1004	0,8293							50	10,38

Table 3.1: Influence of a double convergent on jet angle

In this table we can see that the presence of a double convergent can modify the jet angle. Indeed, different values are obtained for the same value of the final convergent angle. For instance, for a L/b ratio of 0.8146 with a b/B ratio of 0.9508, β_1 equal 60° and β_2 equal to 10°, i.e. a final convergent angle of 70 °, the jet angle obtained is 3.12° while for a single convergent using a nozzle of 70° the jet angle obtained is 2.41° only. It is possible to obtain the same jet angle as the one obtained by the double convergent, but the L/b ratio should be reduced to 0.7155.

3.3.2 Results using Computational fluid dynamics

We have chosen to study the evolution of the jet shape for nine different L/b ratios and eight different convergent angles, for a fixed b/B ratio as shown in table 3.2. We know from previous sections in this work that the geometrical setup of the nozzle, especially the L/b ratio and the b/B ratio, play a role in the jet shape. The aim of this section is to study the influence of other parameters like turbulence levels, gravity, etc. on the jet shape. Another subsidiary objective is to try to determine by means of CFD the jet quality, especially the boundary of the jet (mixing between air and water). Indeed, this could be a good estimation of the quality of the jet coming out of that nozzle. Finally, we wanted to explore the velocity and pressure fields inside the jet in order to validate the previous models and the positioning of the vena contracta.

L/b	-2	-1.5	-1	-0.5	0	0.5	1	1.5	2
θ	20	30	40	50	60	70	80	90	
b/B	0.66								

Table 3.2: Geometrical parameters studied by CFD

Some of the results are shown in figures 3.22(a), 3.22(b) and 3.22(c). They display the shape of the jet delivered by a 2D nozzle and the velocity contours.

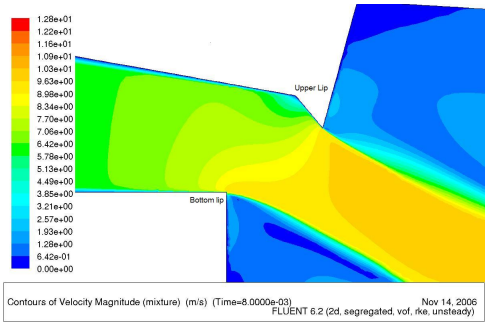

(a) L= -15 mm; θ=50°

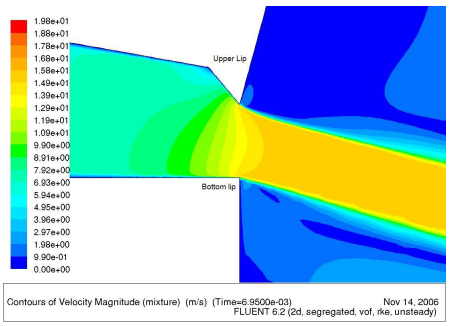

(b) L=0 mm; θ=50°

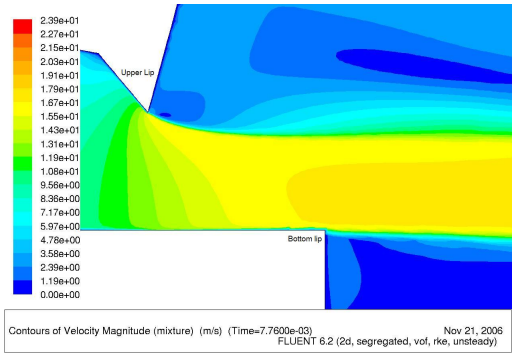

(c) L=15 mm; θ=50°

Figure 3.22: Velocity contours for three different nozzles in a two-phase CFD

It can be seen that the shape of the velocity contours look like the equipotentials of the ideal fluid models. In figure 3.23 we can notice that the mixing layer between water and air remains almost the same whatever the shape of the nozzle. No noticeable effect of the quality of the jet can be concluded from this kind of model.

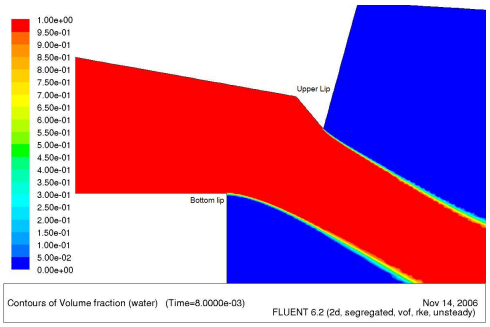

(a) L= -15 mm; θ=50°

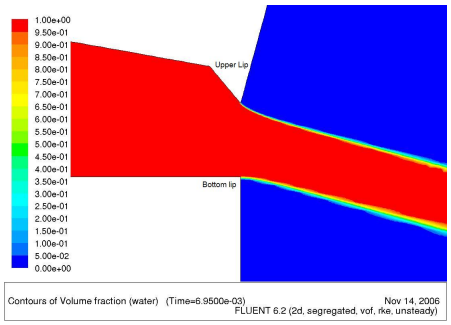

(b) L=0 mm; θ=50°

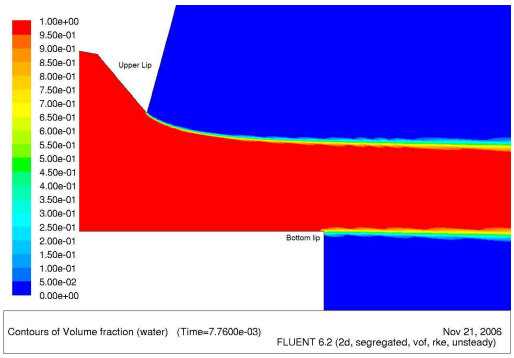

(c) L=15 mm; θ=50°

Figure 3.23: Volume fraction contours for three different nozzles in a two-phase CFD

Turbulence contours (see figure 3.24) can also be obtained from the simulations. Nevertheless, we must take the values with caution, if trying to transpose them to fibre suspension flows, owing to the very particular rheological properties of pulp suspensions. Therefore we will not comment on the results.

The corresponding pressure contours are presented in figure 3.25. They help us to assess where the vena contracta is located. Indeed it is where the pressure inside the jet is equal to the atmospheric pressure. We can notice that it is always inside the bottom lip. This result confirms the previous models, based on ideal flows, which gave similar results. We made pressure measurements at the bottom lip for several openings in order to validate these results. The experimental results show us that a strong pressure drop occurs at the bottom lip and therefore the atmospheric pressure is found before the end of this lip extension, as shown in figure 3.26. Another interesting conclusion is the shape of the vena contracta, up to now supposed straight or parabolic. In the last figures we can see that, depending on the geometry of the nozzle, the shape of the vena contracta looks like a “S” shape.

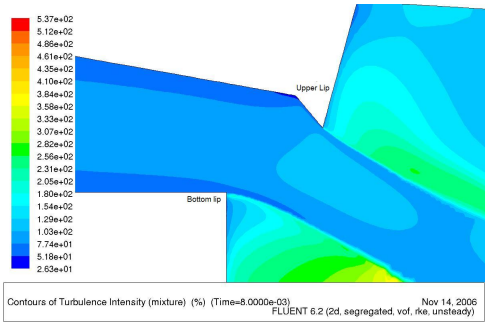

(a) L= -15 mm; θ=50°

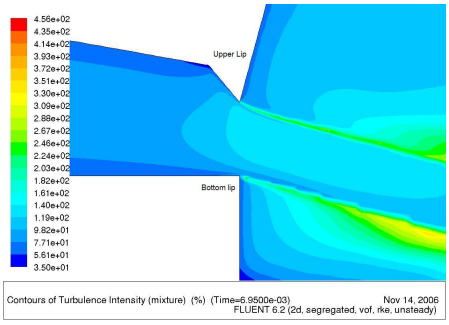

(b) L=0 mm; θ=50°

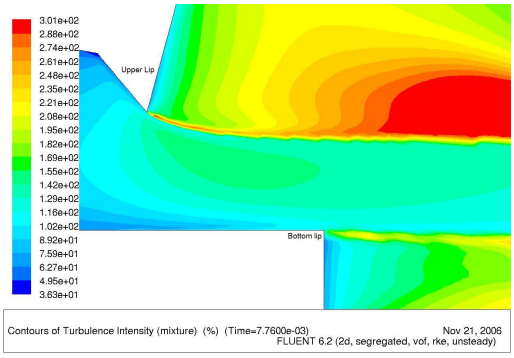

(c) L=15 mm; θ=50°

Figure 3.24: Turbulence intensity contours for three different nozzles in a two-phase CFD

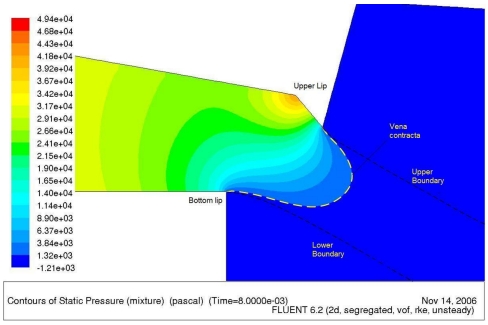

(a) L= -15 mm; θ=50°

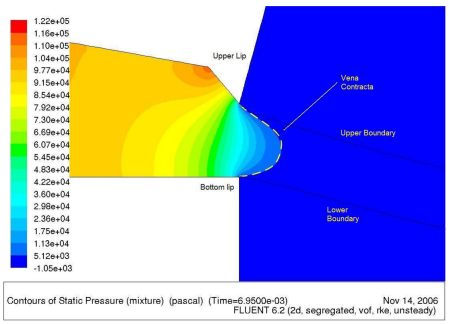

(b) L=0 mm; θ=50°

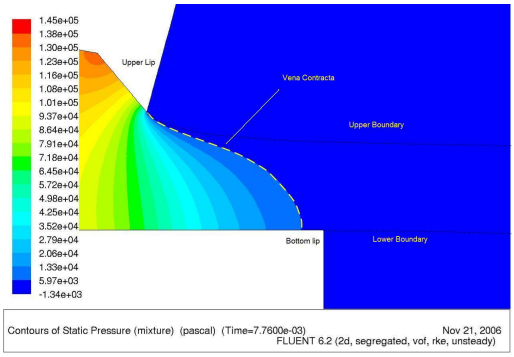

(c) L=15 mm; θ=50°

Figure 3.25: Static pressure contours for three different nozzles in a two-phase CFD

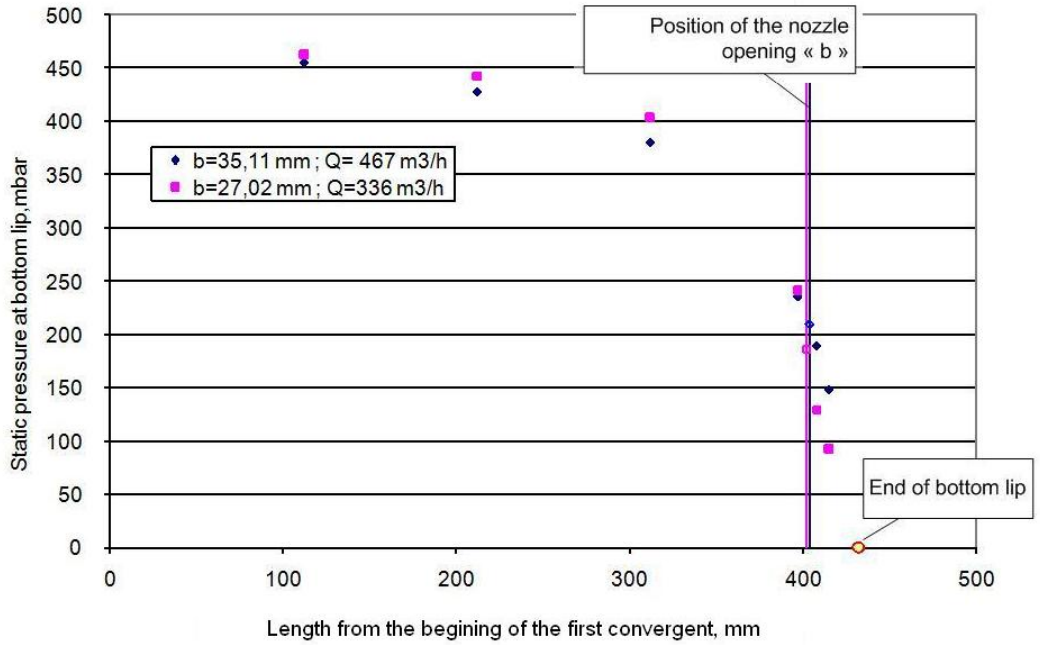

Figure 3.26: Measured position of the vena contracta

Comparison between Computational fluid dynamics and Ideal models.

The next table summarises advantages and drawbacks of the models tested in this chapter.

Model	Advantage	Drawback
Classical Method	Easy to use in industrial applications Jet angle and contraction coefficient can be calculated	Not physical for modern headboxes
Attwood model and Beta functio	Whole jet shape can be calculated Streamlines and equipotentials No need of special hardware Positioning of the vena contracta Computation of the contraction ratio	Works only for small headbox openings Ratio b/B not considered Infinite convergent only
Schwarz-Christoffel	Whole jet shape can be calculated Streamlines and equipotentials No need of special hardware Any nozzle is possible	Mathematically complex Ideal fluids only
CFD	Pseudo real fluid could be used Other information could be obtained (turbulence, boundary mixing)	Need of special hardware Need of specialists in CFD Expensive and long calculations

Table 3.3: Comparison of different models

3.4 Conclusions

We have tested several models in order to predict the behaviour of the headbox jet. It was shown that for industrial application a CFD model is not necessary, even though it gives much more information (turbulence, mixing layer, etc.) than the other models. A CFD model represents a high investment in terms of hardware, time of calculation and qualified people to run the code. This kind of model could be very useful for the dimensioning and design of new equipment (machine suppliers) that could give a reasonable amortisation of this kind of material. Of course this kind of computational model depends on the rheological model imposed. For our purposes a Newtonian model fits quite well to the physical measurements.

However, a model representing the real behaviour of the pulp at different concentrations is necessary and could give more information for a better optimisation of the papermaking processes. A possible way to do this is to identify the different rheological responses according to the shear rates imposed. In other words, no single rheological model could be applied to the pulps, but a collection of different reactions accordingly to the shear rate imposed. If this could be used inside the CFD model, then a more realistic result could be got.

On the other hand, for industrial applications, a simple software, based on the mathematical model for potential flows using a Schwarz-Christoffel formulation, could be applied. The information given by this kind of model are extremely precise for this application with cheap investment in hardware (any modern computer can handle this calculation in short time). However no information can be obtained about the quality of the jet in order to optimise the nozzle. This kind of model can be very useful for the every-day machine operation, with precise values of the jet constriction, speed and angle. As the angle and speed of the jet are very difficult to measure in a real industrial setup, we think that the model proposed could be extremely useful for every day operation.

Chapter 4

Conclusions

This work aimed at characterising the internal and external flows of a headbox in order to get rules for designing a headbox.

The first chapter of this work was intended to give a historical background of the state-of-the art of headboxes technology. Papermaker's believes deeply influence the design of some of this headboxes retarding the development of hydrodynamic-based headboxes.

In the second chapter, it could be seen that if a proper, homogeneous pulp distribution was already achieved at the stabilisation chamber, then the headbox can be optimised. The Coanda effect was found at the inlet of the stabilisation chamber. It was shown that any perturbation found inside the headbox can interfere to the whole functioning of the headbox.

Several orifice plate geometries were studied. It was seen that a certain deflocculating effect is got but at a high energy dissipation. This amount of energy is related to the small constriction that has to be imposed at the inlet of the tube bank. It was also shown that to optimise this constriction, its size should be related to the type of pulp passing through it. In other words if the pulp passing through the constriction is a softwood pulp then the constriction should be smaller (energy applied higher) than if it is a hardwood pulp for which the constriction could be a larger. Considering the high energy dissipation and the risk to block out the entire headbox, these optimised constrictions can not be kept in industrial conditions. However it can be interesting to try a moveable constriction of the tube bank related to the consistency of the pulp and the length of fibres used. For the normal tube bank geometries, especially the geometries used nowadays in the papermaking industry, no notable deflocculating process was seen. Nevertheless, industrial testimony described a better paper formation by the use of this type of geometry. Several theories were proposed to try to describe this phenomenon, unfortunately no experimental method was found to validate these theories. We believe that most of the energy applied at the

tube bank is wasted in the fluid medium and not applied at the deflocculating process. If this is true, it will mean that a certain slip exists between the fibres and the fluid, even though the fibres represent only a little amount of volume inside the fluid. This could be essential for the total understanding of the deflocculating process because it would mean that the same amount of energy applied by the tube bank should be applied by other ways (ultrasound by instance) directly to the fibres and not into the fluid if we want to optimised this process.

It was also shown that the geometrical configuration of a tube bank is closely related to some perturbations found afterwards at the sheet formation. These perturbations can be minimised if a streamlined profile is respected for the design of the turbulence generator and a staggered placing method is used to avoid secondary flows.

The nozzle itself, even though for many people does not represent a main parameter at the headbox design, should be reconsidered. Comparing to other researches made for mining industry it was shown that for obtaining a more coherent jet some geometrical rules should be applied to the nozzle design. It could be interesting to check whether these design parameters apply or not in order to obtain an optimised jet. From the CFD simulations made inside the headbox, no noticeable effect could be seen to conclude that these parameters are the best one for the papermaking industry. Nevertheless, a CFD model can not replace a real experimental setup where the evolution of the jet can be seen and compared to other geometries. It could be very interesting to determine if these geometrical nozzle parameters can be optimised to get a better jet, without secondary flows and breaks up.

From a deflocculating point of view, it was seen big structures reformed at the nozzle and were stretched at the lips. No deflocculating process was seen at this point. This is quite logical because inside the nozzle the turbulence decays. It can be said now, that the scale and intensity of turbulence should be kept inside this nozzle. This justified the use of vanes inside the nozzle that will keep as long as possible the turbulence intensity and scale over the nozzle. Several works treated this subject and much literature can be found in the optimisation parameters of these vanes.

Although it was shown that the design of an optimised headbox is possible, the quality and the shape of the jet flowing out of the headbox are unknown. A prediction of the jet shape for a better positioning of the headbox in the paper mill is not made and a predefinition of the headbox capacity (range of jet speed, angle, etc) is completely unknown for the papermaker.

In the third chapter, we have tested several models in order to predict the geometry of the jet delivered by a headbox. Experimentally we observed that the global jet shape does not change using water or a diluted fibrous suspension. Roughness of the jet surface

does indeed change if a fibrous suspension is used. This could mean that the turbulence scale is modified by the presence of fibres, but there is no measuring technique allowing a precise measurement to say how much of this energy was absorbed by fibres and what was the global effect in deflocculation.

It was shown that for industrial application a CFD model is not necessary, even though it gives more information (turbulence, mixing layer,etc.) than the other models. A CFD model represents a high investment in terms of hardware, time of calculation and qualified people to run the code. This kind of model could be very useful for the dimensioning and design of new equipment (machine suppliers) that could give a reasonable amortization of this kind of material. Of course this kind of computational model depends on the rheological model imposed. For our purposes a Newtonian model fits quite well to the physical measurements. However, a model representing the real behaviour of the pulp at different concentrations is necessary and could give more information for a better optimisation of the papermaking processes. A possible way to do this is to identify the different rheological responses according to the shear rates imposed. In other words, no single rheological model could be applied to the pulps, but a collection of different reactions according to the shear rate imposed and the geometrical conditions. If a reliable model was achieved then it would lead us to a break-through technology like for instance the reduction of water consumption.

On the other hand, for industrial applications, a simple software using a mathematical model based on Schwarz-Christoffel formulation could be applied. The information given by this kind of models are extremely precise for this application with cheap investment in materials (any modern computer can handle this calculation in short time). However no information can be obtained about the quality of the jet for optimisation of the nozzle. As the angle and speed of the jet are very difficult to measure in real industrial conditions, we believe that this kind of model can be very useful for the regulation of the machine operation, with precise values of the jet constriction and angle. Another important achievement of this work is the location of the vena contracta which can be of extreme utility for the machine operability.

Even though, much progress was done, several questions must be answered and new measuring equipment should be developed in order to optimise the fibre distribution and control. We have made an energy study of each part of a headbox. Several phenomena were observed thanks to experimental work performed with our laboratory setups and thanks to CFD. Some optimisations were proposed for our particular setup. We cannot conclude that all these rules will be suitable for every headbox available in the market, since the type of headbox and the technology used is intimately related to the kind of paper and its quality. However, we wanted to point out that, using some common-sense based criteria, the energy applied into the system should be better employed and there

are available tools to analyse part of the problem. In a world where energy and water are becoming the strategic values of the future, some efforts should be made to get a clearer understanding of paper formation and therefore a water and energy reduction. For this, the first problem to be solved, which is a real challenge, is getting a reliable non-invasive measuring technique for determining the slippery between fibres and water. If this slippery exists then it would mean that the turbulence levels applied into the fluid, intended for de-flocculation, are not completely used by fibres themselves.

Appendix A

Computational fluid dynamics results

A.1 Velocity contours

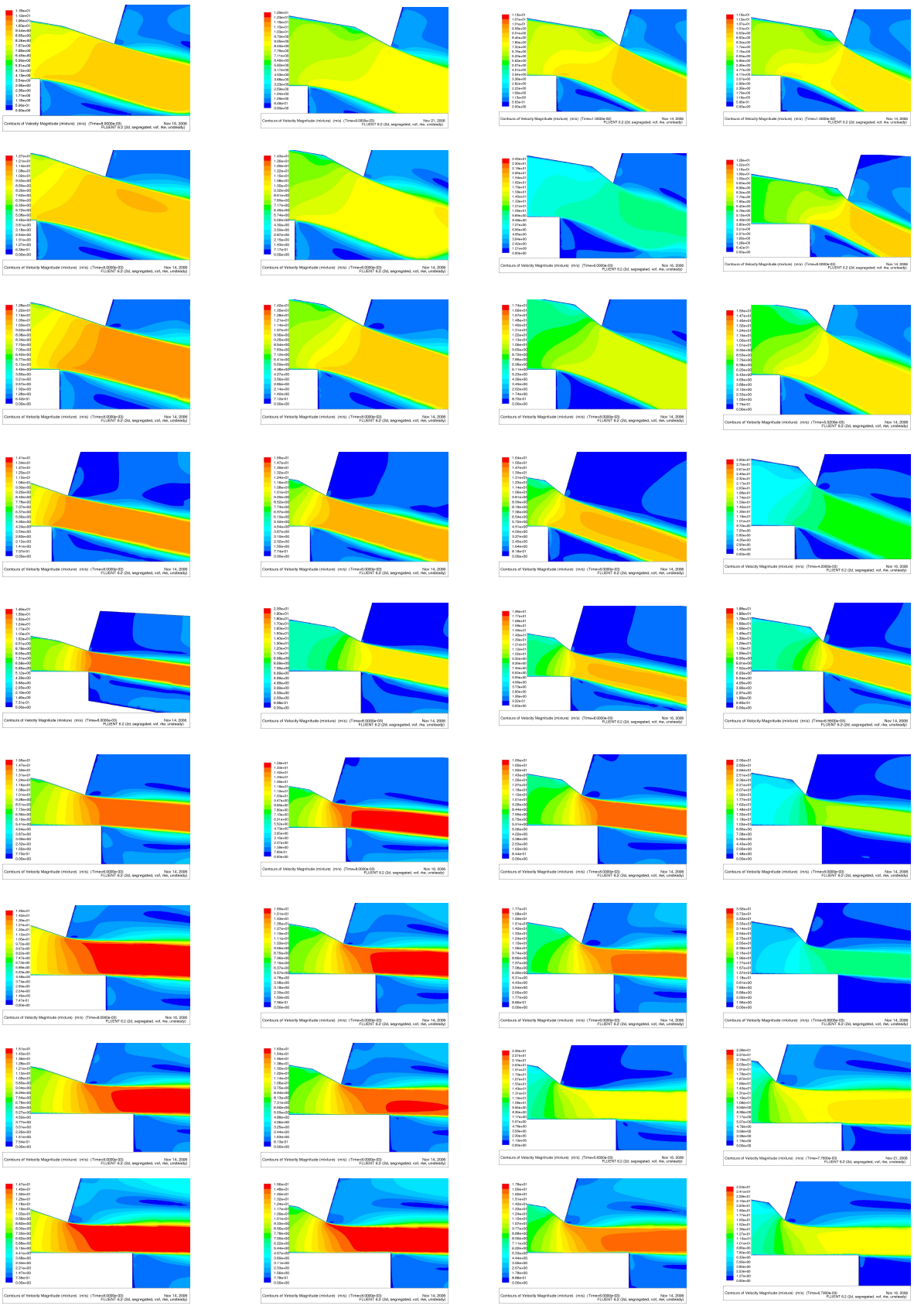

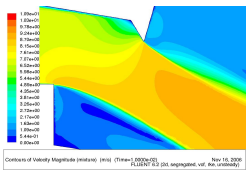
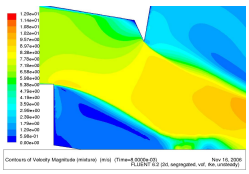
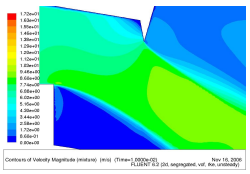
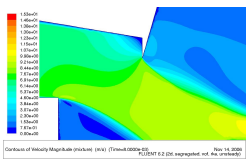
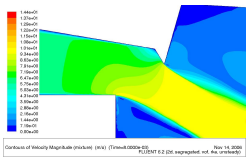
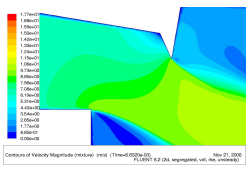
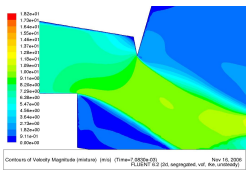
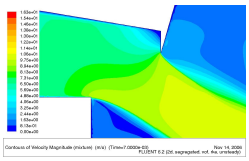
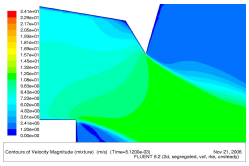
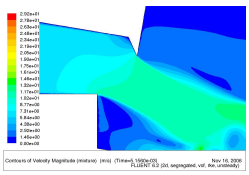
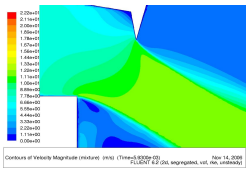
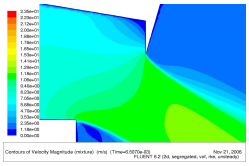
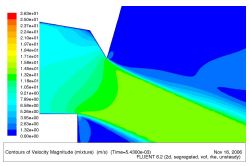
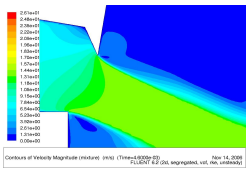
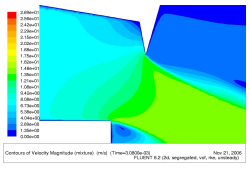
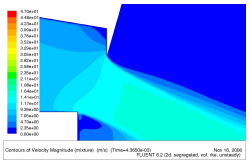
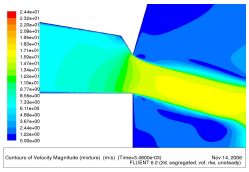
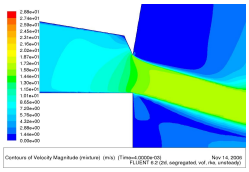
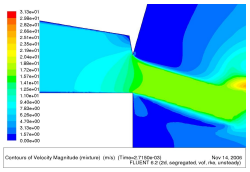
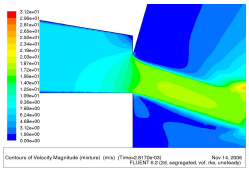
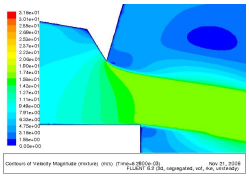
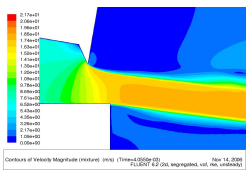
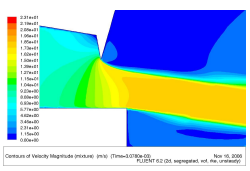
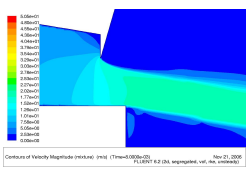
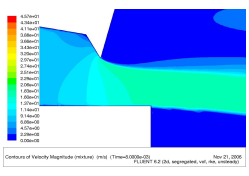
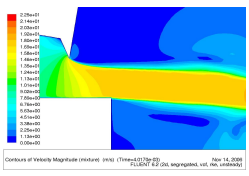
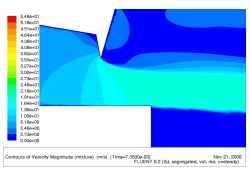
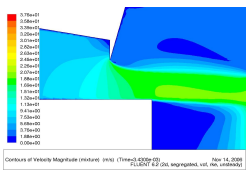
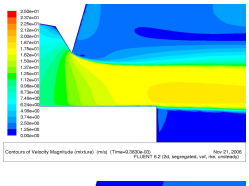
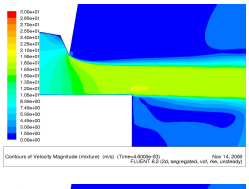
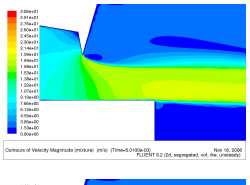
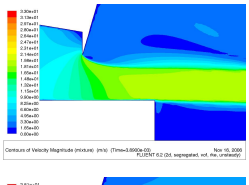
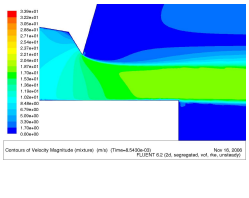
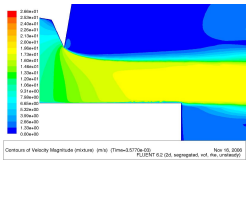
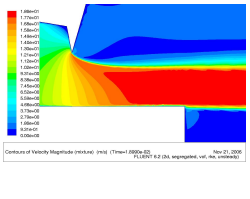
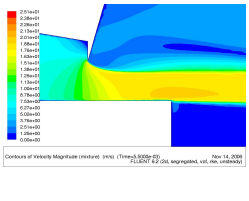

A.2 Pressure contours

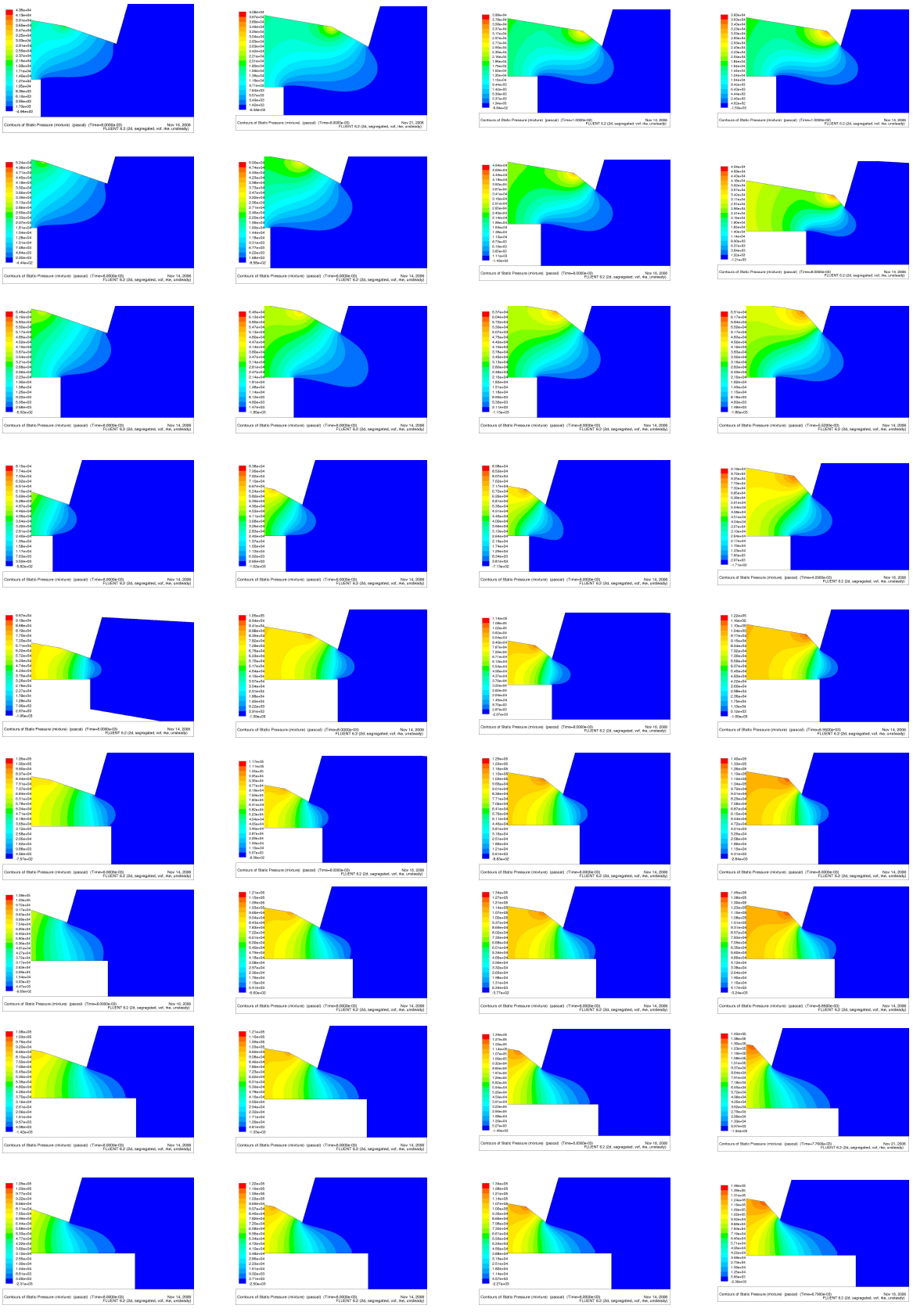

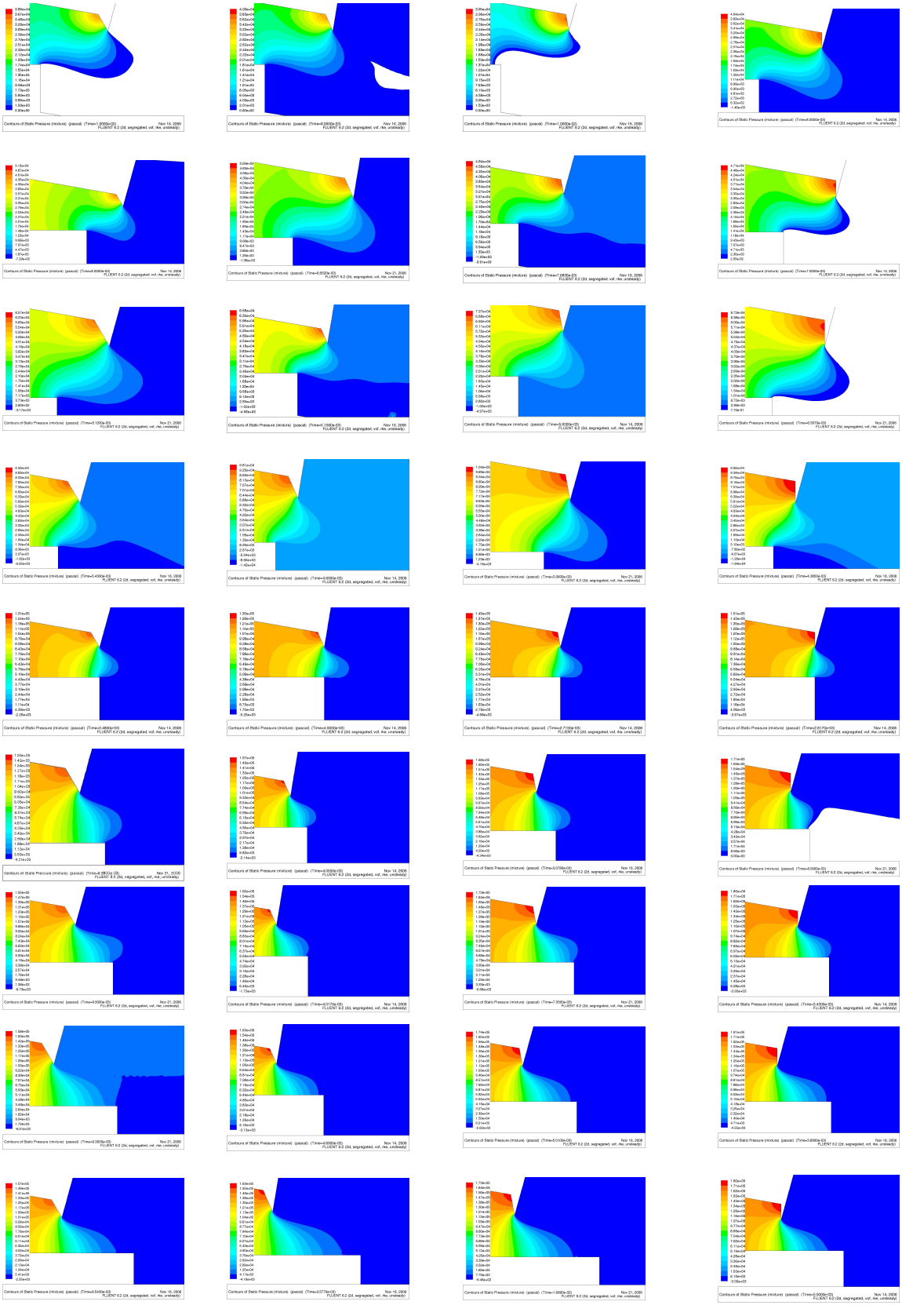

Annexe B

Résumé étendu en Français

L'évolution des machines à papier pour obtenir des papiers toujours de meilleure qualité à une cadence de production toujours plus rapide impose l'utilisation de systèmes complexes et de plus en plus précis. Les caisses de tête, partie centrale et essentielle d'une machine à papier, qui délivrent la suspension fibreuse diluée sur une toile de formation n'ont pas échappé à cette évolution continuelle. Au cours des cinquante dernières années, des travaux de recherche fondamentale ont été réalisés pour essayer de comprendre la rhéologie des suspensions fibreuses et donner une réponse scientifique afin d'obtenir une meilleure distribution de la pâte dans l'unité de formation. Cependant, quoique quelques avancées majeures aient été faites dans ce domaine, il reste des points obscurs dans la conception des caisses de têtes modernes :

- Certains d'entre eux sont dûs à un manque de connaissances du comportement des suspensions fibreuses en raison de leur complexité et de l'absence d'outils de mesure.
- D'autres viennent de "vieilles croyances papetières" qui ont maintenu quelques traditions dans la conception des machines.
- Et efin, d'autres encore viennent de clauses de confidentialité qui ont noyé le développement des caisses de têtes dans un océan des secrets et l'ont conservé à l'écart de données applicables.

On recherche de nos jours une description détaillée du comportement de suspensions fibreuses mais les paramètres rhéologiques principaux sont toujours inconnus. La formation du papier devrait être aussi homogène que possible afin d'assurer au papier une bonne qualité. Cependant, du fait de la nature et de la forme des fibres, la floculation est presque inévitable. Dans ce travail, conduit grâce à l'aide financière du ministère français de l'éducation et de la recherche et du laboratoire LGP2, nous essayerons de répondre à trois questions principales pour prévenir, autant que faire ce peut, la re-floculation de la suspension, de façon à obtenir une distribution la plus homogène possible :

- Est-il nécessaire de disposer d'un modèle rhéologique complet des suspensions fibreuses pour concevoir les caisses de têtes modernes ou bien les modèles de base sont suffisamment précis pour décrire l'écoulement ?
- Toutes les parties d'une caisse de tête sont-elles nécessaires ? Si oui, sont-elle optimisées ?
- Est-il possible de prévoir la géométrie du jet libre fourni par le bec de la caisse de tête avec des outils mathématiques simples ?

Le premier chapitre de ce travail présente l'historique de l'évolution des machines à papier et particulièrement de la caisse de tête. La complexité de la rhéologie fibreuse de suspension est mise en évidence. Ce n'est pas l'intention de l'auteur de décrire amplement ces sujets ; il souhaite juste donner une idée de la complexité de la fabrication du papier et de la raison pour laquelle, jusqu'ici, il y a un manque de connaissances dans ces secteurs.

Le deuxième chapitre concerne les éléments internes d'une caisse de tête. Son objectif est d'analyser les écoulements internes et de déterminer si l'on peut proposer des règles de dimensionnement, ou pas. Par conséquent, nous avons réalisé une étude expérimentale des écoulements de suspensions fibreuses ainsi que des simulations numériques par CFD en utilisant l'eau seulement. Pour l'étude expérimentale, nous avons fait des mesures classiques de perte de charge ; nous avons aussi employé des méthodes plus sophistiquées : imagerie à grande vitesse et mesure des profils de vitesse grâce à une technique non intrusive, la vélocimétrie Doppler à ultrasons pulsés. Nous avons comparé le comportement de la suspension à celui de l'eau. En effet, aucun modèle rhéologique n'est disponible pour décrire le comportement des suspensions fibreuses dans la gamme d'intérêt ; ceci peut être un problème pour l'application de la CFD. Cependant, nous avons observé que, pour la plupart des conditions industrielles analysées, le dimensionnement avec de l'eau est plus restrictif qu'en utilisant une suspension fibreuse. C'est pourquoi les simulations numériques ont été faites avec de l'eau afin d'analyser seulement l'intensité et la longueur de turbulence dans le système.

La commande du jet est un paramètre important dans la fabrication du papier. En effet, une bonne connaissance de l'angle du jet et de sa vitesse est nécessaire pour contrôler l'orientation des fibres. Par conséquent, nous consacrons le troisième chapitre de cette thèse à la prévision de la géométrie du jet. Nous avons analysé plusieurs modèles mathématiques, déjà publiés dans la littérature, applicables aux écoulements idéaux. Nous avons recherché non seulement l'angle du jet et son rapport de contraction du jet mais aussi le positionnement de la veine contractée. Nous avons complété l'étude par un travail expérimental afin de vérifier si ces modèles s'appliquent. Après avoir observé qu'il n'y avait

aucune différence significative dans la forme du jet entre une suspension fibreuse et l'eau, nous avons effectué des calculs de CFD avec un modèle diphasique pour prévoir la forme du jet. Nous terminons ce chapitre finit par une comparaison de toutes ces méthodes et de leurs limitations.

Enfin, nous présentons une conclusion générale et proposons quelques perspectives.

Étude de l'efficacité d'une caisse de tête et de son dimensionnement

Le dépôt des fibres sur la toile de formation est réalisé par un système (caisse de tête) qui contient plusieurs éléments. L'action de chacun d'entre eux sur la suspension fibreuse est essentielle pour obtenir une qualité de papier satisfaisante. L'objectif principal de ce chapitre est d'analyser l'efficacité énergétique de chaque dispositif à l'intérieur d'une caisse de tête. La motivation de ce travail vient d'une observation visuelle d'une caisse de tête en fonctionnement où l'on a noté que l'état de floculation d'une suspension fibreuse ne changeait pas de manière très significative d'un élément à un autre. Ceci signifierait que l'énergie utilisée à l'intérieur d'une caisse de tête pour la défloculation n'était pas correctement employée. En effet, vu la concentration et donc le facteur de encombrement, il doit y avoir les contacts continus entre les fibres dans ces suspensions ; elles floculent et il faut défloculer la suspension.

Nous avons décidé d'effectuer une étude individuelle des éléments les plus importants, afin d'obtenir une image plus claire de leur influence individuelle sur les suspensions fibreuses. Puis, dans un deuxième temps, nous avons étudié l'inter-influence de ces éléments afin de tirer une conclusion globale d'un point de vue énergétique et proposer quelques voies d'optimisation En effet, comme on l'a vu dans le premier chapitre, la formation est étroitement liée aux forces hydrodynamiques. Pour mieux comprendre ces forces nous avons décidé d'étudier chaque élément qui compose une caisse de tête séparément. Selon l'importance de leur action sur la qualité de papier et considérant qu'ils sont présents dans chaque caisse de tête commerciale, nous avons retenu trois éléments principaux dans cette étude :

- la chambre de stabilisation ;
- le générateur de turbulence (ou banque de tubes) ;
- et la section du convergent.

Chambre de stabilisation

On a considéré pendant longtemps que la chambre de stabilisation des machines à papier jouait un rôle direct dans la formation. En effet, on a longtemps crû que la formation se faisait dans la chambre de stabilisation et que le réseau fibreux ainsi formé se déposait sur l'unité de formation où l'on commençait l'extraction de l'eau. De nos jours, on donne une raison hydrodynamique pour garder cette chambre. Par conséquent, nous avons étudié le comportement de la suspension fibreuse dans différents bancs d'essai hydrodynamiques puis nous avons puis fait le passage à une chambre de stabilisation.

Il est bien connu qu'après une perturbation hydrodynamique, c'est-à-dire le passage par une singularité ou une pompe, un fluide a besoin d'une certaine distance pour récupérer un profil stable de vitesse. Cette distance a été souvent mesurée avec un fluide homogène comme l'eau, mais pouvons-nous considérer que la même distance est nécessaire avec une suspension fibreuse ? Afin de répondre à cette dernière question nous devons d'abord comprendre l'écoulement des suspensions fibreuses. À cet effet, nous avons employé un banc d'essai de mécanique des fluides conçu pour étudier l'écoulement de pâtes à papier en conditions industrielles.

Une conclusion intéressante obtenue à partir cette étude est le fait que les pertes de charge sont plus petites, pour n'importe quelle suspension, aux débits industriels élevés, c'est-à-dire pour des vitesses d'écoulement supérieures à 3 m/s. Ceci signifie que la viscosité apparente de la suspension est inférieure à la viscosité de l'eau seule. C'est une conclusion très importante parce qu'elle signifie que la conception d'un circuit avec de l'eau pur nous donnera un coefficient de sécurité pour le passage de n'importe quelle suspension dans l'installation. Cependant, un effet contraire se produit si la vitesse de l'écoulement est inférieure à 2 m/s parce que les pertes de charge pourraient être presque doublées pour la pâte, comparé à l'eau.

Nous avons pris des images à différents points du circuit grâce une caméra à grande vitesse (MotionScope 8000s de Redlake). Cette caméra nous permet faire 8000 prises d'images par seconde mais la résolution n'est alors que 60 pixels par 68 pixels. La résolution maximum, à plus faible fréquence d'acquisition, est 480 pixel par 420 pixel à 250 images par seconde. Ces résolutions ne sont pas assez bonnes pour obtenir une image détaillée du processus de défloculation mais elles permettent de faire des observations. En effet, nous voulons vérifier dans ce travail l'équilibre dynamique entre la défloculation et la régénération des agrégats pour différents débits, et dans ce cas-ci la résolution est suffisant. Nous avons fait des observations détaillées à certains points critiques du circuit.

Les résultats sont encouragents et vérifient nos autres résultats et mesures. À chaque débit, même au plus grand, nous trouvons des agrégats dans la région proche de la paroi. Pourtant, c'est la région où le taux de cisaillement est le plus élevé. Ainsi nous pouvons conclure que de plus grandes structures sont également présentes dans la région centrale du tuyau. Nous avons observé une réduction de taille des flocs seulement au débit le plus élevé. Ces constatations sont importantes parce que cela signifie que le cisaillement n'est généralement pas suffisant pour détruite tous le flocs dans la suspension. En outre, cela indique que dès que la vitesse d'écoulement diminue, des flocs se reforment et se développent dans la masse.

L'allure générale des courbes de pertes de charge est expliquée par la présence d'un piston fibreux aux faibles vitesses d'écoulement. Pour vérifier l'existence de ce piston, nous avons employé une technique de mesure de vitesse non intrusive : nous avons déterminé des profils de vitesse des particules grâce à la vélocimétrie Doppler à ultrasons pulsés. Cette méthode développée à l'origine pour le domaine médical est, de nos jours, utilisée dans d'autres secteurs, particulièrement en mécanique des fluides appliquée à des suspensions. Nous avons constaté qu'un régime complètement turbulent n'est obtenu qu'à vitesse d'écoulement élevée, c'est-à-dire plus de 4 m/s, la valeur dépendant de la concentration en fibres. Rappelons que cette valeur est supérieure à la valeur pour laquelle la perte de charge pour la suspension devient inférieure à celle de l'eau. Ainsi, nous concluons qu'un effort de cisaillement élevé devrait être sans cesse appliqué pour garantir une bonne mobilité des fibres dans la suspension afin d'obtenir une bonne formation de la feuille.

Il peut se produire un effet Coanda à l'admission de la chambre de stabilisation pour un élargissement trop important. Comme toute perturbation à l'intérieur de la caisse de tête peut interférer sur fonctionnement entier de celle-ci, cet effet est à éviter et nous pensons que la forme de l'entrée devrait être optimisée (sauf moindre ou élargissement progressif).

D'un point de vue hydrodynamique, l'écoulement est établi à la sortie de la chambre de stabilisation. Si cette chambre est employée comme chambre de mélange c.-à-d. si un système local de dilution est employé, son utilité est justifiée. Cependant, s'il n'y a aucun mélange, nous estimons qu'une chambre de stabilisation plus courte pourrait être employée.

Générateur de turbulence

Le générateur de turbulence dans les caisses de têtes modernes est la plupart du temps composé par un ensemble de tubes parallèles, qui distribuent la suspension dans le convergent. Une turbulence de forte intensité y est produite. L'objectif principal de ce dispositif est appliquer une certaine quantité d'énergie turbulente à une certaine échelle turbulente à la suspension fibreuse pour rompre la plupart des flocs et d'obtenir la pâte la plus homogène possible. Nous avons observé visuellement que le niveau de floculation de la suspension avant et après le générateur n'est pas sensiblement différent. Ainsi, il se pose une question primordiale : l'énergie appliquée dans ce dispositif est-elle correctement employée ? Pour l'étudier , nous avons suivi deux approches différentes :

- Premièrement, caractériser en termes de chute de pression et d'intensité de turbulence la quantité d'énergie appliquée dans cette installation et déterminer s'il y n'a pas de différence (d'un point de vue hydraulique et énergétique) entre l'eau et une suspension fibreuse.
- Deuxièmement, étudier qualitativement la floculation des suspensions et tenter de déterminer l'efficacité de l'énergie appliquée. Dans cette optique, nous avons décrit les deux différents mécanismes théoriques de défloculation et fait une analyse critique des méthodes de mesure disponibles pour déterminent la taille des flocs.

Afin de mieux comprendre chaque paramètre à l'intérieur d'un tube de générateur de turbulence, nous avons réalisé une installation de laboratoire, comportant un diaphragme hydraulique épais échangeable et avons étudié deux paramètres géométriques, la longueur du diaphragme et le diamètre de l'orifice. Ce dernier paramètre est celui qui agit le plus sur la quantité d'énergie dissipée dans l'installation. Dans une première partie de l'étude, nous avons choisi un diaphragme de 3 millimètres de longueur et nous avons changé son diamètre. Par simulation numérique des écoulements, nous avons trouvé que la dissipation turbulente change remarquablement entre l'orifice de 15 millimètres de diamètre et celui de 5 millimètres, passant de 25 W/kg de fluide à 850 W/kg de fluide. En d'autres termes la dissipation turbulente est multipliée par un facteur de 34 quand le diamètre est divisé par. Par contre, entre 15 millimètres et 10 millimètres de diamètre, il n'y a une aucune grande différence en termes de dissipation turbulente, les valeurs passant de 25 W/kg de fluide à 50 W/kg de fluide pour le deuxième cas. Les mêmes constatations s'appliquent à la longueur turbulente. Cependant l'écart relatif entre tous les cas est beaucoup plus faible que pour la dissipation turbulente.

Compte tenu de ces résultats, il est intéressant d'analyser l'effet de cette énergie sur l'état de floculation des suspensions fibreuses. À cet effet, nous avons réalisé une étude qualitative de l'aspect des suspensions fibreuses avant et après le passage par les dia-

phragmes. Pour la plupart des cas observés, il n'y a aucune différence apparente de la taille de flocs avant et après le diaphragme, sauf pour le cas du diaphragme de diamètre 5 millimètres et longueur 3 millimètres de longueur, qui délivre une suspension plus homogène. Cependant, la quantité d'énergie dissipée dans cette configuration est beaucoup trop forte pour être employée industriellement (autour de 1 kilowatt par kilogramme de suspension). Dans le cas général, on observe une pâte homogène juste après le diaphragme mais cette homogénéité disparaît rapidement. En d'autres termes, il pourrait être possible que le passage par les diaphragmes produise un certain degré de défloculation, mais les gros tourbillons en aval régénèrent les flocs qui viennent d'être rompus. Nos résultats expérimentaux montrent que le diamètre de l'orifice devrait être lié au type de pâte à papier : pour des fibres de résineux, il devrait être plus petit (plus haut niveau d'énergie appliqué) que pour des fibres de feuillus.

Il faut aussi se poser la question de l'utilité d'un générateur de turbulence et de son véritable effet sur une suspension fibreuse. A partir d'images prises avec la caméra rapide, sur le dispositif prototype, nous n'avons observé aucun changement apparent de taille des flocs. Ceci signifierait que l'énergie consommée dans ce dispositif est complètement dissipée dans le milieu liquide et non pas utilisée pour défloculer. Il y aurait un glissement entre les fibres et le fluide vecteur. Ceci nous amène à penser qu'une autre technologie pourrait être utilisée, l'utilisation d'ultrasons qui donneraient un certain degré d'activation aux fibres et non à l'eau. Ce type de technologie a déjà été utilisé avec succès sur l'unité de formation de la feuille. Il se pose toutefois la question de la consommation d'énergie d'un tel dispositif et des risques encourus.

Malgré nos constatations, nous savons que l'expérience industrielle montre une vraie amélioration de la formation de feuille quand la caisse de tête contient un générateur de turbulence. Les différentes approches que nous avons prises ne nous ont pas permis de mesurer raisonnablement la taille des flocs et les forces inter-fibres. D'autres techniques de mesure restent à développer pour mieux comprendre le véritable effet de la turbulence à l'intérieur d'une structure floculée.

Convergent

La fonction principale du convergent est d'accélérer la suspension à une vitesse industrielle acceptable. La majeure partie des papetiers pense que c'est sa seule fonction. Il se pose cependant aussi le problème de la cohérence du jet. Nous n'avons pas trouvé de critères de conception allant dans ce sens dans le cadre des applications papetières. par contre, des informations ont été publiées pour des applications minières, et celles-ci

devraient être valables, au moins en partie, en papeterie puisqu'elles concernent la même problématique. Nous énumérons donc ces critères et les commentons :

- Éviter les tourbillons à grande échelle et tout mouvement rotationnel à l'entrée du convergent. En fabrication du papier, l'entrée du convergent est situé à l'extrémité du générateur de turbulence. On peut donc trouver de gros tourbillons, selon la géométrie des tubes et le débit traversant. En l'absence de défaut de fabrication, il ne devrait pas y avoir de mouvement rotationel mais, selon la disposition de la sortie du générateur quelques tourbillons périodiques pourraient exister.
- Assurer une intensité turbulente suffisante à l'entrée du convergent. Dans notre cas, pour maintenir une pâte homogène, une petite échelle de turbulence et une intensité turbulente élevée sont nécessaires tout au long du convergent.
- Éviter les parties saillantes entre la tuyauterie d'admission et le convergent lui-même. Si des sauts sont inévitables, ils devraient être des élargissements, non des rétrécissements, et idéalement être de taille limitée à l'ordre de grandeur de l'épaisseur de la sous-couche laminaire locale. Vu notre caisse de tête pilote, le convergent étudié n'est pas symétrique. Il y a donc un changement de géométrie avec un joint entre les deux parties (générateur de turbulence et convergent). Aucune perturbation n'a été observée à cet endroit, mais ce pourrait être une source de non-homogénéité au jet. Nous pourrions débattre de certains paramètres chaque fois que nous avons travaillé avec un liquide newtonien : l'ordre de grandeur de la sous-couche laminaire, qui est déjà très petit. Mais de plus, chaque fois que nous utilisons une suspension fibreuse, nous ne pouvons pas parler de sous-couche laminaire ni de fluide homogène à cette échelle. La présence des fibres change le comportement de l'écoulement et, s'il y a une sous-couche laminaire, son épaisseur est si réduite qu'il est difficile de penser qu'elle a une influence sur le comportement de l'écoulement.
- Réduire l'intensité turbulente en sortie du convergent grâce à un rapport de contraction compris entre 10 et 45. Le rapport de contraction est défini comme rapport de taille en entrée et en sortie. Dans notre cas, il était de 11,45, valeur qui est dans la limite basse du rapport de contraction voulu.
- Minimiser la hauteur en sortie du convergent et la longueur du convergent ; s'assurer que les parois du convergent soient hydrauliquement lisses. L'utilisation d'une règle à l'extrémité du convergent provoque une accélération soudaine et évite que les faces en sortie soient parallèles ; ceci va agir comme le convergent décrit ci-dessus. Le facteur d'aspect, rapport de la longueur du convergent à sa hauteur en entrée, devrait être de l'ordre de 1. Dans notre cas, il était égal à 4,39. Aidun a constaté qu'il se forme moins de stries quand le rapport tend vers 1.
- Éviter le décollement de la couche limite à l'entrée du convergent et la génération de turbulence à grande échelle dans les zones de recirculation induites. Ceci est lié

au point précédent, le facteur d'aspect du convergent devrait tendre vers 1 mais ceci devrait être pris avec précaution. Une paroi en forme d'arc cubique est conseillé à l'entrée du convergent pour empêcher le décollement de couche limite.

- Éviter toute cavitation près de la sortie de convergent due aux changements de courbure de la paroi et parties rugueuses. En fabrication du papier, l'utilisation d'un bec à l'extrémité de convergent est tout à fait commune. Ce bec est généralement un changement soudain de l'inclination de la paroi du convergent. Avec un angle assez raide, la cavitation pourrait se produire. Toutefois ce n'est pas le seul problème, quelques zones mortes avec des recirculations pourraient apparaître dans cette région.
- Donner la possibilité de re-laminarisation de la couche limite dans le convergent. Ce phénomène, comme expliqué auparavant, est possible avec un fluide homogène. Avec une suspension fibreuse, la re-laminarisation de la couche limite (s'il y en a une) est improbable du fait de la présence des fibres dans la région proche de la paroi.

Il pourrait être intéressant de vérifier si ces paramètres de conception s'appliquent afin d'optimiser le jet. Selon les résultats obtenus par simulations en CFD ne permet de conclure que ces paramètres préconisées pour l'industrie minière sont les meilleurs pour l'industrie papetière. Néanmoins, un modèle de CFD ne peut pas remplacer une vraie installation expérimentale où l'évolution du jet peut être vue et comparée à d'autres géométries. Il pourrait être très intéressant de déterminer si les paramètres géométriques de convergent peuvent être optimisés pour obtenir un jet de meilleure qualité, sans écoulements secondaires.

En termes de défloculation, nous avons observé de grosses structures fibreuses dans le convergent et aucune défloculation n'a été vue dans cette partie de la caisse de tête. Ceci semble logique parce qu'à l'intérieur du convergent la turbulence diminue. Les flocs s'étiraient seulement au niveau de la barre de profil, ce qui peut permettre de les rompre temporairement. Nous pouvons maintenant dire que l'échelle et l'intensité de la turbulence devraient être conservées dans le convergent, ce qui justifie l'utilisation des lames à l'intérieur du convergent. La littérature est riche à ce sujet et l'on peut trouver des paramètres d'optimisation de ces lames.

Contrôle du jet en sortie de caisse de tête

Contrôler le jet en sortie d'une caisse de tête est extrêmement important pour la fabrication du papier. En effet la qualité du papier dépend de la vitesse et de l'angle du

jet de suspension au point d'impact sur l'unité de formation. Ces paramètres influencent l'orientation moyenne des fibres dans la feuille de papier. Ces paramètres sont très sensibles et il faut, la majeure partie du temps, une opération d'essai/erreurs consommatrices de temps et d'argent pour les régler. De nos jours, le principe de base de calcul de la vitesse du jet est basé sur l'équation de Bernoulli (ou une approximation au moyen de l'équation de Torricelli). L'angle du jet à l'impact peut être approché en utilisant une équation ballistique simple, si l'on connaît l'angle du jet à la veine contractée. Cependant, ces méthodes ne fournissent pas toute l'information requise parce qu'on ne connaît pas la forme du jet et l'angle à la veine contractée. Pour résoudre ce problème, outre l'expérimentation qui demanderait une quantité de travail phénoménale, la modélisation et la simulation numérique des écoulements peuvent être une aide. Comme nous avons constaté expérimentalement qu'il n'y avait pas de différence significative lorsque nous utilisions des suspensions de pâte à papier et de l'eau seule, nous nous limiterons au cas de l'eau. En effet, seule la rugosité de la surface du jet est modifiée. Ceci indiquerait que l'échelle de turbulence est modifiée par la présence des fibres, mais aucune technique de mesure ne permet de déterminer précisément l'énergie absorbée par les fibres et la part consommée par la défloculation.

Nous avons trouvé dans la littérature différentes études, basées sur les écoulements de fluides idéaux et les transformations conformes, pour prédire l'angle et la contraction du jet issu d'un convergent. Ce sont notamment les travaux de Birkhoff et Zarantonello, Attwood, Appel et Yu, Dias, Elcrat et Trefethen.

- Dans les deux premières références, on trouve des information nécessaires au calcul du jet issu d'un convergent simple. Ce convergent a donc une longueur infini. Il peut représenter valablement une caisse de tête dont le convergent est long, si la buse terminale n'a pas de barre de profil.
- La troisième référence concerne le cas d'un convergent simple de hauteur limitée. Il peut représenter valablement par exemple une caisse de tête dans laquelle la hauteur de suspension est limitée et dont la buse terminale comporte un simple convergent. Les calculs sont basés sur l'utilisation d'une transformation de Schwarz-Christoffel. Les travaux de Appel et Yu ont permis la construction d'abaques donnant l'angle et la contraction du jet en fonction de paramètres géométriques.
- La quatrième, également basée sur une transformation de Schwarz-Christoffel, couvre le cas d'un convergent de forme quelconque, dont les deux faces d'entrée sont parallèles. Elle représente le cas le plus général.

Ces modèles ne présentent pas de difficultés majeures de mise en oeuvre informatique avec les outils de calcul modernes. Ils présentent l'avantage de permettre le calcul non

seulement de l'angle du jet et de son coefficient de contraction, mais aussi de déterminer la forme des contours du jet et des lignes de courant. Ceci est utile pour estimer la position de la veine contractée. Expérimentalement, nous avons constaté que les modèles les plus simples peuvent convenir dans un certain domaine avec une caisse de tête moderne. On observe une déviation lorsque l'ouverture des lèvres de la caisse de tête est trop importante, à la limite en dehors des conditions normales d'utilisation. Les modèles plus complexes, basés sur une transformation de Schwarz-Christoffel, qui permettent de mieux décrire des convergents réels, font apparaître quelques différences selon les rapports géométriques. Enfin, pour tous les cas étudiés, nous trouvons par simulation que la veine contractée se situe avant l'extrémité de la lèvre inférieure de la caisse de tête, ce qui est un résultat nouveau.

Comme l'angle et vitesse du jet sont difficiles à mesurer en conditions industrielles, nous pensons que ce type de modèle simple peut s'avérer utile au réglage de la machine à papier. Avec la détermination de la position de la veine contractée, nous pouvons aussi aider à prévoir la position du point d'impact du jet sur la table de fabrication, ce qui est également important.

Enfin, nous avons utilisé un logiciel de CFD avec un modèle diphasique air/eau pour tracer les contours du jet. Il n'existe pas (ou peu) de résultats publiés dans la littérature à ce sujet. Nos résultats vont dans le même sens que les simulations avec les modèles plus simples. Ils nous apportent des informations supplémentaires notamment sur l'intensité turbulente.

Nous résumons dans le tableau suivant les avantages, inconvénients et limitations des différentes méthodes utilisées.

Méthode	Avantages	Inconvénients / restrictions
Abaques	Faciles à utiliser pour les applications industrielles Utiles pour déterminer de l'angle du jet et son coefficient de contraction	Fluides idéaux seulement Non représentatives de la géométrie des caisses de tête modernes
Modèle d'Attwood et Fonction Beta incomplète	Calcul : - de l'angle du jet - du coefficient de contraction - des lignes de courant et équipotentielles - de la position de la veine contractée Moyens informatiques simples	Fluides idéaux seulement Un seul facteur géométrique en plus de l'angle du convergent Convergent infini Valable uniquement pour des faibles ouvertures
Schwarz-Christoffel	Calcul : - de l'angle du jet - du coefficient de contraction - des lignes de courant et équipotentielles - de la position de la veine contractée Moyens informatiques simples N'importe quel convergent	Mathématiquement plus complexe Fluides idéaux seulement
CFD	Fluide pseudo réel Mêmes informations que ci-dessus Autres informations (turbulence, mélange)	Moyens informatiques dédiés Spécialiste en CFD Coûteux et longueur du temps calcul

TABLE B.1 – Comparaison des méthodes

Quelques remarques de conclusion

Nous avons effectué une étude hydraulique et énergétique au niveau de chaque partie d'une caisse de tête. En couplant travaux expérimentaux et CFD nous avons pu proposer quelques éléments d'optimisation (ou de voies d'amélioration) mais nous ne pouvons pas conclure que toutes ces règles conviendront à chaque caisse de tête disponible sur le marché. Cependant, il semble bien que l'énergie appliquée dans le système devrait être mieux utilisée. Il existe des outils disponibles pour analyser une partie du problème. Dans un monde où l'énergie et l'eau deviennent les valeurs stratégiques, des efforts devraient être faits pour obtenir une meilleure compréhension de la formation de papier et donc une réduction de la consommation d'eau et d'énergie. Le premier problème à résoudre, qui est un vrai défi, est le développement d'une technique de mesure non intrusive et fiable pour déterminer s'il existe un glissement entre les fibres et l'eau. Si ce glissement existe, les niveaux de turbulence exercés, destinés normalement à défloculer la suspension, ne sont pas correctement employés.

General bibliography

[1] P.B. Meggs. *A history of graphic design*. John Wiley & Sons, Inc., 1998. ISBN : 0-471-291-98-6.

[2] J. Gullichsen and H. Paulapuro. *Chemical Pulping*, volume 6a. Tappi Press, 1990.

[3] J.R. Istas and E.L. Raekelboom. Etude biométrique, chimique et papetière de quelques conifères exotiques. *Régisseur de la Donation Royale à Bruxelles*, 1967.

[4] J.R. Istas and E.L. Raekelboom. Etude biométrique, chimique et papetière de quelques essences feuillues. *Régisseur de la Donation Royale à Bruxelles*, 1970.

[5] A. Einstein. Eine neue bestimmung der molekuldimensionen. *Ann. Phys.*, 19 :289–306, 1906.

[6] A. Einstein. Corrections of "eine neue bestimmung der molekuldimensionen". *Ann. Phys.*, 34 :591–592, 1911.

[7] S.G. Mason. The motion of fibers in flowing liquids. *Pulp and Paper Magazine of Canada*, pages 93–100, 1950.

[8] Douglas Wahren and R. Meyer. On the elastic properties of three-dimensional fiber networks. *Svensk Papperstidning*, 67(10) :432–436, 1964.

[9] C.T.J. Dodson. Fiber crowding, fiber contacts, and fiber flocculation. *Tappi Journal*, 79(9) :211–216, 1996.

[10] N. Pan. A modified analysis of the microstructural characteristics of general fiber assemblies. *Textile Res. Journal*, 63(6) :336–345, 1993.

[11] R. Soszynsky. *The formation and properties of coherent flocs in fiber suspensions*. PhD thesis, University of British Columbia, 1987.

[12] R. Kerekes, R.M. Soszynski, and P.A. Tam Doo. The flocculation of pulp fibers. In FRC, editor, *Trans. 8th Fundamental Research Symposium Oxford*, pages 265–310, 1985.

[13] R.J. Kerekes and C.J. Schell. Characterization of fibre flocculation regimes by a crowding factor. *Journal of Pulp and Paper Science*, 18(1) :32–38, January 1992.

[14] D.M. Martinez, K. Buckley, S Jivan, A. Lindstrom, R. Thiruvengadaswamy, J.A. Olson, T.J. Ruth, and R. Kerekes. Characterizing the mobility of papermaking

fibers during sedimentation. In FRC, editor, *Trans. 12th Fundamental Research Symposium-Oxford*, pages 225–254, 2001.

[15] G. Jacquelin. Cohèsion des réseaux fibreux papetiers en milieu humide. *A.T.I.P.*, 20(4) :153–163, 1966.

[16] D. Wahren. On the visco-elastic of fiber networks. *Svensk Papperstidning*, 67(9) :378–381, 1964.

[17] N. Thalén and D. Wahren. A new elasto-viscometer. *Svensk Papperstidning*, 67(11), 1964.

[18] N. Thalén and D. Wahren. Shear modulus and ultimate shear strength of some paper pulp fiber networks. *Svensk Papperstidning*, 67(4) :259–264, 1964.

[19] J.C. Wollwage. *Paper trade Journal*, 108(12,13) :41, 1939.

[20] O.L. Forgacs, A.A. Robertson, and S.G. Mason. The hydrodynamic behaviour of paper-making fibers. *Pulp and Paper Magazine of Canada*, pages 117–128, May 1958.

[21] G.G. Duffy, A.L. Titchener, P.F.W. Lee, and K. Møller. *Appita*, 29(5) :363, 1976.

[22] F. Lundell, D Söderberg, S. Storey, and R. Holm. The effects of fibers on laminar-turbulent transition and scales in turbulent decay. In FRC, editor, *Trans. 13th Fundamental Research Symposium-Cambridge*, pages 19–34, 2005.

[23] A.A. Robertson and S.G. Mason. The flow characteristics of dilute fiber suspensions. *Tappi*, 40(50) :326–335, 1957.

[24] T. Paul, G. Duffy, and D. Chen. New insights into the flow of pulp suspensions. *Tappi solutions !*, 1(1), 2001.

[25] C.P.J. Bennington, R. Kerekes, and J.R. Grace. Motion of pulp fiber suspensions in rotary devices. *Canadian Journal of chemical engineering*, 69 :251–258, 1991.

[26] R.J. Kerekes. Pulp flocculation in decaying turbulence : a literature review. *Journal of pulp and paper science*, 9(3) :86–91, 1983.

[27] L Salgueiro, M. Rueff, and J-C. Roux. Towards a better understanding of pulp suspension flows. In Tappi Press, editor, *Tappi Papermakers Conference-Atlanta*, 2006.

[28] G.G. Duffy. Flow of medium consistency wood pulp fiber suspensions. *Appita Journal*, 48(1) :51–55, 1995.

[29] S.G. Mason. The flocculation of cellulose fiber suspensions. *Pulp and Paper Magazine of Canada*, pages 99–104, 1948.

[30] L. Salgueiro. Etude de l'écoulement de suspensions fibreuses par vélocimétrie doppler à ultrasons et analyse d'image. Master's thesis, LGP2, Ecole Française de Papeterie et des Industries Graphiques, 2004.

[31] P. Dietemann and M. Rueff. A study of fibre suspension flow by means of doppler ultrasound velocimetry and image analysis. *Canadian Pulp and Paper Association*, Preprint - Vol A :225–230, 2004. Ninetieth Ann. Mtg. Technical Section.

[32] S. Skali Lami. *Contribution à l'étude de l'écoulement de pâte à papier-interaction floculation, turbulence.* PhD thesis, Institut National Polytechnique de Lorraine, 1991.

[33] L.H. Switzer and D.J. Klingenberg. Simulation of fiber floc dispersion in linear flow fields. *Nordic Pulp and Paper Research Journal*, 18(2) :141–144, 2003.

[34] G.G. Duffy and B.G. Norman. Fiber flocculation in conical contractions simulating the papermachine flowbox slice. In McGill University Dept. of Chemical engineering, editor, *Trans. International Symposium Papermachine Headboxes*, 1979.

[35] R.J. Kerekes. Pulp floc behavior in entry flow to constrictions. *Tappi Journal*, 1 :88–91, 1983.

[36] T.Q. Li and L. Ödberg. Studies of flocculation in cellulose fibre suspensions by nmr imaging. *Journal of Pulp and Paper Science*, 23(8) :401–405, 1997.

[37] J. Ringnér and A. Rasmuson. Characterisation of fiber suspensions using X-Ray computed tomography and image analysis. *Nordic Pulp and Paper Res. Journal*, 15 :319–325, 2000.

[38] H. Yan and D. Söderberg. Two dimentional wavelet flocculation analysis of fiber suspensions and paper sheets. *Nordic Pulp and Paper Res. Journal*, 21(1) :13–23, 2006.

[39] B. Steemberg and B. Johanson. Viscous properties of pulp suspension at high shear-rates. *Svensk Papperstidning*, 61(18) :696–700, 1958.

[40] M. Horie and K.L. Pinder. Time-dependent shear flow of artificial slurries in coaxial cylinder viscometer with a wide gap. *Canadian Journal of Chemical Engineering*, 57 :125–134, 1979.

[41] E. Ganani and R.L. Powell. Suspension of rod-like particles : Literature review and data correlations. *Journal of Composite materials*, 19 :194–215, 1985.

[42] C.P.J. Bennington and R. Kerekes. Power requirements for pulp suspension fluidisation. *Tappi Journal*, 79(2) :253–258, 1996.

[43] C.J.S. Petrie. The rheology of fiber suspensions. *Journal of non-Newtonian fluid mechanics*, 87 :369–402, 1999.

[44] W.C. Chase, A.A. Donatelli, and J.W. Walkinshaw. Effects of freenes and consistency on the viscosity of hardwood and softwood pulp suspensions. *Tappi Journal*, pages 199–204, May 1989.

[45] O. Anderson. Some observations on fibre suspensions in turbulent motion. *Svensk'c Papperstid.*, 69(2) :23–31, 1966.

[46] D.G. Wagle, C.W. Lee, and R.S. Brodkey. Further comments on a visual study of pulp floc dispersion mechanisms. In *Engineering conference proceedings*, volume 71, pages 137–141. TAPPI Press, Atlanta, 1987.

[47] M.J. Hourani. Fibre flocculation in pulp suspension fiow. part 1 : theoretical model. *Tappi*, 71(5) :115–118, 1989.

[48] M.J. Hourani. Fibre flocculation in pulp suspension flow. part 2 : experimental results. *Tappi*, 71(6) :186–189, 1989.

[49] M. Steen. The 9th fundamental research symposium. In *Mechanical engineering publications Ltd.*, 1989.

[50] TAPPI, editor. *Generalized method for determining the pipe friction loss of flowing pulp suspensions*, TIS 0410-14, 1992. Tappi information Sheets.

[51] Signal Processing S.A., Switzerland. *DOP 2000 User Manual.* www.signal-processing.com.

[52] I.E. Idel'cik. *Memento des pertes de charge.* Eyrolles, Paris., 1988.

[53] H.J. Youn and H.L. Lee. A numerical study of flow behaviour in the turbulence generator of headboxes. *Appita*, 58 :196–201, 2005.

[54] W. Cherdron, F. Durst, and J.H. Whitelaw. Asymmetric flows and instabilities in symmetric ducts with sudden expansions. *Journal of fluid mechanics*, 84 :13–31, 1978.

[55] J. Salmela and M. Kataja. Floc rupture and re-flocculation in turbulent shear flow. In FRC, editor, *Trans. 13th Fundamental Research Symposium Cambridge*, pages 35–50, 2005.

[56] C.K. Aidun and A.E. Kovacs. Hydrodynamics of the forming section : the origin of nonuniform fiber orientation. *Tappi Journal*, 78 :97–106, 1995.

[57] H. Yan. *Fibre suspension flocculation under simulated forming conditions.* PhD thesis, Division of paper technology, Department of fibre and polymer technology, Royal Institute of technology, 2004.

[58] M.K. Jackson and T.W. Davies. Nozzle design for coherent water jet production. In *2nd US Water Jet conference, Rolla, Missouri*, 1983.

[59] TAPPI, editor. *Flow from a 45° slice*, TIS 0410-03, 2004. Tappi information paper (TIP).

[60] TAPPI, editor. *Flow from a nozzle (slice) with inclined upper lip*, TIS 0410-04, 2004. Tappi information paper (TIP).

[61] G. Birkhoff and E.H. Zarantonello. *Jets, Wakes, and Cavities.* Academic Press Inc., 1957.

[62] D. Attwood. Flow of liquids from papermaking slices. Technical report, Bowaters United Kingdom Pulp and Paper Mills Ltd., October 1967.

[63] D. Appel and Y-S Yu. Free-streamline analises of flow from nozzles, flow through side inlets, and flow past corners. Technical report, Departement of mechanics and aerospace engineering, University of Kansas, 1963.

[64] J. McNown and C-S Yih. Free-streamline analyses of transition flow and jet deflection. Technical report, Institut of hydraulic research, Iowa University, 1953.

[65] F. Dias, A.R. Elcrat, and L.N. Trefethen. Ideal jet flow in two dimensions. *Journal of Fluid Mechanics*, 185 :275–288, 1987.

[66] D. L. Youngs. Time-dependent multi-material flow with large fluid distortion. *Numerical Methods for Fluid Dynamics*, 1982.

[67] J. U. Brackbill, D. B. Kothe, and C. Zemach. A continuum method for modeling surface tension. *J. Comput. Phys.*, 100(2) :335–354, 1992.

[68] T.-H. Shih, W. W. Liou, A. Shabbir, Z. Yang, and J. Zhu. A new k-epsilon eddy viscosity model for high Reynolds number turbulent flows : Model development and validation. *NASA STI/Recon Technical Report N*, 95 :11442–, August 1994.

Etude expérimentale et simulation d'écoulements de suspensions fibreuses - Application à une caisse de tête

Résumé
L'évolution des machines à papier pour obtenir des qualités de papier supérieures a fait évoluer les équipements papetiers en complexité et en précision. L'injecteur hydraulique de pâte à papier, appelé caisse de tête dans l'industrie, n'a pas échappé à cette règle. Nous avons analysé chaque partie constituant une caisse de tête, en nous basant sur des observations et mesures directes quand les conditions le permettaient, ou sinon grâce à des simulations numériques, pour répondre à des questions essentielles relatives à l'utilité et au dimensionnement de chaque partie d'une caisse de tête moderne. Pour cela, deux approches ont été retenues : la première est l'étude hydrodynamique de la suspension circulant dans chaque élément, surtout en termes d'échelle et intensité de turbulence ; la deuxième est l'analyse de la réaction de la pâte à cette énergie. Nous avons remarqué que l'eau peut être utilisée au lieu d'une suspension fibreuse pour établir les paramètres de dimensionnement. Finalement, nous avons étudié les paramètres géométriques de la buse terminale d'une caisse de tête pour donner des solutions alternatives aux méthodes actuelles servant au contrôle du jet. Nous avons démontré que les modèles existants pour caractériser le jet ne sont pas toujours applicables aux caisses de tête modernes et avons observé qu'aucune solution alternative n'est proposée actuellement pour calculer correctement l'angle et le coefficient de contraction du jet. Nous avons montré que le calcul de l'angle du jet est possible pour tout type de géométrie et avons mis en évidence la position de la veine contractée. Nous avons aussi montré que l'utilisation d'un double convergent peut modifier significativement l'angle de jet et cela devrait être pris en compte.

Mots clés : Caisse de tête, suspension fibreuse, CFD, turbulence, jet, veine contractée.

Experimental study and computational simulation of fibre suspension flows - Application to headboxes

Abstract
The evolution of paper machines in order to get better paper grades at faster production rates imposed paper mills to operate more complex systems and gain in precision. The hydraulic injector which delivers the pulp onto a paper fabric, commonly called headbox, has not escaped from this evolution. In this work a detailed analysis and simulation of each part of a headbox was made. From these simulations and whenever possible from experimental observations and measurements, some basic questions were tried to be answered, like the need of each part in a modern papermaking operation. Two different approaches were chosen, firstly a hydrodynamical study of the pulp flowing inside the different parts, focusing especially on turbulence scales and intensities and, secondly, the reaction of this pulp to the applied energy. It was observed that water can be used to reasonably predict the behaviour of a weak consistency pulp suspension for most of the important design parameters. The geometrical parameters of a headbox were also studied in order to provide alternative methods for jet control. Indeed the jet geometrical characteristics are important variables for paper production. Most of the time miscalculated by old methods, no modern solutions were proposed to get a detailed jet angle and contraction coefficient. We have shown in this work that a detailed solution for any nozzle geometry can be computed. The location of the vena contracta is also possible with the proposed method. It was also shown that the real nozzle geometry used normally in a modern headbox with a double convergent configuration, may considerably modify the jet angle.

Keywords : Headbox, fibre suspension, computational fluid dynamics, turbulent, jet, vena contracta